POLITECNICO DI MILANO

Scuola di Ingegneria Industriale e dell'Informazione

Corso di Laurea Magistrale in
Ingegneria Aeronautica

Numerical Study of The Vortical Flow Over a Reverse Delta Wing

Relatore: Prof. Luca CORTELEZZI

Tesi di Laurea di:
Ahmed Osama Mohamed Elhassan MAHGOUB
Marticola 862379

Anno Accademico 2017-2018

To my father,
who made sure that I only worry about my studies by providing everything I need...
To my mother,
who never stopped in believing in me, and kept telling me that I can do it...
To my brother and sisters,
for helping me overcome the hardest times and bringing me joy...
To my wife,
for giving me a 1000 reason to work harder..
To all the people who were a reason of what I am right now, my friends and teachers...
I dedicate this work to you...

Abstract

Reverse delta wings have been used in Lippisch type wing-in-ground crafts since the 1960's of the previos century, due to their stabilizing pitching moment close to ground. Previous studies showed that reverse delta wing behaves differently from a regular delta wing, either in terms of aerodynamic performance or flowfield structure. Up to this date only one study that includes a numerical simulation for the flow past a reverse delta wing have been published. In this thesis, we simulate numerically the unsteady flow past a reverse delta wing to understand better its aerodynamic performance, the structure of the flowfield and the unsteady phenomena associated. The numerical simulations are performed using ANSYS Fluent commercial software. The turbulence model used is Delayed Detached-Eddy in conjunction with the kω-SST as a RANS model. We selected the grid size and time step by performing a time step and grid sensitivity analysis using the power spectral density of the time history of the lift coefficient C_L for the flow past a delta wing at angle of attack $\alpha = 20°$. Before simulating numerically the flow past a reverse delta wing, we perform unsteady numerical simulations for the flow past a delta wing at angles of attack ranging from 5° to 20°. We found that the lift of a reverse delta wing is unsteady even at angles of attack as low as 5°, differently from a delta wing. The power spectral density analysis shows that the time history of the lift coefficient C_L is related to the time history of vortex shedding. The numerical simulations showed that over the leeward side of the reverse delta wing, the shear layer separating at the leading edge rolls into spanwise vortical structures that are convected downstream. As the vortical structures are convected, they alter the pressure distribution over the leeward side of the reverse delta wing. The results also showed that the tip vortex of a reverse delta wing is formed entirely by flow coming from the lower side of the wing. When comparing the performance of the delta wing against the reverse delta wing, at angles of attack below 10, both wings generated the same lift and drag, while at higher angles of attack, the reverse delta wing generated less lift and had less drag than the delta wing, but the lift-to-drag ratio for both wings is almots the same.

Keywords: Computational Fluid Dynamics; Delta wing; Detached-eddy simulation; Finite Volume Method; Reverse delta wing;

Acknowledgement

I would like to thank my supervisor, professor Luca Cortelezzi, for his help, he dedicated to me most of his time and always provided advises and suggestions for the improvement of this thesis. I would also like to thank the Department of Aerospace Sciences and Technology at Politecnico di Milano for providing me the computational resources necessary to complete this work.

Contents

List of Figures

List of Tables

Nomenclature

Abbreviations

CFD	Computational fluid dynamics
DDES	Delayed Detached-Eddy simulation
DES	Detached-Eddy simulation
DW	Delta wing
FVM	Finite volume method
LES	Large Eddy simulation
PIV	Particle Image Velocimetry
PSD	Power spectral density
RANS	Reynolds averaged Navier-Stokes equations
RDW	Reverse delta wing
SVF	Spanwise vortex filament
URANS	Unsteady Reynolds averaged Navier-Stokes equations
WIG	Wing-in-ground

Greek letters

α	Angle of attack (deg)
Δ	Mesh cell dimension (m)
δ_t	Turbulent boundary layer thickness (m)
Γ	Circulation (m^2/s)
κ	von Karman constant
ε_{ij}	Turbulent dissipation rate tensor
μ	Dynamic viscosity (m^2/s)
μ_t	Dynamic turbulent viscosity (m^2/s)
ν	Kinematic viscosity (Pa.s)
ν_t	Kinematic turbulent viscosity (Pa.s)
ω	Specific dissipation rate (1/s)
Ω_{ij}	Rotation part of the velocity gradient tensor
ϕ	Generic scalar quantity
ϕ_f	Face value of generic scalar quantity
ρ	Density (kg/m^3)
τ_w	Wall shear stress (Pa)
τ_{ij}	Shear stress tensor
ε	Dissipation rate of turbulent kinetic energy ((m^2/s^3))
ζ	x-component of vorticity (1/s)

Symbols

$\bar{\mathbf{u}}$	Filtered velocity field
ΔA_i	ith-cell face area m^2
Δt	Time step (s)
$\Delta t^\star$	Non-dimensional time step
$\hat{\mathbf{u}}$	Non-dimensional flow quantity
$\langle u \rangle$	Mean flow quantity
$\mathbf{D}$	Anisotropic part of Reynolds stresses tensor
$\mathbf{I}$	Identity tensor
$\nabla \mathbf{u}$, $\frac{\partial u_i}{\partial x_j}$	Velocity gradient tensor
$\mathbf{n}$	Unit normal vector
$\mathbf{r}$	Location vector (m)
$\mathbf{u}$	Velocity vector (m/s)
$\mathbf{u}'$	Fluctuating flow quantity
a_P, a_{nb}	Coefficients for the finite volume method
b	Wing span (m)
c	Wing mid chord (m)
C_D	Drag coefficient
C_f	Skin friction coefficient
C_L	Lift coefficient
C_m	Pitching moment coefficient
C_p	Pressure coefficient
C_S	Smagorinsky constant
c_∞	Free stream sound speed (m/s)
d	Distance to the wall (m)
f	Frequency (1/s)
F_1, F_2	Blending functions for the kω-SST turbulence model
f_d	Delaying function for DDES
F_i	Convective flux at the ith-face (kg/s)
J_i	Mass flux at the ith-face (kg/m^{2}s)
k	Turbulent kinetic energy (m^2/s^2)
l^*	Turbulent length scale (m)
l_S	Smagorinsky length scale (m)
M_∞	Free stream Mach number
P	Pressure (Pa)
P_k	Production of turbulent kinetic energy
r_f	Delaying parameter for DDES
Re_∞	Free stream Reynolds number
S_ϕ, S_{u_k}	Source terms
S_{ij}	Strain rate tensor
S_{ref}	Wing planform area (m^2)
St	Strouhal number
t/c	Thickness-to-chord ratio
u, v, w	x, y and z velocity components (m/s)
u^*	Turbulent velocity scale (m/s)
U_∞	Reference velocity (m/s)

u_τ	Friction velocity (m/s)
V	Cell volume (m^3)
y^+	Normalized wall distance
y_v	Vortex core spanwise location (m)
z_v	Vortex core vertical location (m)

Chapter 1

Introduction

Ever since the first flight by the Wright brothers, at the beginnings of the previous century, various wing configurations have been developed and tested in search for an optimum wing. An optimum wing configuration valid for all applications cannot be found because the aerodynamic characteristics of a wing depend on flight conditions, such as airspeed and altitude. Therefore, wings that perform well in certain regimes could perform poorly in others. To select the most suitable wing configuration, we need to determine its performance in the desired flight regime. Various methods are used to determine the aerodynamic characteristics of wings, including experimental techniques, methods based on analytic solutions and most recently computational fluid dynamics (CFD). We begin the first chapter of this thesis by discussing the current applications of reverse delta wings compared to those of regular delta wings. Following that, we provide a brief theoretical background about unsteady flows past delta wings, and an overview of the relevant experimental and numerical studies of flows over both the delta wings and reverse delta wings. We then move on to state the motivations of this thesis and its objectives. And lastly, we discuss the methodology used in this thesis.

1.1 Current applications of reverse delta wings

As a wing approaches the ground, a ram pressure below the wing is generated and leads to a rise in static pressure below the wing, and consequently the lift increases. The presence of the ground also interacts with the wing tip vortices and attenuates their strength, which reduces the induced drag, and eventually the total drag, and the total effect is an increase in the lift-to-drag ratio of the wing. However, this lift increase along with the variation in pressure distribution are accompanied by a backward shift in the location of the aerodynamic center of the wing, meaning a more negative pitching moment. This makes the wing less stable than in the case of free flight. Thus, for stable ground flight, we need to use a horizontal stabilizer with a larger area.

Lippisch in his patents, published in the 1960s [3, 4], proposed the use of the reverse delta wing (RDW) configuration for seaplanes that fly close to sea level to benefit from the RDW performance in ground effect. The Lippisch style RDW in ground (WIG) configuration has since been extensively used compared to other WIG craft configurations [5]. What makes a RDW configuration suitable for ground flight, is that it has a stabilizing pitching moment

C_m close to the ground, because the shift of the aerodynamic center is much less than a conventional wing. Therefore, the tail size required for longitudinal stability will be smaller. In figure 1.1 we can see examples of Lippisch type WIG craft.

Gerhardt (1996) [6] in his patent considered the design of a supersonic natural laminar flow wing by using a RDW configuration. His work mainly concentrated on supersonic flow applications where the supersonic wave drag and the skin friction drag values are the same for both the conventional and the RDWs. He mentions that due to a more favorable pressure gradient in the RDW, a laminar flow across a wider region of the wing can be achieved and thus leading to almost 50 percent of the wing area to have a laminar flow, which reduces the drag. He also pointed out that the lift of a RDW is lower compared to that of a conventional delta wing.

Other than the patent of Gerhardt (1996) [6], the RDW has rarely been considered for high speed flight and most of its applications are at low flight speeds. Even at low speed flight, RDWs are not considered for flight in the free stream. This led to lack of literature regarding the RDW. In the future, applications like Micro Air Vehicles could utilize the advantages of using a RDW like configurations in ground effect, and this could lead to more research activity.

1.2 Previous studies

1.2.1 Delta wings

In a conventional wing, the airflow over the upper surface accelerates as a result of the circulation generated around the wing section, while it decelerates over the lower surface. The pressure difference between upper and lower surfaces us responsible for the lift force is produced. The lift generated by a conventional wing can be accurately predicted by wings theory. Differently from conventional wings, delta wings (DW), which find applications in fighter aircraft and supersonic commercial planes (namely the Concorde) due to their good performance in supersonic flight. Stall of conventional wings can happen at angles of attack values ranging from 12° to 15°, while a DW can reach angles of attack beyond 25° without stalling, and this led to using it for highly maneuverable aircraft.

Literature regarding DWs starts in the middle of the last century and continue to be produced. The mechanism of lift generation of a DW differs from that of conventional wings, in DWs the boundary layers at the leading edge separate and create a shear layer that rolls up into a pair of vortices known as leading edge vortices. These vortices generate a suction force on the upper side (leeward side) of the DW, and this suction force is responsible for the bulk of lift. The presence of the leading edge (primary) vortex leads to the formation of a secondary vortex that rolls in the opposite direction, and has a lesser strength. Figure 1.2 shows the vortical structure characteristic of the flow over a DW. The strength of the leading edge vortices increases with increasing angle of attack leading to an increase in lift. The aspect ratio of a DW, defined as the length of the span (b) squared divided by the area (S), is low, and because of that the its lift variation with angle of attack is lower than in a normal wing [7]. Lee (1990) [8] published an excellent study of the lift generation mechanism of DWs.

The stalling mechanism in DWs is not completely due to the flow separation from the

(a) Collins X-112

(b) X-114

(c) Airfish 1

(d) Airfish 3

Figure 1.1: Examples of Lippisch style WIG craft

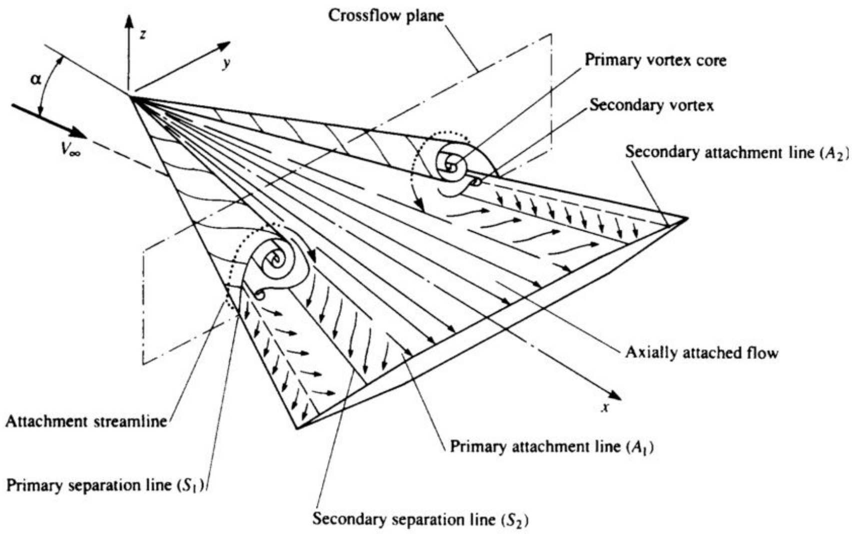

Figure 1.2: Vortical flow in a delta wing. Reproduced with permission from [9].

upper (leeward) side, but rather due to a phenomenon known as vortex breakdown. During vortex breakdown the cores of the leading edge vortices expand and become diffused inducing a pressure increase that produces a loss of suction, and consequently of lift. A well-known problem is the determination of the exact location of the vortex breakdown. Many criteria have been proposed in the literature, but we still are lacking a robust criterion. In figure 1.3 we see the different phases leading to a spiral breakdown of a vortex, while figure 1.4 shows a water tunnel visualization of the breakdown of the leading edge vortices over a DW.

Complex vortical patterns are obtained when the DW is set at high angles of attack. In figure 1.5 we see a visualization for the flow over a DW, and we can also see the visualization of the vortex shedding from the trailing edge of the wing.

Conventional DWs can be used for applications other than high performance flight, e.g. vortex alleviation. In the work done by Lee and Pereira (2013) [10] the vortex of a rectangular wing with a NACA 0012 section was modified by mounting a slender half DW at the tip, the results showed that adding the half DW modified the roll-up process for the tip vortex. By deflecting the half DW, lift increased, along with the total drag. The induced drag, however, decreased compared to the baseline wing. At high angles of attack, the lift to drag ratio improved. The modification of the wing tip roll-up process is due to the vortex breakdown over the attached half DW.

1.2.1.1 Numerical studies

A large number of scientific articles focus on numerical simulations of flows past DWs. A steady state simulation by AlGarni *et al.* (2008) [7] used FLUENT to simulate the flow about a DW of sweep angle 65° and a double DW with two sweep angles 65°/40°. The turbulence model used was the Spallart-Almaras. They did not only do a numerical simulation, but they also performed experiments in the wind tunnel and compared the numerical results to experimental data. Their numerical results showed good agreement with wind tunnel data in the pre-stall region, with a better agreement of the lift coefficient C_L than for the drag coefficient C_D. They also compared the numerical results of the spanwise pressure coefficient C_p variation with experimental data, and numerical results showed good agreement.

Other studies concentrated on the unsteady simulation of flows over a DW. Schiavetta *et al.* (2007) [14] compared the use of Unsteady Reynolds averaged Navier Stokes (URANS) turbulence models and Detached-Eddy simulation (DES) for unsteady vortical flows over DWs. They considered the test cases of the 70° ONERA and the 65° VFE-2 DWs and analyzed the velocity spectrum in the post-breakdown region. They also studied the effect of grid refinement and temporal resolution on the DES calculations. They detected different frequencies to be dominant in different locations in the flow, and those frequencies corresponded to phenomena such as oscillation of vortex breakdown location, shear layer instabilities and Kelvin-Helmholtz instability. Their conclusion was that URANS models captured the main frequencies accurately compared to DES for the same grid. Figure 1.6 shows the vorticity isosurface of the region post vortex breakdown colored by pressure coefficient C_p, and we see the vortex core expanding before its eventual breakdown.

Ludeke and Leicher (2008) [16] performed unsteady CFD simulations of a flow over a full DW fighter configuration. They used Delayed DES (DDES) and compared their results with the ones they obtained by DES, for time steps in the range 1×10^{-4} to 5×10^{-4} seconds.

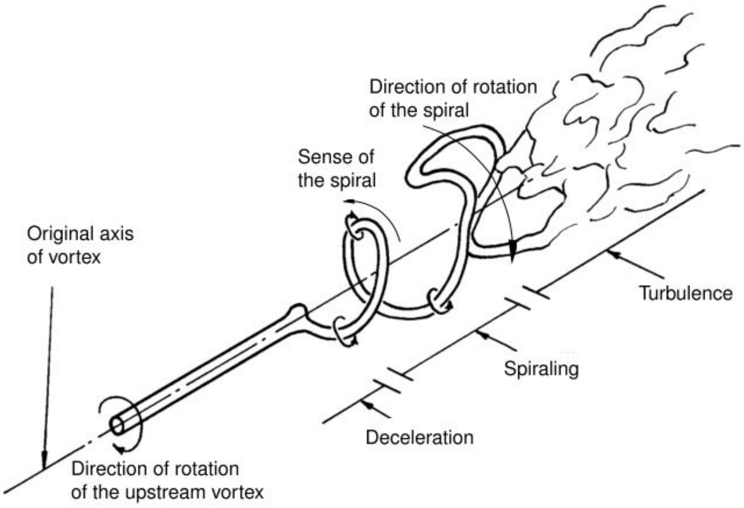

Figure 1.3: Schematic of a spiral vortex breakdown. Reproduced with permission from [11].

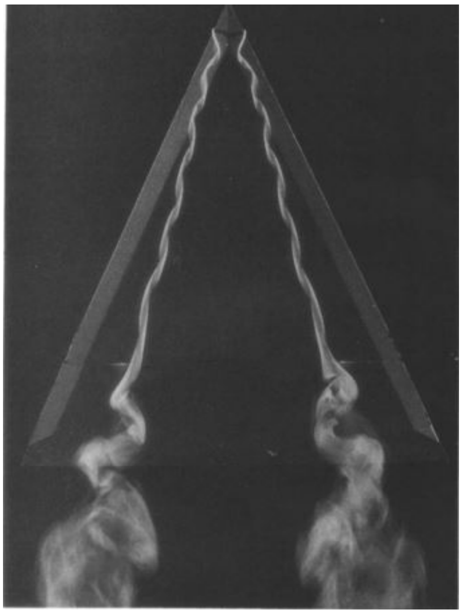

Figure 1.4: Water tunnel visualization of the breakdown of the leading edge vortices over a DW at angle of attack $\alpha = 20°$ and Reyonlds number $Re = 6500$. Reproduced with permission from [12].

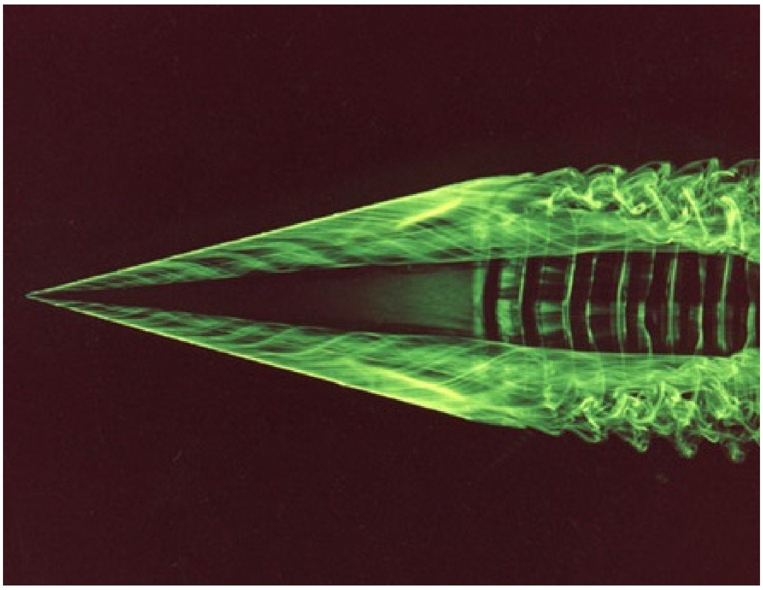

Figure 1.5: Water tunnel visualization of delta wing in free flight showing leading edge vortices and vortical structures at the trailing edge by using laser illuminated fluorescence dye. Reproduced with permission from [13].

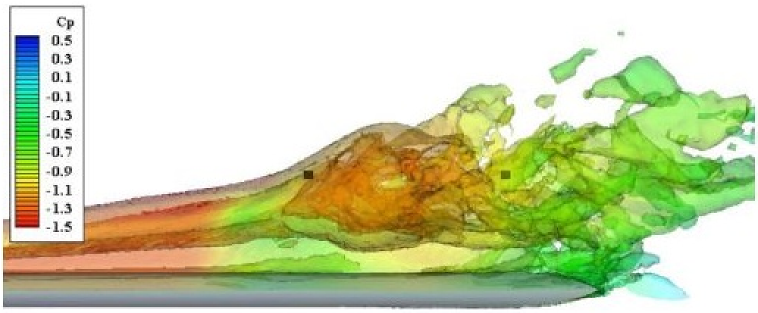

Figure 1.6: Iso-surface of constant vorticity magnitude colored by pressure coefficient C_p in the post vortex breakdown region over a DW. Reproduced with permission from [15].

They compared the the root mean square (rms) values of the turbulent velocity fluctuations obtained through the simulations to the ones obtained experimentally via PIV, concluding that DDES gave more accurate results than DES. They also computed the power spectral densities of the velocity fluctuations and found that DES over-predicted the magnitude of the PSD. Figure 1.7 shows the vorticity iso-surface obtained in their study by using DDES.

An excellent numerical simulation containing a physical description of the DW leading edge vortex breakdown phenomenon is due to Robertson *et al.* (2014) [17]. They compared the numerical simulations of the two CFD solvers: FLUENT and OpenFOAM. They also compared several turbulence models: the kω SST and the Delayed Detached Eddy Simulations (DDES) model by using Spallart Almaras or kω SST as a RANS model. The results from DES showed regions of massively helical flow in the DW leading edge vortex core, indicating a vortex breakdown. According to their findings, appearance of turbulence within the vortex core and the reversed axial flow are clear indications of a vortex breakdown. The use of different software and different turbulence models predicted different locations for the vortex breakdown. They concluded that FLUENT was not able to capture the vortex breakdown. Figure 1.8 shows the visualizations of the simulations performed with OpenFOAM and Fluent using the same turbulence model (DDES). clearly, only OpenFOAM predicted the occurrence of the vortex breakdown.

1.2.1.2 Unsteady vortical flow over delta wings

Several studies focused on the understanding and characterization of the unsteady vortical flow over a DW, as there are several unsteady phenomena associated with such flowfield. Research in this area is still ongoing as some phenomena are still not fully understood.

The flow about a regular DW is steady at angles of attack below 20°, because the leading edge vortex characteristics do not vary with time. Menke *et al.* (1999) [18] noted that the unsteady phenomena in the flow past a DW starts to appear at high angles of attack. Figure 1.9 shows the values of the Strouhal number associated with different unsteady phenomena. The unsteady phenomena in a flow over a DW include: oscillation of vortex breakdown location, vortex shedding, helical mode instability and shear layer instability. A schematic of the unsteady phenomena in the flow past a DW is shown in figure 1.10. Quantitative information about these phenomena can be obtained using experimental techniques such as hot wire and particle image velocimetry (PIV), while for a qualitative description, visualization techniques such as smoke tunnels, water tunnels and dye injection are used.

Rockwell (1993) [19] discussed the three-dimensional flow structure over a DW at high angles of attack. He categorized the different phenomena according to their time scale, with emphasis on flow control applications. Short time scale phenomena include: feeding sheet, vortex breakdown and near wake instabilities, while long time scale phenomena include: separation from the wing surface and vortex breakdown above the wing.

The most important unsteady phenomenon in the flow over DWs is the breakdown of the leading edge vortex, because it is associated with the stall of the wing. This phenomenon has been studied extensively [20, 21, 22, 23, 24, 25] and various criteria have been proposed to detect the location of the vortex breakdown. Indicators of the occurrence of a vortex breakdown include: expansion of the vortex core, reverse axial flow, turbulent vortex core, increase of core pressure, reversed axial vorticity and patches of vorticity instead of it being

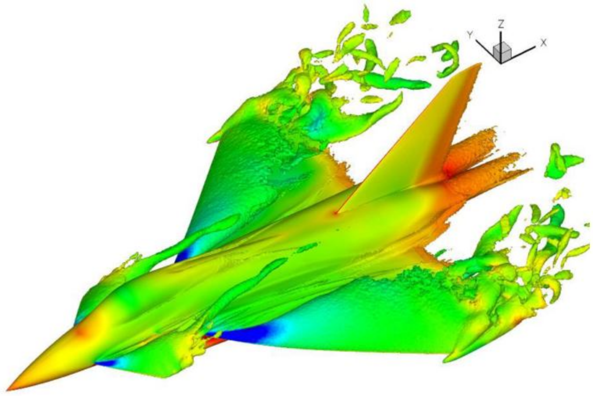

Figure 1.7: Iso-surface of constant vorticity magnitude colored in proportion to the value of the pressure coefficient C_p for a generic DW figter aircraft. Reproduced with permission from [16].

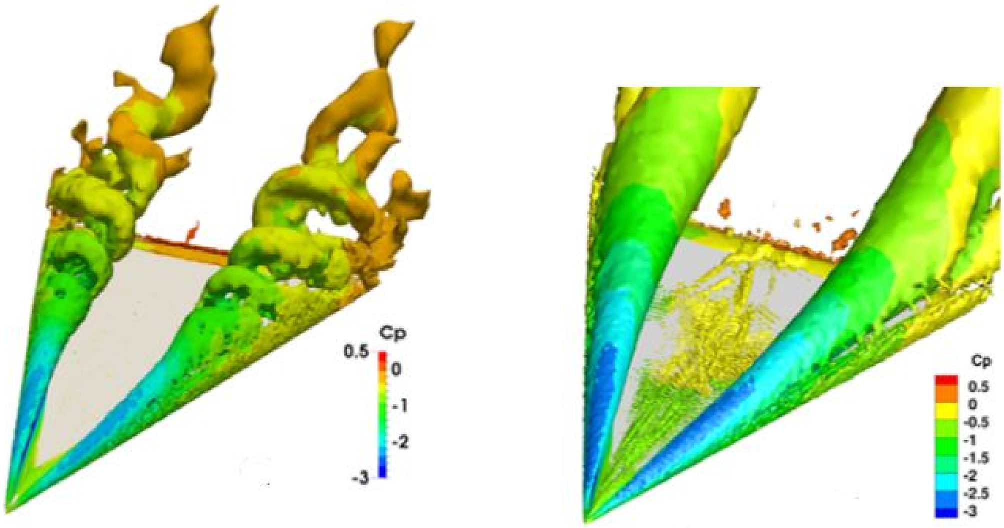

(a) Result obtained by OpenFOAM

(b) Result obtained by Fluent

Figure 1.8: Iso-surface of Q-criterion=2 colored in proportion to the value of the pressure coefficient C_p for a DW at an angle of attack $\alpha = 23°$. Reproduced with permission from [17].

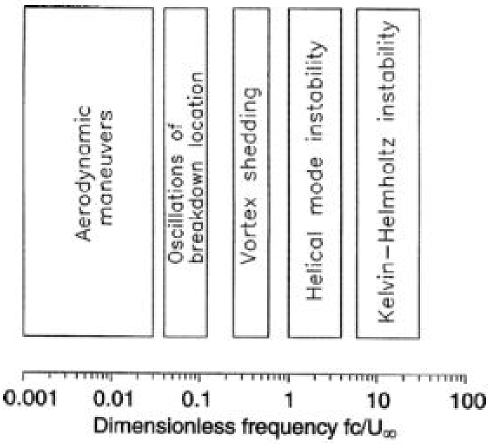

Figure 1.9: Stouhal numbers associated to unsteady phenomena over a DW compared with Strouhal number for aerodynamic maneuveres. Reproduced with permission from [18].

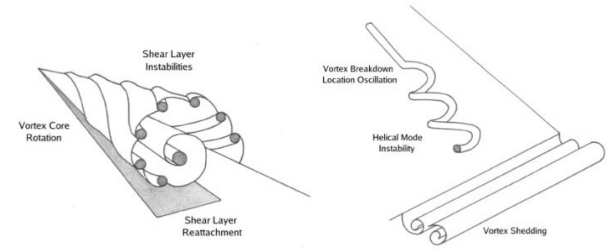

Figure 1.10: Schematic of unsteady phenomena in the flow over DW. Reproduced with permission from [14].

concentrated in the core.

Visbal (1995) [26] explained the physical and computational aspects of vortex breakdown in rather a different way. He suggested that the vortex breakdown mechanism emerges from the propagation of disturbances and their growth. In particular, there exist two main modes of vortex breakdown: the bubble mode and the spiral mode. In the bubble mode, a three-dimensional stagnation point is present in front of the region of reversed axial flow, while in the spiral mode such point is not present. Visbal also studied the influence of free stream Mach number M_∞ on the onset and structure of breakdown.

An excellent review of the vortex flows over slender DWs and the unsteady phenomena associated was provided by Gursul (2005) [27], where he explained some unsteady phenomena related to instabilities ranging from Strouhal number about 0.1 (large time scale), for phenomena like oscillation of vortex breakdown location, to values of about 10 (small time scale) for a phenomenon like Kelvin-Helmholtz instability.

Cummings *et al.* (2008) [28] provided clear guidelines for the best practices in performing numerical simulations of unsteady flows. They analyzed the effects of time step, grid sizing and refinement on unsteady simulations as well as the effect of using different turbulence models. They concluded providing a list of the best practices to obtain accurate results. Figure 1.11 shows the effect of using different grid sizes, with and without local grid refinement on the details of a DW leading edge vortex.

1.2.2 Reverse delta wings

Now we will consider the most relevant literature concerned with RDWs and their applications. As we mentioned earlier, due to the limited applications, literature concerning RDWs is not easily found.

1.2.2.1 Experimental studies

Urquhart *et al.* (2006) [5] studied the aerodynamics in ground effect of a Lippisch WIG craft having a configuration with a RDW. In particular, they focused on the effect of the ground on the wing tip vortices and the aerodynamic coefficients. They showed that the lift-to-drag ratio C_L/C_D increased considerably with reducing the ground clearance, up to a factor of 2. They concluded that the RDW configuration is the most stable in ground effect. Figure 1.12 shows the WIG craft tested in a wind tunnel.

Altaf *et al.* (2011) [29] studied experimentally by PIV the aerodynamics of a RDW at Reynolds number $Re = 3.82 \times 10^5$ and compared their results to the aerodynamics of a DW. They measured vortex characteristics such as maximum tangential velocity, vorticity and circulation distributions. The PIV results showed that the rollup process takes longer for the tip vortex of a RDW, and the RDW tip vortex exhibited a lower tangential velocity magnitude. In conclusion, the RDW had lower C_L and C_D values than the DW, but a higher value of aerodynamic efficiency C_L/C_D. They also concluded that one of the benefits of a RDW is the less adverse pressure gradient along the chord, contrary to the conventional DW.

Lee and Su (2012) [2] studied the aerodynamic performance of a conventional wing with a deflected half RDW mounted at its tip. They aimed to use the half RDW for passive control of the wing tip vortex. They found that with increasing deflection angle of the half

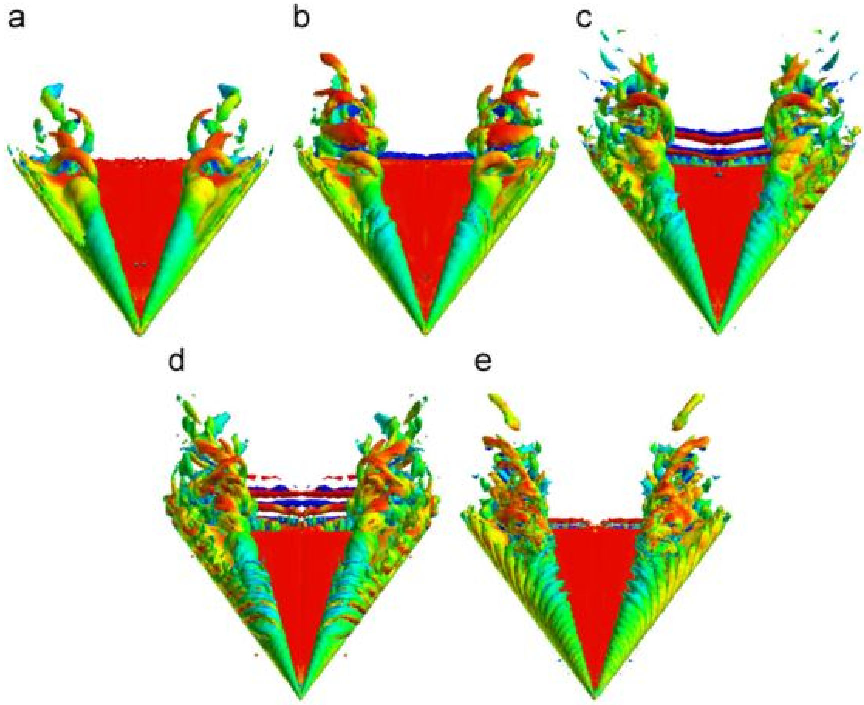

Figure 1.11: Effect of gird refinements on the vortical flwofield over a DW at an angle of attack $\alpha = 27°$. Reproduced with permission from [28].

Figure 1.12: WIG craft model mounted in a wind tunnel. Reproduced with permission from [5].

RDW, the lift produced by the wing increased nonlinearly, and so is the total drag. The deflected half RDW weakened the wing tip vortex compared to the one of the baseline wing, such that the wing tip vortex had lower vorticity levels and smaller peak tangential velocity. Regardless of the half RDW deflection, the induced drag was always reduced compared to the baseline wing.

Lee and Ko in 2016 [30] studied experimentally the aerodynamics and vortex flow of a RDW. They showed that the RDW stall angle was larger than a DW, but the RDW has a lower lift-to-drag ratio than a DW, which is contrary to the findings of [29]. The RDW wing tip vortex was located outside the wing, unlike the DW leading edge vortex, and the complete rollup happens at $x/c = 0.7$. Figure 1.13 shows a comparison of the vortex development for both the DW and RDW.

Another study by Lee (2016) [31] considered the impact of gurney flaplike strips on the flow characteristics of a RDW. He tested strips located at the leading edge and the wing sides with different deflection angles. The strips at the sides resembled a conventional trailing edge flap and had the effect of shifting the lift curve to the left, producing a large lift increment overwhelming the drag increase, which, in the end, led to a better lift to drag ratio. The wing tip vortex remained similar to the one generated by the baseline RDW, but with higher core vorticity and tangential velocity, which increase with strip height. On the other hand, the leading edge strips led to a diffused wing tip vortex and a reduction in lift coefficient C_L in the pre-stall region. The downward leading edge strips however increased the value of the the maximum lift coefficient C_{Lmax} which increases with the strip height.

Altaf *et al.* followed by several other studies utilizing the RDW for vortex alleviation applications. In 2016 [32], they studied the effect of a half RDW added to the ends of a conventional wing for wing tip vortex alleviation. In [33] they studied the effect of a similar device on the flap tip vortex. In 2017 Lee *et al.* [34] studied the effect of anhedral on a RDW. They found that the anhedral decreases the lift coefficient C_L and the aerodynamic efficiency C_L/C_D of a RDW.

Figure 1.14 shows a smoke visualization of the flowfield past a RDW performed by Ko in [1]. It shows that there are vortices that originate from the tips of the RDW that are similr to the tip vortices of a conventional wing. Ko [1] suggested that these vortices have no role in lift production by a RDW. Additional vortical structures in the form of "spanwise vortex filaments", referred to as "SVF" in figures 1.14 cover the upper surface of the RDW. At low angles of attack, the spanwise vortex filaments remain connected but are destroyed as the angle of attack increases leading to complex flow patterns over the upper surface of the RDW. Ko concluded that the lift produced by a RDW is not due to the wing tip vortices and that the stall of a RDW is connected to the destruction of the spanwise vortex filaments.

1.2.2.2 Numerical studies

To the best of our knowledge, the only published work presenting a numerical simulation of the flow past a RDW in a free stream is the work of Altaf *et al.* (2011) [29] which was extended with more details by Jamaluddin *et al.* (2015) [35]. They performed a numerical simulation for both a DW and a RDW and compared the results. The simulations were steady state and the turbulence model used was a RANS kε-model. Their results showed good agreement with experiments for the lift coefficient, but a less agreement for the values

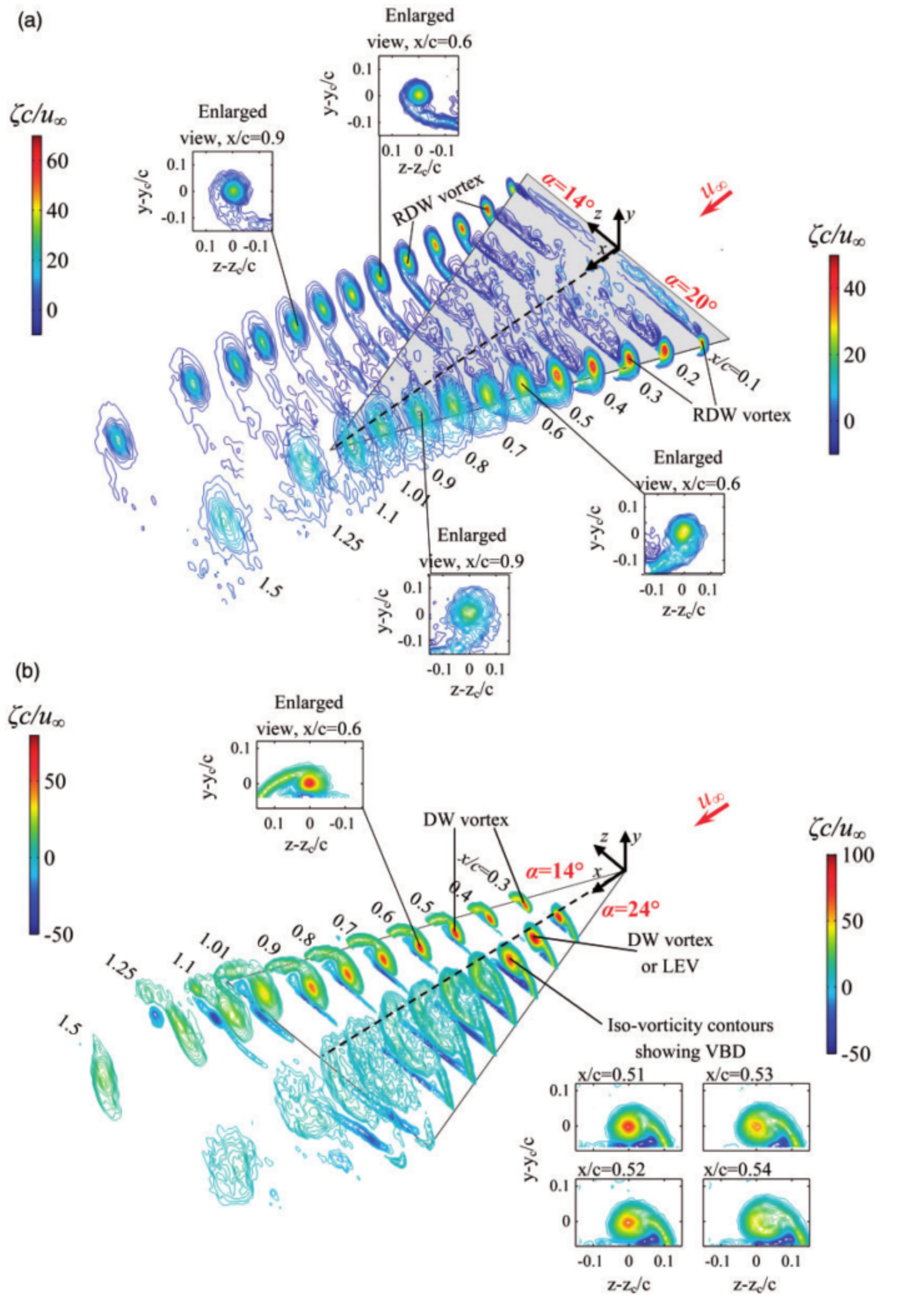

Figure 1.13: Comparison of the three-dimensional vorticity flowfield for the(a)RDW and (b)DW. Shown contours of normalized x-component of vorticity at different chordwise sections and for angles of attack $\alpha = 14°$ and $\alpha = 20°$ and $Re = 11 \times 10^3$. Reproduced with permission from [30].

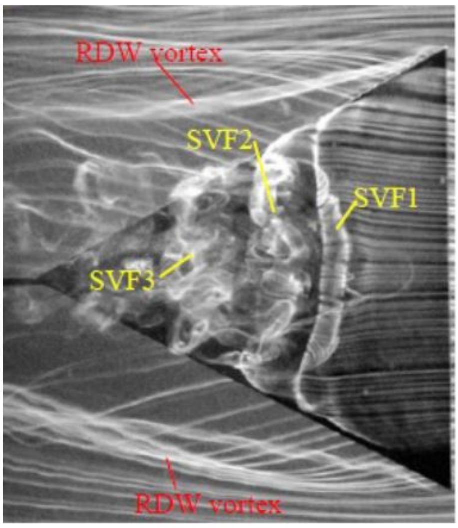

(a) $\alpha = 14°$

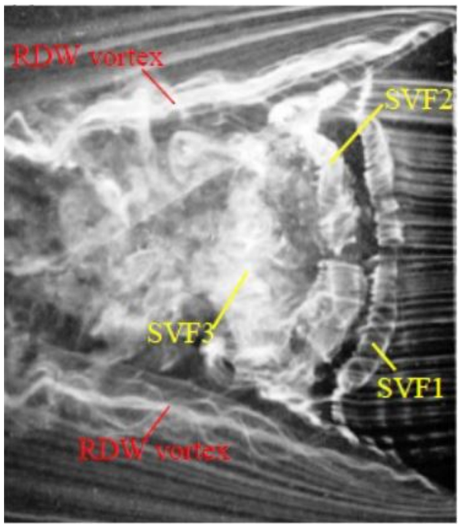

(b) $\alpha = 20°$

Figure 1.14: Smoke visualization of the flow past a RDW showing the RDW vortex and the spanwise vortex filaments SVF. Reproduced with permission from [1].

of drag coefficient. They concluded that the DW leading edge vortex generated higher circulation and had higher tangential velocity than the RDW tip vortex at angles of attack between 20° and 30°. They concluded that the turbulence model did not predict vortex size correctly. Comparing the flow visualizations shown in figure 1.14 and the streamlines visualization shown in figure 1.15, we notice major discrepancies. These discrepancies could be due to the steady state simulation performed to produce an unsteady flow and the use of kε turbulence model.

1.3 Motivations

A large body of litreature regarding DW is available and reflects the extensive use of DW, especially in military applications. The RDW, on the other hand, has not been studied as extensively as the DW, probably because of its limited use. Additionally, according to the findings of Lee and Ko [30], RDW performance in free stream is not superior to the conventional wing configurations. To the best of our knowledge, up to this date, there is a single published work on RDW including a visualization of the flow over a RDW by Lee and Ko (2016) [30], and only a steady state numerical study by Altaf *et al.* (2011) [29].

The lack of literature regarding the RDWs is the main motivation for this thesis. Thus, we would like to develop an understanding of the flow past a RDW, in particular lift mechanism and associated unsteady flow phenomena, both qualitatively and quantitatively. A deeper understanding of the flowfield over a RDW will not only help improving the designs of current Lippisch type WIG crafts, but it could also allow us to explore other areas where the RDW could find applications, such as passive flow control for wing tip vortex alleviation. This thesis is the first unsteady numerical study of the flow past a RDW.

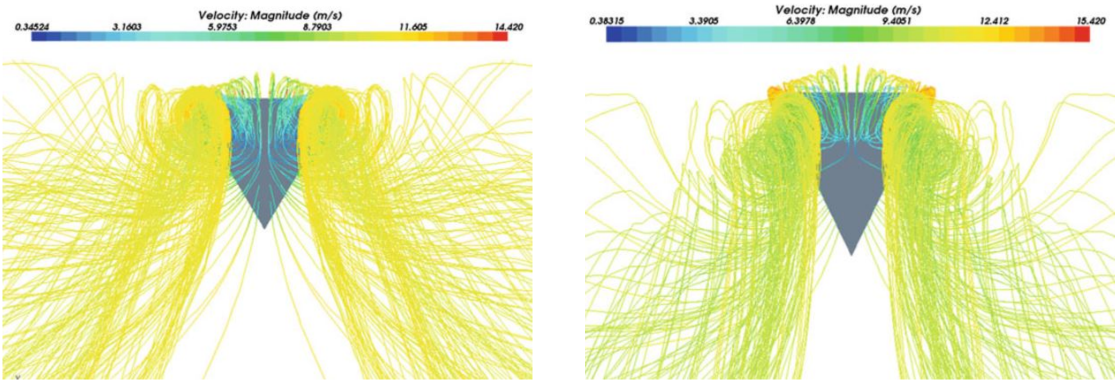

(a) $\alpha = 25°$

(b) $\alpha = 30°$

Figure 1.15: Flow streamlines colored by velocity magnitude for the flow over a RDW obtained by numerical simulations performed by [35]. Reproduced with permission.

1.4 Objectives

Now that we stated the motivations for this work, we discuss the main objectives of this thesis. First, we want to develop a numerical methodology suitable for analyzing the unsteady flowfield past a RDW. In addition, we want to develop an understanding for the lift generation mechanism in RDW and compare it to the one of regular DW. We also aim to verify the results of the numerical simulation by comparing them with available experimental data. Lastly, we want to compare the performance of the RDW to the DW.

1.5 Methodology

Due to the lack (non-existence) of methodology for analyzing the flow past a RDW, we start by applying methods that successfully simulate unsteady flows over DWs. We validate the results of our simulations against the experimental data provided by Ko [1] and Lee and Su [2].

First we generate a series of grids of different sizes to be tested in conjunction with a series of time steps in a sensitivity study to determine the most suitable combination of grid/time step for accurate simulations. To this end, we perform unsteady numerical simulations of the flow past a DW. The mesh selected is designed so that it can be used for both DWs and RDWs. The CFD simulations are performed using the commercial software ANSYS Fluent.

To validate our numerical methodology, we perform unsteady simulations of a flow past a DW and compare the results obtained with the experimental results [1, 2]. A successful validation of our methodology will allow us to perform numerical simulation of the unsteady flow past a RDW and compare the results with experimental data. The results from the numerical simulations allow us to analyze carefully and describe precisely the flowfield past a RDW. Finally, we will compare the performance of DW and RDW.

1.6 Structure of the thesis

The remaining of this thesis is organized as follows: In chapter 2 we present the methodology used to implement and perform the numerical simulations. In chapter 3, we present the results of our numerical simulations. We discuss the results obtained for the DW and RDW and compare them to experimental results. We then discuss the physics of the flowfield past the RDW. We conclude this chapter by comparing the performance of the DW and RDW. Finally, in chapter 4, we present our concluding remarks and our ideas for future work.

Chapter 2

Methodology for Numerical Simulations

This chapter presents the methodology used for simulating the flow over a DW and a RDW. We start by presenting the mathematical model and the type of discretization scheme employed by ANSYS Fluent. Subsequently, we describe the methodology used for mesh construction and time step selection. By the end of the chapter we show the results of the time step and grid sensitivity study and comment on them.

2.1 Mathematical model

In this section we will present the mathematical model that describes the fluid motion.

2.1.1 Navier-Stokes equations for incompressible flow

In the present work we simulate flows over DWs and RDWs at velocities low enough to neglect the effect of compressbility, i.e. flows with Mach number $M_\infty = \frac{U_\infty}{c_\infty} < 0.1$, where U_∞ is the free stream velocity and c_∞ is the sound speed at the free stream. Therefore, the equations that govern the motion of an incompressible viscous fluid over a DW are continuity and momentum equations [36]:

$$\begin{aligned} &\nabla \cdot \mathbf{u} = 0, \\ &\frac{\partial \mathbf{u}}{\partial t} + (\mathbf{u} \cdot \nabla)\mathbf{u} = -\frac{1}{\rho}\nabla p + \nu \nabla^2 \mathbf{u}, \end{aligned} \tag{2.1}$$

where $\mathbf{u} = [u, v, w]^T$ is the velocity vector, p is the pressure ,ρ is the density of the fluid and ν is the fluid kinematic viscosity.

We can find a relationship between the pressure and the velocity if we take the divergence of the momentum equation, and we get the Poisson's equations for the pressure as follows [36]:

$$\frac{1}{\rho}\nabla^2 p = -\nabla \cdot (\mathbf{u} \cdot \nabla)\mathbf{u}. \tag{2.2}$$

We can rewrite equations (2.1) in a dimensionless form by defining the non-dimensional independent variables as:

$$\hat{x} = \frac{x}{c},\ \hat{t} = \frac{tU_\infty}{c}, \tag{2.3}$$

where c, the wing mid chord, is the reference length. While the non-dimensional dependent variables are:

$$\hat{u} = \frac{u}{U_\infty},\ \hat{p} = \frac{p}{\rho_\infty U_\infty^2}, \tag{2.4}$$

where ρ_∞ is the fluid density at the free stream. Hence, the non-dimensional Navier Stokes equations are:

$$\begin{aligned} &\hat{\nabla} \cdot \hat{\mathbf{u}} = 0, \\ &\frac{\partial \hat{\mathbf{u}}}{\partial \hat{t}} + (\hat{\mathbf{u}} \cdot \hat{\nabla})\hat{\mathbf{u}} = \frac{1}{Re_\infty}\hat{\nabla}^2\hat{\mathbf{u}} - \hat{\nabla}\hat{p}, \end{aligned} \tag{2.5}$$

where Re_∞, the free stream Reynolds number, is:

$$Re_\infty = \frac{U_\infty c}{\nu}, \tag{2.6}$$

which represents a ratio of the fluid inertial forces to the viscous forces.

2.1.2 Unsteady Reynolds-Averaged Navier Stokes (URANS) equations

2.1.2.1 Turbulence

The momentum equation, the bottom equation in (2.1), is a nonlinear partial differential equation. The nonlinearity appears in the inertial term $(\mathbf{u} \cdot \nabla) \cdot \mathbf{u}$, and its effect increases with the fluid velocity $\mathbf{u}$. The effect of this nonlinear term is related to the value of the Reynolds number Re_∞. At very low values of Reynolds number, any disturbance in the flow is damped by viscous effects [15]. As the Reynolds number increases, disturbances in general, will be amplified and lead to instabilities, and the fluid flow will undergo transition from laminar to turbulent. Turbulence can be defined as an irregular, three dimensional fluid motion, with fluid quantities fluctuating rapidly both in space and time. Turbulent flows are found everywhere, and this includes flows past DWs and RDWs.

A numerical solution for the Navier Stokes equations (2.1) potentially can always be obtained by direct numerical simulation (DNS), however in our case, given the complexity of the flowfield, this approach would be computationally too expensive. Therefore we rely to turbulence modeling, where turbulence is resolved by computing the evolution of turbulent quantities with respect to a mean flow.

2.1.2.2 Reynolds decomposition

A turbulent flow is any pattern of fluid motion characterized by chaotic changes in pressure and fluid velocity. The best method to deal with such randomness is to use a statistical description. In order to describe statistically a turbulent flow, one can use Reynolds decomposition, where fluid variables are decomposed into a mean and a fluctuating parts [36]. In the case of a steady mean flow, a mean flow operator can be defined as:

$$\langle \mathbf{u}(\mathbf{x}) \rangle = \lim_{T \to \infty} \frac{1}{T} \int_0^T \mathbf{u}(\mathbf{x}, t)\, \mathrm{d}t. \tag{2.7}$$

Using this operator we can decompose the flow quantities as follows:

$$\begin{aligned} \mathbf{u}(\mathbf{x}, t) &= \langle \mathbf{u}(\mathbf{x}) \rangle + \mathbf{u}'(\mathbf{x}, t), \\ p(\mathbf{x}, t) &= \langle p(\mathbf{x}) \rangle + p'(\mathbf{x}, t), \end{aligned} \tag{2.8}$$

where the mean depends only on space, while the fluctuating parts depend both on space and time. Note that we define the fluctuating parts have a zero mean.

In the case of unsteady flows, in particular vortical flows such as the flows over DWs at high angles of attack or RDWs, the flow is inherently unsteady [15, 18, 27], as shown by typical values of the Strohaul number associated with the unsteady phenomena, see figure 1.9. In this case, the mean value operator is defined as:

$$\langle \mathbf{u}(\mathbf{x}, t) \rangle = \frac{1}{T} \int_t^{t+T} \mathbf{u}(\mathbf{x}, t)\, \mathrm{d}t, \tag{2.9}$$

where the sample time T is chosen to be much larger than the characteristic time of the small scales turbulent fluctuations, and at the same time it is much smaller than the period of mean flow oscillation. Applying the mean operator (2.9) to the fluid variables, we obtain the following unsteady Reynolds decomposition:

$$\begin{aligned} \mathbf{u}(\mathbf{x}, t) &= \langle \mathbf{u}(\mathbf{x}, t) \rangle + \mathbf{u}'(\mathbf{x}, t), \\ p(\mathbf{x}, t) &= \langle p(\mathbf{x}, t) \rangle + p'(\mathbf{x}, t). \end{aligned} \tag{2.10}$$

Laveraging the above decomposition, the Navier-Stokes equations (2.1) can be reduced to the Unsteady Reynolds-Averaged Navier-Stokes (URANS) equations [36]:

$$\begin{aligned} &\nabla \cdot \langle \mathbf{u} \rangle = 0, \\ &\frac{\partial \langle \mathbf{u} \rangle}{\partial t} + (\langle \mathbf{u} \rangle \cdot \nabla) \langle \mathbf{u} \rangle = -\frac{1}{\rho} \nabla \langle p \rangle + \nu \nabla^2 \langle \mathbf{u} \rangle - \nabla \cdot \langle \mathbf{u}' \otimes \mathbf{u}' \rangle, \end{aligned} \tag{2.11}$$

where both, the velocity fields of the mean flow $\langle \mathbf{u}(\mathbf{x}, t) \rangle$ and the fluctuating component $\mathbf{u}'(\mathbf{x}, t)$, are solenoidal. Note that the nonlinear term of the momentum equation (2.1) produces the divergence of the Reynolds stress tensor ($\langle \mathbf{u}' \otimes \mathbf{u}' \rangle$). This symmetric tensor represents the effect of the fluctuations on the mean flow.

Unlike Naiver-Stokes equations (2.1), RANS equations (2.11) don't need to resolve the turbulent motions. On the other hand, the Reynolds averaging process leads to more unknowns than equations, namely the Reynolds stress tensor components, the well known problem of closure of the (U)RANS equations.

2.1.3 Turbulence modeling

The problem of closure of the URANS equations can be solved by introducing additional equations that describe the statistics of the fluctuating quantities. The solution of these equations produces the Reynolds stress tensor. This procedure is known as turbulence modeling. Several turbulence models have been developed over the years, and most of them rely on the concept of eddy viscosity ν_t.

2.1.3.1 Turbulent viscosity hypothesis

We can decompose the Reynolds stress tensor into isotropic and anisotropic parts as follows [36]:

$$\langle \mathbf{u}' \otimes \mathbf{u}' \rangle = \frac{2}{3} k \mathbf{I} + \mathbf{D}, \tag{2.12}$$

where k is the turbulent kinetic energy. The isotropic part $\frac{2}{3}k\mathbf{I}$ acts as a pressure (normal stresses), while the anisotopic part $\mathbf{D}$ contains the shear stresses due to turbulent motion, and we can define the kinetic energy of the turbulent velocity fluctuations k as [36]:

$$k = \frac{1}{2} \langle \mathbf{u}' \cdot \mathbf{u}' \rangle. \tag{2.13}$$

The conecpt of turbulent (eddy) viscosity was introduced by Boussinesq, which assumed that a turbulent flow behaves like a Newtonian fluid, so that the shear stresses due to turbulent motion are linearly related with the mean velocity gradients, and the constant of proportionality is the eddy viscosity. Since only the anisotropic part is responsible for the shear stresses it can be writtin as follows [36]:

$$\mathbf{D} = -\nu_t(\mathbf{x}, t)(\nabla \langle \mathbf{u} \rangle + (\nabla \langle \mathbf{u} \rangle)^T). \tag{2.14}$$

Note that ν_t is not a constant, like the kinematic viscosity ν, but rather a function of time and space, which depends on the turbulent flow motion at that given location and instant of time. To evaluate ν_t it can used the formula [36]:

$$\nu_t(\mathbf{x}, t) = u^*(\mathbf{x}, t) l^*(\mathbf{x}, t), \tag{2.15}$$

where u^* and l^* are the velocity and length scales of the turbulent flow motion at location $\mathbf{x}$ and time t.

Finally, substituting the expression for the Reynolds stress tensor (2.12) in the URANS equations (2.11), and using the turbulent viscosity hypothesis (2.14), we obtain:

$$\begin{aligned} &\nabla \cdot \langle \mathbf{u} \rangle = 0, \\ &\frac{\partial \langle \mathbf{u} \rangle}{\partial t} + (\langle \mathbf{u} \rangle \cdot \nabla) \langle \mathbf{u} \rangle = -\frac{1}{\rho} \nabla (\langle p \rangle + \frac{2}{3} \rho k) + (\nu + \nu_t) \nabla \cdot (\nabla \langle \mathbf{u} \rangle + (\nabla \langle \mathbf{u} \rangle)^T). \end{aligned} \tag{2.16}$$

The above set of equations is still not closed, because the eddy viscosity should be specified. However this problem is much simpler than the problem evaluating all the components of the Reynolds stress tensor.

2.1.3.2 Eddy viscosity models

We can classify the turbulence models that rely on the eddy viscosity concept into the following: 0-equation (algebraic) models; 1-equation models; 2-equations models. This classification is in accord to the method used to estimate the velocity and length scales required to evaluate the eddy viscosity.

The algebraic models, which use algebraic equations to determine length and velocity scales, are the simplest. These models rely on empirical equations and constants that are obtained by studying a specific basic flow, therefore they are appropriate only for a small set of specific flows and cannot be generalized.

The one-equation models, that use an evolutive transport equation for one turbulent quantity (for example, the turbulent kinetic energy k or the eddy viscosity ν_t), are more accurate than the algebraic models because they use a more physical approach to determine the turbulent length and velocity scales. Nontheless, these models are in general incomplete, because they cannot evaluate u^* and l^* with a sinle equation. The only 1-equation model that is considered complete is the Spalart-Allmaras model, because it solves a transport equation directly for the eddy viscosity, without evaluating the velocity and length scales [36].

Lastly, the two-equations models solve two transport equations for two turbulent quantities, relate those quantities to the velocity and length scales and determines the eddy viscosity ν_t.

The most commonly used 2-equations model is the kε-model which solves 2 transport equations, one for the turbulent kinetic energy k and the other for the dissipation rate of turbulent kinetic energy ε, which is defined as:

$$\varepsilon = -\frac{dk}{dt}. \tag{2.17}$$

The transport equations for k and ε can be obtained by manipulating the URANS equations (2.11). However the equations in their original form (details can be found in [36]) cannot be solved, as they contain some terms that are need modeling. Hence, some assumptions are made in order to make the equations solvable. In the kε-model, the eddy viscosity is obtained using the following relationship:

$$\nu_t = C_\mu \frac{k^2}{\varepsilon}, \tag{2.18}$$

where C_μ is one of the kε-model constants.

The kε-model has some drawbacks, one of which is its inability of resolving the flow in the near wall region. Many modifications to the kε-model have been proposed over the years, some of which include varying the values of the constants of the model, while others modify the ε equation by adding a source term that acts as an ad-hoc correction.

The Wilcox kω-model is similar, in principle, to the kε-model. The only difference is that it solves for the specific dissipation rate ω instead of the dissipation rate ε, where ω is defined as:

$$\omega = \frac{\varepsilon}{k}. \tag{2.19}$$

For boundary layer flows, this model behaves better than kε-model in the near wall region and in regard of the effects of streamwise pressure gradient [36].

2.1.3.3 Menter's kω SST turbulence model

The kω Shear Stress Transport (SST) model propsed by Menter 1994 [37], is a modified version of the original kω-model. It combines the kε and the original kω models by using the kω- model in the near wall region and the kε-model in the region far from wall. In our simulations the kω SST model has been used. Detailed formulation of the kω SST model can be found from [38]. The two equations implementing this model are:

$$\underbrace{\frac{\partial k}{\partial t}}_{\text{Unsteady term}} + \underbrace{\langle u \rangle_i \frac{\partial k}{\partial x_i}}_{\text{Convection}} = \underbrace{\tilde{P}_k}_{\text{Production}} - \underbrace{\beta^\star k \omega}_{\text{Destruction}} + \underbrace{\frac{\partial}{\partial x_i}\left[(\nu + \sigma_k \nu_t)\frac{\partial k}{\partial x_i}\right]}_{\text{Turbulent and viscous diffusion}}, \tag{2.20}$$

$$\begin{aligned}\frac{\partial \omega}{\partial t} + \langle u \rangle_i \frac{\partial \omega}{\partial x_i} =& \alpha S^2 - \beta \omega^2 + \frac{\partial}{\partial x_i}\left[(\nu + \sigma_\omega \nu_t)\frac{\partial \omega}{\partial x_i}\right] \\ &+ \underbrace{(1 - F_1)\sigma_{\omega 2}\frac{1}{\omega}\frac{\partial k}{\partial x_i}\frac{\partial \omega}{\partial x_i}}_{\text{Cross diffusion}}.\end{aligned} \tag{2.21}$$

Note that equations have the same structure: on the left-hand-side there is the unsteady and convective terms, while on the right-hand-side we have the production, destruction and diffusion (both due to turbulent fluctuations and viscosity) terms. The only difference among these equations lies in the last term of the ω-equation, the cross diffusion coupling term, which is missing in the k-equation. The term $\tilde{P}_k$ represents the production of turbulent kinetic energy. The production is defined as:

$$\begin{aligned}\tilde{P}_k &= \min(P_k, 10.\beta^\star k \omega), \\ \text{where } P_k &= \nu_t \frac{\partial \langle u \rangle_i}{\partial x_j}\left(\frac{\partial \langle u \rangle_i}{\partial x_j} + \frac{\partial \langle u \rangle_j}{\partial x_i}\right),\end{aligned} \tag{2.22}$$

and F_1 is the first blending function, which is responsible for switching between the original kω-model and the kε-model. F_1 is equal to zero far from walls (kε-model) and is equal to one inside the boundary layer (kω-model), and is defined as:

$$F_1 = \tanh\left\{\left\{\min\left[\max\left(\frac{\sqrt{k}}{\beta^\star \omega y}, \frac{500\nu}{y^2\omega}\right), \frac{4\rho\sigma_{\omega 2} k}{CD_{k\omega} y^2}\right]\right\}^4\right\}, \tag{2.23}$$

where $\sigma_{\omega 2}$ is a constant of the kω SST model, y is the distnace from the wall, and $CD_{k\omega}$ stands for the positive portion of the cross diffusion-term (last term in (2.21)), and has the following form [39]:

$$CD_{k\omega} = \max\left(\frac{2}{\sigma_{\omega 2}\omega}\frac{\partial k}{\partial x_j}\frac{\partial \omega}{\partial x_j}; CD_{k\omega\,\min}\right). \tag{2.24}$$

Note that the argument of the blending function F_1 is $\frac{\sqrt{k}}{\omega y}$ which is a ratio between an internal length scale of the kω-model and the distance y from the wall.

Once the values of k and ω are known, the turbulent eddy viscosity ν_t can be estimated as:

$$\nu_t = \frac{a_1 k}{\max(a_1\omega, SF_2)}., \tag{2.25}$$

where a_1 is a constant taken to be equal to 0.31 [39], and F_2 is a second blending function and S is a scalar measure of the strain rate, and can be estimated as [39]:

$$\begin{aligned} S &= \sqrt{2S_{ij}S_{ij}}, \\ \text{where } S_{ij} &= \frac{1}{2}\left(\frac{\partial u_i}{\partial x_j} + \frac{\partial u_j}{\partial x_i}\right), \end{aligned} \tag{2.26}$$

and

$$F_2 = \tanh\left[\left[\max\left(\frac{2\sqrt{k}}{\beta^\star \omega y}, \frac{500\nu}{y^2\omega}\right)\right]^2\right]. \tag{2.27}$$

All the model constants are computed using the blending function F_1 in order to give constants that are a blend of both the $k\varepsilon$ and $k\omega$ models [38], for example if we consider the constant α the blend form will be:

$$\alpha = \alpha_1 F_1 + \alpha_2(1 - F_1). \tag{2.28}$$

Table 2.1 presents the constants used in the kω SST model, where the subscripts 1 and 2 refer to the constants corresponding to the $k\varepsilon$- or $k\omega$- models, respectively.

Table 2.1: kω SST turbulence model constants [38]

Constant	$\beta^\star$	α_1	β_1	σ_{k1}	$\sigma_{\omega 1}$	α_2	β_2	σ_{k2}	$\sigma_{\omega 2}$
Value	0.09	5/9	3/40	0.85	0.5	0.44	0.0828	1	0.856

2.1.3.4 Curvature correction for the kω SST model

Flows past DWs and RDWs are characterized by coherent vortical structures having, of course, and the maximum values of vorticty at the vortex core. The large values of vorticity lead to large values of eddy viscosity ν_t within the vortex core, which in turn lead to an excess of dissipation of turbulent quantities. Hence, an ad-hoc correction is needed in order to simulate correctly flows dominated by coherent vortical structures.

In order to apply the curvature correction to the kω SST turbulence model we need to multiply the production term both in the k and ω equations ((2.20) and (2.21)) by an empirical function f_{r1}, defined as follows (For details see [40]):

$$\begin{aligned} f_{r1} &= \max\{\min(f_{rotation}, 1.25), 0\}, \\ f_{rotation} &= (1 + c_{r1})\frac{2r^*}{1 + r^*}[1 - c_{r3}\tan^{-1}(c_{r2}\tilde{r})] - c_{r1}, \end{aligned} \tag{2.29}$$

where $f_{rotation}$ is an empirical correction function that accounts for streamline curvature and system rotation. The values of the constants are: $c_{r1} = 1.0, c_{r2} = 2.0$ and $c_{r3} = 1.0$, and:

$$\begin{aligned} r^* &= \frac{S}{\Omega}, \\ \tilde{r} &= 2\Omega_{ik}S_{jk}\left[\frac{DS_{ij}}{Dt} + (\varepsilon_{imn}S_{jn} + \varepsilon_{jmn}S_{in})\Omega_m^{rot}\right]\frac{1}{\Omega D^3}, \end{aligned} \tag{2.30}$$

where ε is the dissipation rate tensor, S_{ij} and S are the strain rate tensor and its scalar measure which were defined previously. Note that DS_{ij}/Dt are the components of the Lagrangian derivative of the strain tensor, Ω_m^{rot} is the rotation rate in the case of a rotating reference frame and:

$$\begin{aligned} \Omega_{ij} &= \frac{1}{2}\left(\left(\frac{\partial u_i}{\partial x_j} - \frac{\partial u_j}{\partial x_i}\right) + 2\varepsilon_m ji\Omega_m^{rot}\right), \\ \Omega^2 &= 2\Omega_{ij}\Omega_{ij}, \\ D^2 &= \max(S^2, 0.09\omega^2). \end{aligned} \tag{2.31}$$

2.1.3.5 Large-Eddy simulation (LES)

Large Eddy Simulation (LES) solves Navier-Stokes equations with an accuracy better than full RANS modeling and worse than a direct numerical solution (DNS). In LES the larger three-dimensional unsteady turbulent scales are fully resolved, while the effect of smaller scales is modeled. Hence the computational cost of LES is between RANS and DNS. The greatest advantage is that it is based on physical grounds and requires less assumptions than RANS model. Furthermore, since LES resolves more scales, a LES solution comes closer to DNS solution of the same problem[36]. Therefore, LES is more accurate and reliable than eddy viscosity models in simulating flows dominated by large vortical structures such as flows over DWs at high angles of attack.

The procedure for deriving LES can be summarized in 4 main steps [36]:

1. Filtering, where the velocity $\mathbf{u}(\mathbf{x}, t)$ is decomposed into the sum of a filtered (resolved) component $\overline{\mathbf{u}}(\mathbf{x}, t)$ and a residual (modeled) component $\mathbf{u}'(\mathbf{x}, t)$.
2. The equations for the evolution of the filtered variables are derived from the Navier-stokes equations.
3. Closure of the equations is obtained by modeling the residual stress tensor.
4. The filtered equations are solved numerically for $\overline{\mathbf{u}}(\mathbf{x}, t)$.

A general filtering operation can be defined as [36]:

$$\overline{\mathbf{u}}(\mathbf{x}, t) = \int G(\mathbf{r}, \mathbf{x})\mathbf{u}(\mathbf{x} - \mathbf{r}, t)\,\mathrm{d}\mathbf{r}, \tag{2.32}$$

where $G(\mathbf{r}, \mathbf{x})$ is the filtering function that filters out the scales that should not be resolved by the LES formulation. Therefore, the residual field is defined as:

$$\mathbf{u}'(\mathbf{x}, t) = \mathbf{u}(\mathbf{x}, t) - \overline{\mathbf{u}}(\mathbf{x}, t). \tag{2.33}$$

Note that this residual velocity field $\mathbf{u}'(\mathbf{x}, t)$ plays a similar role as the fluctuating part in the RANS formulation.

Applying this decomposition to the Navier stokes equations (2.1) generates the filtered continuity and momentum equations:

$$\begin{aligned} &\nabla \cdot \overline{\mathbf{u}} = 0, \\ &\frac{\partial \overline{\mathbf{u}}}{\partial t} + (\overline{\mathbf{u}} \cdot \nabla)\overline{\mathbf{u}} = -\frac{1}{\rho}\nabla\overline{p} + \nu\nabla^2\overline{\mathbf{u}} - \nabla \cdot \boldsymbol{\tau}^r, \end{aligned} \tag{2.34}$$

where τ^r is the residual stress tensor representing the turbulent motion not resolved by the LES model, which is analogous, in role, to the Reynolds stress tensor present in RANS model.

In order to close the LES problem 2.34, the residual strsses tensor τ^r should be modeled. This is accomplished by using a formulation similar to the eddy viscosity formulation, the only difference being that this formulation is applied only to the small scales not resolved by LES, and not all the scales as in the URANS model. Hence, the residual stress tensor can be related to the filtered rate of strain as follows:

$$\tau^r_{ij} = -2\nu_t(\mathbf{x}, t)\overline{S_{ij}}, \tag{2.35}$$

where $\nu_t(\mathbf{x}, t)$ is the eddy viscosity of the residual velocity field. Smagorinsky [36] suggested this formulation:

$$\nu_t = {l_S}^2\overline{S} = (C_S\Delta)^2\overline{S}, \tag{2.36}$$

where l_S is the Smagorinsky length scale, C_S is the Smagorinsky constant and Δ is the LES filter width. Many variants to this formulation have been developed where the constant C_S varies over different regions of the flow. Further details can be found in [36].

2.1.3.6 Detached-Eddy simulation (DES)

As we discussed in the previous subsection, LES computational cost is less than performing a DNS, however it is still too large for our applications. DES is a hybrid model that combines LES and a RANS model. DES has a lower computational cost than LES and was first suggested by Spalart 1997 in [41]. DES uses the RANS model close to the wall , i.e. in a boundary layer region of thickness d, and the LES model far from the boundaries. Figure 2.1 shows an example of DES formulation on a structured grid.

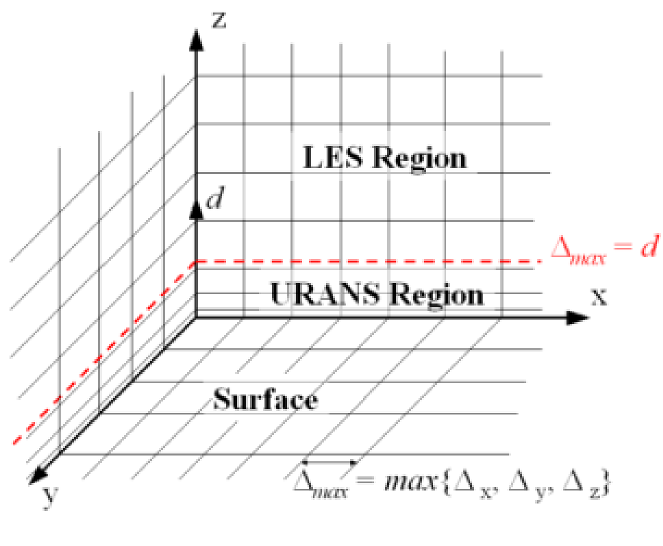

Figure 2.1: Formulation of DES on a structured grid. Reproduced with permission from [15]

Note that only two RANS models, the Spalart-Allmaras and the kω-SST models, can be used to formulate a DES model. In our work we will use the kω-SST model.

The formulation of the DES model leads to the modifications of some of the equations for the kω-SST model. The dissipation term in the k-equation (2.20) becomes:

$$\varepsilon = \beta^{\star} k \omega F_{DES}, \tag{2.37}$$

where F_{DES} is a limiter used in the DES formulation:

$$F_{DES} = \max\left(\frac{l^*}{C_{DES}\Delta}, 1\right), \tag{2.38}$$

The turbulent length scale l^* is defined as

$$l^* = \frac{\sqrt{k}}{\beta^{\star}\omega}, \tag{2.39}$$

where $\beta^{\star}$ is a coefficient used in the kω-SST model, Δ is the maximum local grid spacing:

$$\Delta = \max(\Delta x, \Delta y, \Delta z), \tag{2.40}$$

and $C_{DES} = 0.61 - 0.65$ is a calibration constant which is calibrated by using the decay of isotropic turbulence [16].

2.1.3.7 Delayed Detached-Eddy Simulation (DDES)

An improvement to the DES formulation is the Delayed DES (DDES) model, which avoids a predefined zonal selection by leaving it to the solution process to determine the separation between the wall regions where the URANS model is used and the outer regions where the LES model is used. DDES detects boundary layers, and accordingly switches between the full RANS and LES models [42].

The kω SST model has the potential for being the best model to be used in conjunction with DDES. The blending functions, F_1 and F_2, which are used to determine where to apply either the kε- or kω- models, as they are equal to 1 in the boundary layer regions and fall rapidly to 0 at edges of these regions. If the kω-SST model is used as a RANS model for DES, the bleding functions can be used in DDES as indicators for the presence of boundary layer regions [43].

Other eddy viscosity models, that do not use blending functions, such as the Spalart-Allmaras model, use a parameter r_f, that acts similarly to a blending function, which is defined as:

$$r_f = \frac{\nu_t + \nu}{\sqrt{U_{i,j}U_{i,j}}\kappa^2 d^2}, \tag{2.41}$$

where $U_{i,j}$ is the velocity gradient tensor, κ is the von Karman constant and d is the distance to the wall. In analogy to the blending functions, this parameter is equal to 1 in the boundary layer region and falls to 0 as it approaches the edge of the boundary layers. It is used to evaluate the delaying function f_d:

$$f_d = 1 - \tanh([8r_f]^3). \tag{2.42}$$

The value of f_d is 1 in the LES region (corresponds to $r_f << 1$) and 0 in boundary layer regions. Note that when using the kω-SST as a RANS model in DDES, one can use either of the blending functions F_1,F_2, or the delaying function f_d to act as an indicator for the different regions.

2.2 Numerical solution

2.2.1 Philosophy of the finite volume method (FVM)

Finite volume method (FVM) is a numerical method used for solving transport equations. In integral forms of these equations, the domain is discretized into a number of cells that surround nodes located in the center of every cell, with each cell having a specific volume. The integral form of the transport equation is integrated over the closed boundary of the control volume surrounding the node, and the surface integrals are evaluated at the faces of the cell separately [44]. Figure 2.2 shows an example for a node surrounded by a control volume.

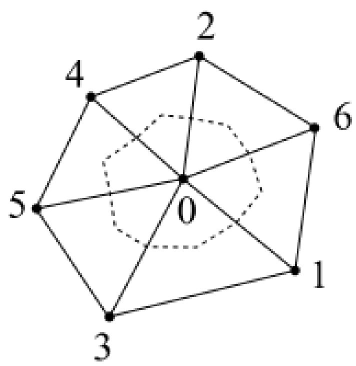

Figure 2.2: The control volume surrounding a generic node. Reproduced with permission from [44]

.

2.2.2 Generic scalar transport equation

A generic transport equation for a scalar quantity ϕ convected with a velocity $\mathbf{u}$ has the following form [45]:

$$\underbrace{\frac{\partial(\rho\phi)}{\partial t}}_{\text{Unsteady term}} + \underbrace{\nabla\cdot(\rho\phi\mathbf{u})}_{\text{Convection}} = \underbrace{\nabla\cdot(\Gamma_\phi\nabla\phi)}_{\text{Diffusion}} + \underbrace{S_\phi}_{\text{Source term}} \quad , \tag{2.43}$$

where Γ_ϕ is the diffusion coefficient for the scalar ϕ, ρ is its corresponding density, and S_ϕ is a source term. By integrating over a control volume V and using Gauss divergence theorem, we can obtain the corresponding integral form [45]:

$$\iiint_V \frac{\partial(\rho\phi)}{\partial t}\,\mathrm{d}V + \iint_{CS} \mathbf{n}\cdot(\rho\phi\mathbf{u})\,\mathrm{d}S = \iint_{CS} \mathbf{n}\cdot(\Gamma_\phi\nabla\phi)\,\mathrm{d}S + \iiint_V S_\phi\,\mathrm{d}V, \tag{2.44}$$

where CS is the control surface enclosing the control volume CV.

The URANS equations (2.11) and the equations for the kω-SST turbulence model (2.20) and (2.21) are all in the form of (2.43), and, therefore, they can be rewritten in the integral form (2.44).

2.2.2.1 Finite volume discretization of a generic scalar transport equation

Equation (2.44) is solved by finite volume method by discretizing the computational domain to a finite number of cells having a specific geometry. We proceed with spatial discretization, assuming that we can discretize in space and time separately, hence we take the steady state version of (2.44) and consider a cell with a control volume CV. The integral form of the equation is [45]:

$$\sum_{i}^{N_{faces}} \iint\limits_{\Delta A_i} \mathbf{n}_i \cdot (\rho\phi\mathbf{u})\,\mathrm{d}A = \sum_{i}^{N_{faces}} \iint\limits_{\Delta A_i} \mathbf{n}_i \cdot (\Gamma_\phi \nabla\phi)\,\mathrm{d}A + \iiint\limits_{CV} S_\phi\,\mathrm{d}V, \tag{2.45}$$

where ΔA_i is the ith-face surface area and $\mathbf{n}_i$ is a unit vector with a direction normal to the corresponding surface. In the equation above we have terms that require the knowledge of the values of the property ϕ at the cell surfaces. Additionally, the discretization of the the diffusion term requires the evaluation of the gradient of ϕ at the cell surfaces, i.e. the fluxes of ϕ.

To illustrate how each term in (2.45) is discretized, we consider the cells arrangement shown in figure 2.3. The figure shows two adjacent triangular cells with their centroids at points P and A, and the line ab of length $\Delta\eta$ separates them.

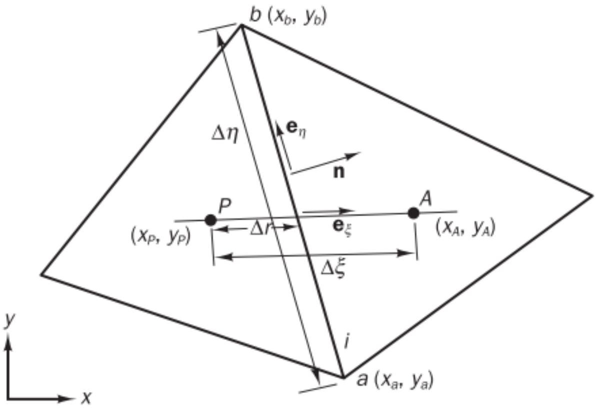

Figure 2.3: Cell centered control volume arrangement. Reproduced with permission from [45].

In figure 2.3 $\mathbf{n}$ is the direction normal to the line ab, and $\mathbf{e}_\eta$ is the direction parallel to it, while $\Delta\xi$ is the length of the line connecting A and P and $\mathbf{e}_\xi$ is the direction of that line.

The following is discretization methodology used in conjunction with either 2D or 3D unstructured grids and it is the same methodology implemented in ANSYS Fluent.

Diffusion term The discretization of the diffusion term for the control volume gird shown in figure 2.3 can be done by using a central difference scheme [45]:

$$\begin{aligned}\iint\limits_{\Delta A_i} \mathbf{n}_i \cdot (\Gamma_\phi \nabla\phi)\,\mathrm{d}A &\cong \mathbf{n}\cdot\nabla\phi\Delta A_i \\ &= D_i(\phi_A - \phi_P) + S_{D-cross,i},\end{aligned} \tag{2.46}$$

where ϕ_A and ϕ_P are the values of the scalar field ϕ at the cell centroids A and P. The term D_i is the diffusive flux parameter for the ith-face, and $S_{D-cross,i}$ is the corresponding cross diffusion term, having the from:

$$\begin{aligned}D_i &= \frac{\Gamma_\phi}{\Delta\xi}\frac{\mathbf{n}\cdot\mathbf{n}}{\mathbf{n}\cdot\mathbf{e}_\xi}\Delta A_i, \\ S_{D-cross,i} &= -\Gamma_\phi\frac{\mathbf{e}_\xi\cdot\mathbf{e}_\eta\Delta A_i}{\Delta\xi}\frac{\mathbf{n}\cdot\mathbf{n}}{\mathbf{n}\cdot\mathbf{e}_\xi}\frac{\phi_b-\phi_a}{\Delta\eta}.\end{aligned} \tag{2.47}$$

The diffusion term (2.46) is discretized, and the only unknowns are the values of ϕ at the cells centroids and at the face between them.

Convective term We can define a convective flux parameter F_i as [45]:

$$F_i = \iint\limits_{\Delta A_i} \mathbf{n}_i \cdot (\rho\mathbf{u})\,\mathrm{d}A \cong \mathbf{n}_i\cdot(\rho\mathbf{u})\Delta A_i. \tag{2.48}$$

If a suitable interpolated value for the convection velocity at the ith-face is available, the convective flux can be rewritten as [45]:

$$\sum_i^{N_{faces}} \iint\limits_{\Delta A_i} \mathbf{n}_i\cdot(\rho\phi\mathbf{u})\,\mathrm{d}A = \sum_i^{N_{faces}} F_i\phi_i, \tag{2.49}$$

where ϕ_i is the value of ϕ at the center of the ith-face.

To calculate the convective flux, it is more convenient to use an upwind difference scheme, where the values used for the approximation depend on the direction of the flux parameter F_i, for example, the convective flux using the simplest upwind scheme is (see figure 2.3):

$$\phi_i = \begin{cases}\phi_P, & \text{for } F_i > 0 \\ \phi_A, & \text{for } F_i < 0\end{cases}$$

Note that in this thesis, we use second-order upwind scheme for evaluating the value ϕ_i at the face surface of the grid cell. We will discuss these schemes in section 2.2.2.2.

Source term The source term is discretized as follows:

$$\iiint\limits_{CV} S_\phi\,\mathrm{d}V = \bar{S}_\phi\Delta V, \tag{2.50}$$

where ΔV is the volume of the control volume and $\bar{S}_\phi$ is the average value of S over that control volume. A second-order accurate approximation for the above equation can be obtained by using the midpoint rule, which replaces the average $\bar{S}_\phi$ by the cell centroid nodal value of the source function S_ϕ [45].

2.2.2.2 second-order upwind scheme

In this thesis we use a second-order finite difference upwind scheme to evaluate the values of the convective term at the faces of the grid cell. For a scalar field ϕ, the value at the face of a control volume V is [46]:

$$\phi_f = \phi + \nabla\phi \cdot \mathbf{r}, \tag{2.51}$$

where ϕ is the value at the cell center, and the gradient is evaluated in the upstream cell, $\mathbf{r}$ is the displacement vector from the upstream cell centroid to the face centroid, and the subscript f refers to face value. To use this formula, we need to evaluate the gradient within each cell, as discussed in the next section.

2.2.2.3 Least-squares cell-based gradient evaluation

In this thesis gradients are evaluated using least-squares cell-based scheme. If a scalar quantity ϕ varies linearly along a vector $\Delta\mathbf{r}_i$ connecting two cells $c0$ and ci, we have [47]:

$$(\nabla\phi)_{c0} \cdot \Delta\mathbf{r}_i = (\phi_{ci} - \phi_{c0}), \tag{2.52}$$

where $(\nabla\phi)_{c0}$ is the gradient at the cell center, $\Delta\mathbf{r}_i$ is the vector connecting the cell centroids, and ϕ_{c0} and ϕ_{ci} are the values of ϕ at the centroids of the cells $c0$ and ci. Figure 2.4 shows cell $c0$ surrounded by other cells, and illustrates the vector r_i connecting the cells' centroids.

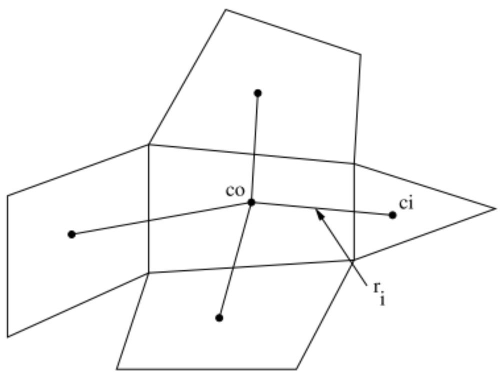

Figure 2.4: Generic cell surrounded by other cells and vectors connecting the cells' centroids. Reproduced with permission from [47].

Equations similar to (2.52) can be writting for each cell ci surrounding cell $c0$, generating a set of equations of the form [47]:

$$[J]\,(\nabla\phi)_{c0} = \Delta\phi, \tag{2.53}$$

where $[J]$ is the coefficients matrix, which is purely a function of grid geometry. The above system is an over-determined set of linear equations that can be solved by using a least-squares method [44]. The three components of the gradient vector are the unknowns, while the number of equations depends on the number of adjacent cells.

2.2.2.4 Assembly of the discretized equations

Using the discretization of the convective, diffusive and source terms introduced previously, the problem is reduced to a system of linear algebraic equations in the form [45]:

$$a_P \phi = \sum_{nb} a_{nb} \phi_{nb} + b, \tag{2.54}$$

where ϕ are the values of the scalar field at the cells centers, a are coefficients obtained from the discretization process, where the subscript P refers to the value at the node and nb refers to the neighboring cells. The last term b contains values resulting from discretizing the source term in equation (2.44) and also includes the terms arising from corrections due to the use of higher-order schemes. The numerical values of the coefficients a_P and a_{nb} depend on the method of discretization used and the mesh topology. Finally we have an equation similar to (2.54) for each cell of the mesh. The ensemble of the equations forms a set of algebraic linear equations with a sparse coefficient matrix. ANSYS Fluent solves this system of equations using a Gauss-Seidel linear equations solver with an algebraic multigrid method [47].

2.2.3 Temporal discretization

So far we have only considered the spatial discretization of equation (2.44), the next step would be derive its temporal discretization for time advancement. The time evolution of a scalar field ϕ is governed by the following generic equation [47]

$$\frac{\partial \phi}{\partial t} = F(\phi), \tag{2.55}$$

where $F(\phi)$ represents a generic flux. Note that all of conservation equations we consider can be rewritten in the form (2.55).

In this thesis we use the following second-order backward bounded finite difference scheme for temporal discretization [47]:

$$\frac{3\phi^{n+1} - 4\phi^{n} + \phi^{n-1}}{2\Delta t} = F(\phi), \tag{2.56}$$

where the superscript n refers to the current time instant, and Δt is the time step used to advance time. Thereofre, applying control volume CV discretization to the unsteady term of (2.44), we obtain [47]:

$$\iiint_{CV} \frac{\partial(\rho\phi)}{\partial t} \mathrm{d}V \cong \frac{\partial(\rho\phi)}{\partial t} V, \tag{2.57}$$

where V is the volume of the control volume CV and the time derivative is evaluated at the center of the cell using the formula (2.56).

2.2.4 Discretization of the governing equations

To discretize the governing equations, we need to discretize both time and space. We discretize time using the scheme (2.56), while in this section we provide the details for the spatial discretization. The steady state governing equations in the integral form are:

$$\begin{aligned} &\iint_S \mathbf{u} \cdot \mathbf{n} \, \mathrm{d}S = 0, \\ &\iint_S \mathbf{u} \otimes \mathbf{u} \cdot \mathbf{n} \, \mathrm{d}S = -\frac{1}{\rho} \iint_S p\mathbf{I} \cdot \mathbf{n} \, \mathrm{d}S + \frac{1}{\rho} \iint_S \boldsymbol{\tau} \cdot \mathbf{n} \, \mathrm{d}S, \end{aligned} \tag{2.58}$$

where $\boldsymbol{\tau}$ is the total stress tensor grouping both viscous and Reynolds stresses, and $\mathbf{I}$ is the identity tensor. Note that in the equations above the force term has been removed, as we don't have external forces acting on the fluid, in particular, gravity is negligible. In the subsequent sections we provide the methodology for disrectizing equations (2.58) by using finite volume method, and describe how they are solved by ANSYS Fluent.

2.2.4.1 Discretization the momentum equation

We discretize the momentum equation using a finite volume scheme. For each velocity component u_k, the corresponding discretized momentum equation obtained using (2.54) has the following expansion [47]:

$$a_P u_k = \sum_{nb} a_{nb} u_{knb} + \sum_{i}^{N_{faces}} p_f \Delta A_{ik} + S_{u_k}, \tag{2.59}$$

where ΔA_{ik} is the area of the ith-face of the cell multiplied by the kth-component of the unit vector normal to that face and S_{u_k} is the source term. Comparing this equation to (2.54), we note an additional source term, that results from the discretization of the pressure gradient term. Note that if the pressure field and mass fluxes are known, equation (2.59) can be solved as a linear system for the cell center values of the kth-velocity component. Note also that ANSYS Fluent uses a co-located arrangement for unstructured grids where both the pressure and the velocity components are stored at cell centers.

2.2.4.2 Pressure interpolation schemes

To solve equation (2.59) we need to know the pressure at the faces separating the cells, therefore a suitable interpolation schemes is needed. In this thesis, we use a second-order interpolation scheme for the pressure field. For each face of the cell, the pressure p_f is [47]:

$$p_f = p + \nabla p \cdot \mathbf{r}, \tag{2.60}$$

where p is the pressure at the cell center and $\mathbf{r}$ is the displacement vector from the cell centroid to the face centroid.

2.2.4.3 Discretization of continuity equation

In incompressible flows, the continuity equation imposes the solenoidality of the velocity field. The integral form of the continuity equation (2.58) can be discretized as follows [47]:

$$\sum_{i}^{N_{faces}} J_i \Delta A_i = 0, \tag{2.61}$$

where J_i is the mass flux across the ith-face:

$$J_i = \rho \mathbf{u}_f \cdot \mathbf{n}_i,$$

ρ is the fluid density, which is a constant in our case, and $\mathbf{u}_f \cdot \mathbf{n}_i$ is the velocity component normal to the ith-face center that should be evaluated. Linear interpolation of cell-centered velocities cannot be used, as it results in unphysical check-board pressure patterns. Instead of linear interpolation, ANSYS Fluent implements a weighted averaging scheme by using the coefficients a_P from equation (2.59). If we consider the cells $c0$ and ci in figure 2.4, the resulting mass flux J_i across the face between them is [47]:

$$J_i = \rho \frac{a_{P,c0} v_{n,c0} + a_{P,ci} v_{n,ci}}{a_{P,c0} + a_{P,ci}} + d_f((p_{c0} + (\nabla p)_{c0}) - (p_{ci} + (\nabla p)_{ci})), \tag{2.62}$$

where p_{c0}, p_{ci} and $v_{n,c0}, v_{n,ci}$ are, respectively, the pressures and normal velocities at the cells $c0$ and ci on either side of the face. Finally, d_f is a function of $\bar{a}_P$, which is the average of the coefficients a_P for the cells $c0$ and ci.

2.2.4.4 Pressure-velocity coupling

On the right-hand-side of the momentum equation (2.11) of the URANS formulation, it appears the pressure gradient and the Reynolds stress tensor as a source term. The Reynolds stress tensor is obtained by solving the equations for the turbulence model chosen, but a method to determine the pressure gradient is still needed. ANSYS Fluent uses equation (2.62) as an additional condition for the pressure field to derive a pressure-velocity coupling scheme.

Various pressure-velocity coupling methods have been developed over the years, and they are divided into two groups: pressure velocity segregated algorithms and pressure velocity coupled algorithms. Figure 2.5 shows the block diagram for the two different algorithms used to solve the pressure-velocity coupling. The pressure-velocity segregated algorithms assume an intial value for the pressure field and solves the discretized momentum equation using that pressure field. The pressure field is corrected using the continuity equation and is used again in solving the momentum equation. This process is iterated until a solution is reached. The coupled algorithms on the other hand solve simultaneously the momentum and the continuity equations. In this thesis we use a coupled solver algorithm implemented by ANSYS Fluent [47]. In the coupled algorithm, implicit coupling is achieved by implicit discretization of the pressure gradient term in the momentum equations. After introducing a suitable pressure interpolation scheme, the pressure term in the kth-component of the discretized momentum equation (2.59) becomes:

$$\sum_f p_f A_k = -\sum_j a^{u_k p} p_j, \tag{2.63}$$

where $a^{u_k p}$ are coefficients that depend on the chosen pressure interpolation scheme and the summations are carried over the cell's faces.

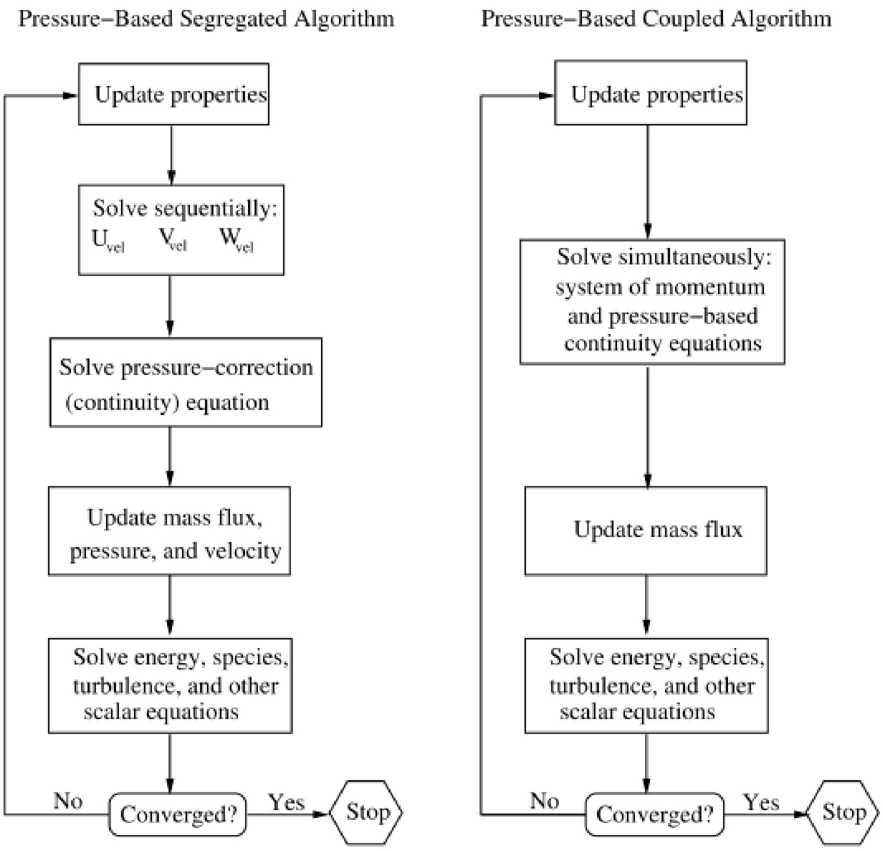

Figure 2.5: Algorithms used to solve pressure-velocity coupling. Reproduced with permission from [47].

Considering the kth-component of the discretized momentum equation, for any ith-cell a system of linear algebraic equations is obtained by replacing the pressure term with the expression above, as follows:

$$\sum_j {a_{ij}}^{u_k u_k} u_{kj} + \sum_j {a_{ij}}^{u_k p} p_j = b_{ik}^{u}. \tag{2.64}$$

If we use equation (2.62) for the mass flux and substitute it into the discretized continuity equation (2.61) we obtain:

$$\sum_k \sum_j {a_{ij}}^{p u_k} u_{kj} + \sum_j {a_{ij}}^{pp} p_j = {b_i}^{p}. \tag{2.65}$$

The overall system of equations obtained combining (2.64) and (2.65) is:

$$\sum_j [\mathbf{A}]_{ij} \mathbf{X}_j = \mathbf{B}_i, \tag{2.66}$$

where $[\mathbf{A}]_{ij}$ is the matrix of influence coefficients of cell i on cell j, $\mathbf{X}_j = [p_i u_i v_i w_i]^T$ is the vector of unkowns, and $\mathbf{B}_i$ is the residuals vector [47].

2.2.5 Boundary and initial conditions

To simulate correctly the flow past a wing, boundary conditions must be imposed both on the wing surface and in the far field. Thus, we construct a box-like domain big enough to simulate the far field. Figure 2.6 shows a schematic of the box-like domain, the location of the wing and the (far field) inlet velocity components. At the outlet a zero gauge pressure is imposed. At the wing surface no-penetration and the no-slip boundary conditions are imposed. Figure 2.6 shows a full DW for clarity, but in our simulations we impose symmetry with respect to the xz-plane passing through the wing middle chord, and use only half of the domain shown to reduce the computational cost. If the inlet velocity has a sideslip angle, the sides of the domain will represent inlets or outlets, depending on the flow direction. If the inlet velocity had no sideslip angle, the sides can be selected to be either inlets or outlets.

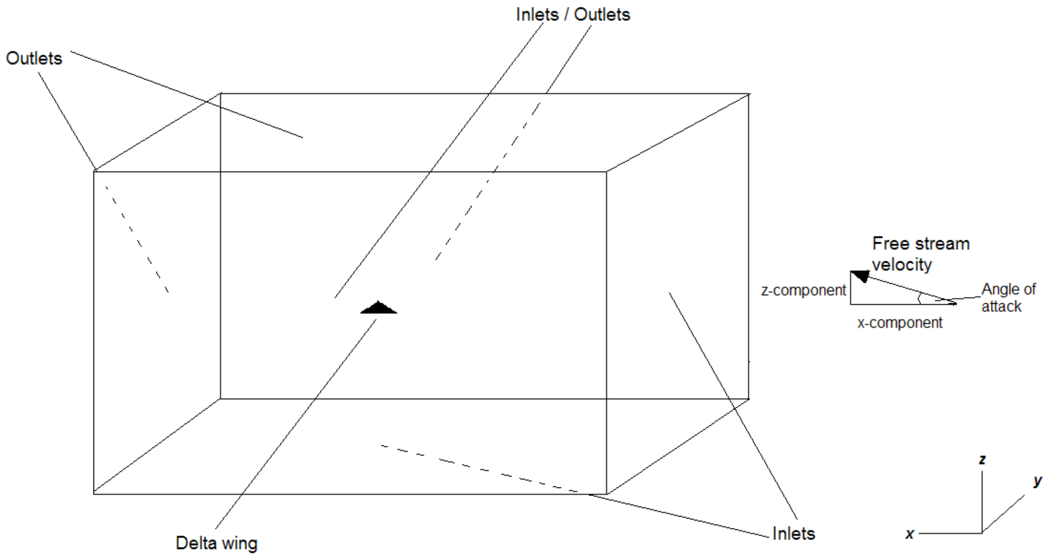

Figure 2.6: Isometric view of the fluid domain enclosing the delta wing

The velocity components that we impose at the inlet boundaries, are:

$$\begin{aligned} u &= U_\infty \cos(\alpha), \\ v &= 0, \\ w &= U_\infty \sin(\alpha), \end{aligned} \tag{2.67}$$

where U_∞ is the free stream velocity and α is the angle of attack of the DW. Note that the y-component of the free stream velocity is zero because we impose symmetry. Therefore, we cannot consider flows with a sideslip.

At the inlet and outlet we also need to impose the boundary conditions for the turbulence model in terms of turbulent viscosity ratio ν_t/ν and turbulence intensity. Values for the turbulent viscosity ratio boundary condition in the free stream can be found in literature (see for example [36]), and the appropriate for our simulations is a value of 0.1. We use a value of 0.05% for the turbulence intensity, which corresponds to low turbulence intensity in the free stream, a common choice in aeronautical applications. The turbulence model needs boundary conditions at the DW walls, and they are imposed automatically by ANSYS Fluent using pre-defined functions.

Since the flows past DW and RDW are unsteady, initial conditions are also needed. If the initial conditions for the whole flowfield are not known as in our case, we can set initial "guess" values in ANSYS Fluent and selecting the values assigned at the inlet boundary, ANSYS Fluent will then assign the inlet values to every cell in the domain excluding the cells that lie on another boundary. In this way, an initial flowfield is obtained by ANSYS Fluent.

2.2.6 Summary of numerical solution procedure

We can summarize the numerical solution procedure use to simulate a flow over a DW or RDW as follows:

1. Discretize the domain into a number of finite volumes.
2. Apply boundary conditions and initialize the flowfield.
3. Advance in time.
4. Solve the discretized momentum and continuity equations.
5. Update the mass flux.
6. In the boundary layer region solve the discretized k and ω equations, else solve the discretized LES formulation.
7. Check convergence.
8. If it is converged go to step 3. If it is not converged iterate steps 4 to 7 until convergence is achieved.

2.2.7 Simulation setup in ANSYS Fluent

In this subsection we discuss how to setup ANSYS Fluent to simulate a flow past a DW or RDW. First we select the fluid used, which is air at constant density $\rho = 1.225$ kg/m^3 and constant dynamic viscosity $\mu = 1.789 \times 10^{-5}$ Pa.s. Second we select the turbulence model, a delayed DES in combination with the kω-SST model with curvature correction as a RANS model. We used default values of the turbulence model set by Fluent. Finally, since we are solving a problem where the compressibility effects are negligible, we chose a pressure based solver and a coupled algorithm for the pressure-velocity coupling.

In details, the solver performs that gradients evaluation using a least-squares cell based method and the pressure interpolation is a second-order scheme. It uses a second-order upwind scheme for the convective terms of the momentum, turbulent kinetic energy k and specific dissipation rate ω equations. Time integration is performed using a bounded second-order implicit scheme.

To evaluate the force coefficients and the non-dimensional quantities, such as force coefficients, ANSYS Fluent needs a series of characteristic (reference) values. In the far field we assume the air density $\rho_\infty = 1.225$ kg/m^3 ,the dynamic viscosity $\mu = 1.789 \times 10^{-5}$ Pa.s, the free stream velocity $U_\infty = 11.83$ m/s and the pressure $p_\infty = 101325$ Pa, which corresponds to sea level value. The reference area $S_{ref} = 0.0411$ m^2 is half the wing planform area, because we are assuming symmetry and only performing the simulations over a half wing. And the characteristic length c the wing mid chord length, is 0.42 m. Therefore, the Reynolds number of our simulation is $Re_\infty = 3.4 \times 10^5$.

2.3 Grid and time step selection

In order to choose the best mesh and most appropriate time step for our simulations, we use a method proposed by Cummings *et al.* (2008) [28]. They suggested to construct three meshes with different sizes, coarse, medium and fine, and select six different time steps one double of the other. The two smallest time steps are used with the fine grid, the two middle steps with the medium grid, and the two largest steps with the coarser grid. To select the best combination of gird and time step, six simulations of the flow past a DW at angle of attack $\alpha = 20°$ are performed using the three grids and the associated time steps. A spectral analysis of the unsteady aerodynamic forces is performed to detect the variations of the primary and secondary frequencies, associated with vortex breakdown, with grid size and time step. The appropriate combination of grid and time step is the one for which the primary and secondary frequencies do not change when further reducing the time step or a using a finer grid.

2.3.1 Grid construction

The geometry of the DW (or RDW) considered in this thesis is exactly the same geometry of the DW used by Ko (2016) [1] because we want to compare the results of our simulations with Ko's experimental findings. Figure 2.7 shows the geometry of the DW (or RDW), considered slender, has a chord of $c = 0.42$ m, a sweep angle of 65°. The three sides of the DW (or RDW) are beveled at 15° and the thickness is 0.63 cm. We constructed the grids around such wing using ANSYS Meshing software.

2.3.1.1 Grid in the boundary layer region

When constructing a gird, one of the most important points to take into account is correctly resolving the flow in the boundary layer regions. The mean velocity profile of a turbulent boundary layer is given by the law of the wall, which is considered to universal. The distance from the wall in a turbulent boundary layer is defined in terms of the normalized wall distance y^+:

$$y^+ = \frac{\nu}{u_\tau}, \tag{2.68}$$

where u_τ is the friction velocity:

$$u_\tau = \sqrt{\frac{\tau_w}{\rho}},$$

where τ_w is the shear stress at the wall [36].

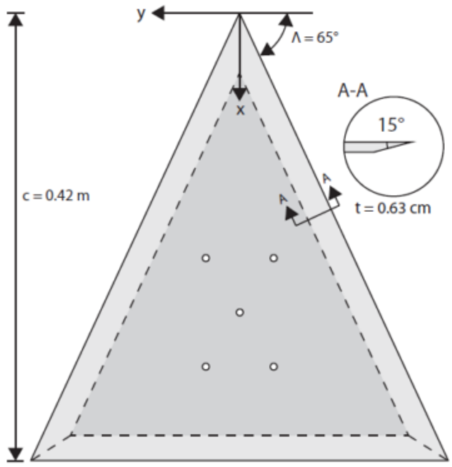

Figure 2.7: Geometry for the slender delta wing considered for analysis. Reproduced with permission from [1].

A turbulent boundary layer is conceptually divded into various regions according to their distance from the wall. The region closer to the wall is known as the viscous layer, which ends at approximately $y^+ = 5$. To resolve accurately a turbulent boundry layer, at least 2 grid points should lie in the viscous layer [28] in order to effectively utilize the RANS model (kω SST).

To construct a mesh to resolve accurately a turbulent boundary layer, the height of the first cell near the wall can be calculated using the empirical formula [28]:

$$\Delta_{turb} = c\frac{(13.1463 y^+_{ave})^{0.875}}{{Re_\infty}^{0.9}}, \tag{2.69}$$

where y^+_{ave} is the average value of the y^+, chosen to be 1. Using the equation above we obtained a first cell height of 0.042 mm.

To generate an appropriate grid for the boundary layer region, we created a subdomain wrapped around the DW. The thickness of this subdomain was chosen equal to the thickness of the turbulent boundary layer over a flat plate, such thickness is given by the following approximation [9]:

$$\delta_t = \frac{0.37c}{Re^{1/5}}, \tag{2.70}$$

that in our case is 1.2 cm. To discretize the boundary layer region we used 20 grid points, with a growth rate of 1.2 starting from the smallest grid cell at the wall. The cells we used were both prisms and hexahedrals.

2.3.1.2 Grid outside the boundary layer region

To generate an appropriate grid for the fluid domain surrounding the wing and the grid in the boundary layer region, we selected a box-like domain large enough to simulate flight in a free-stream, so that the presence of the boundaries of the box-like domain does not affect the flowfield over the wing and vice versa. We selected the inlet and outlet of the box-like domain such that inflows at different angles of attack can be simulated and defined the plane $y = 0$ as a symmetry plane. The distance from the leading edge of the DW to the inlet and from the trailing edge to the outlet is 20 times the wing chord c, while the upper, lower and side boundaries of the domain are at a distance 10 times the chord length from the wing. Note that the domain has been conceived to be used for both DW and RDW, in the latter case the domain is turned by 180° about the vertical axis (z-axis) and the inlets and outlets switch roles.

We generated three different grids, coarse, medium and fine, in order to perform the sensitivity study suggested by Cummings *et al.* [28]. Note that the grid in boundary layer region is kept identical for all three grids, while the grid density changes outside the boundary layer region.

Table 2.2 reports the sizing and the quality parameters for each of the three grids. By defining a certain relevance center, ANSYS meshing software generates automatically unstructured grids of different sizes. Bad quality cells are those who have high skewness (close to 1), or an aspect ratio much larger than one. The number of bad cells in the grids generated is negligible compared to the total number of cells. Furthermore, due to the use of unstructured mesh and the complex geometry of the wing, the values reported in table 2.2 can be considered acceptable and within the limits suggested by ANSYS Fluent. Figure 2.8 shows the gridded fluid domain and the inlets and outlets, while figure 2.9 shows details of the grid around the DW.

Table 2.2: Mesh sizes and quality

Mesh	**Mesh size**			**Quality**		
	Relevance center	Growth rate	No. of cells	Max aspect ratio	Max skewness	Orthogonal quality
Coarse	Medium	1.2	3465493	252.09	0.978	2.21e-2
Medium	Fine	1.2	6143440	265.02	0.975	3.46e-2
Fine	Fine	1.07	8653808	237.56	0.975	3.46e-2

2.3.2 Time step selection

A correct time step selection is essential step for simulating accurately unsteady flows that include regions of separated flows with vorticity fluctuations. As a rule of thumb, for selecting an appropriate time step, Cummings *et al.* [28] suggested to use a non-dimensional time step $\Delta t^\star = 0.01$, where:

$$\Delta t^\star = \frac{\Delta t U_\infty}{c}, \tag{2.71}$$

Δt is the dimensional time step in seconds, U_∞ is the free-stream, or characteristic, velocity and c is the wing mid chord, characteristic length. To perform a grid and time step sensitivity study using the method suggested by Cummings *et al.* [28], we select the non-dimensional time step $\Delta t^\star = 0.01$ to be the minimum one. Therefore, the six time steps to be used in the sensitivity study are $\Delta t^\star = 0.01, 0.02, 0.04, 0.08, 0.16, 0.32$.

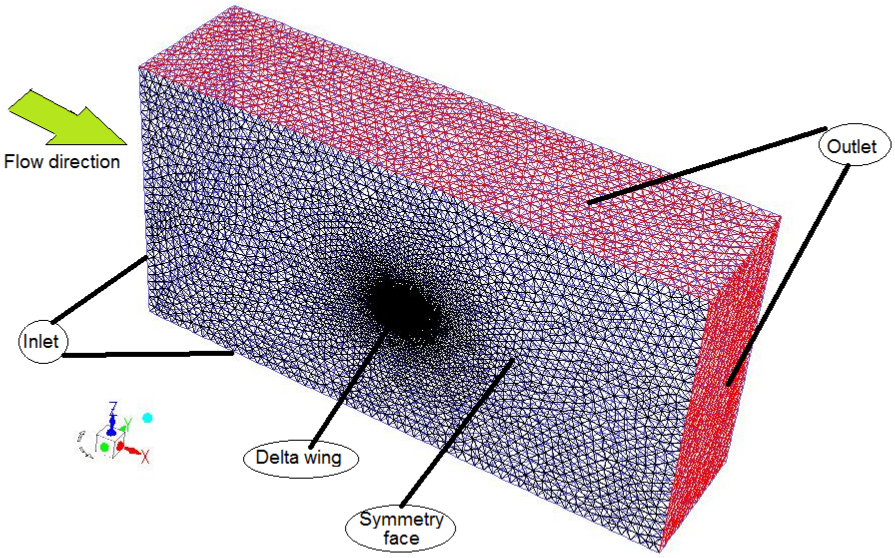

Figure 2.8: Isometric view for the gridded fluid domain for the half DW

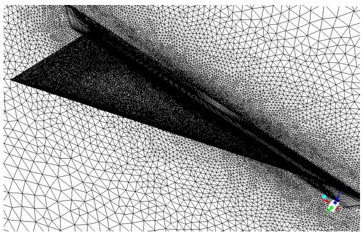

(a)

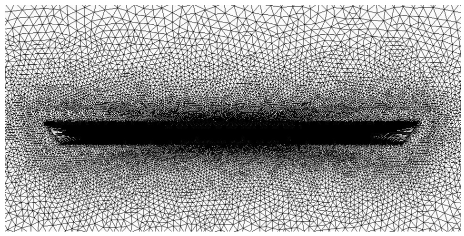

(b)

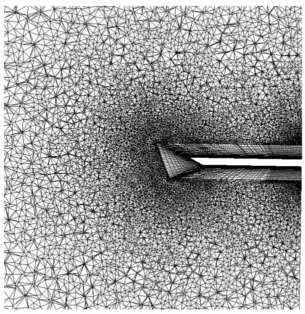

(c)

Figure 2.9: Details of the grid around the DW: (a) isometric view, (b) side view, (c) cross section located at $x/c = 0.5$

2.3.3 Time step selection

A correct time step selection is essential step for simulating accurately unsteady flows that include regions of separated flows with vorticity fluctuations. As a rule of thumb, for selecting an appropriate time step, Cummings *et al.* [28] suggested to use a non-dimensional time step $\Delta t^{\star} = 0.01$, where:

$$\Delta t^{\star} = \frac{\Delta t U_{\infty}}{c}, \tag{2.72}$$

Δt is the dimensional time step in seconds, U_{∞} is the free-stream, or characteristic, velocity and c is the wing mid chord, characteristic length. To perform a grid and time step sensitivity study using the method suggested by Cummings *et al.* [28], we select the non-dimensional time step $\Delta t^{\star} = 0.01$ to be the minimum one. Therefore, the six time steps to be used in the sensitivity study are $\Delta t^{\star} = 0.01, 0.02, 0.04, 0.08, 0.16, 0.32$.

2.3.4 Gird and time step sensitivity study

Using the method suggested by Cummings *et al.* [28], we now perform a grid and time step sensitivity study in order to select the most appropriate combination of grid and time step. To this end, we perform computations of the flow past a DW at an angle of attack $\alpha = 20°$ and Reynolds number $Re_{\infty} = 3.4 \times 10^5$. Under these conditions the flow over the DW is unsteady, because the leading edge vortices undergo to vortex breakdown and vortices are shed at the trailing edge of the DW. These phenomena are characterized by well-defined frequencies [18]. We use a MATLAB script to evaluate the power spectral density (PSD) of the time history of the lift coefficient C_L in terms of the Strouhal number:

$$St = \frac{fc}{U_{\infty}}, \tag{2.73}$$

where f is the frequency in Hz. Note that a spectrum as a function of the wave number is obtained by replotting the original spectrum in terms of the inverse of Strouhal number ($1/St$).

To obtain a well-defined spectrum, the unsteady simulations must run up to 3.5 seconds of flow time, to overcome the initial transient. Within each time step, five internal sub-iterations are used as suggested by Cummings *et al.* [28] because there is no improvement in convergence when using a higher number of sub-iterations. Table 2.3 summarizes the six pairs of grid and time step created to perform the sensitivity study.

Table 2.3: Time step values and corresponding grid

$\Delta t^{\star}$	0.32	0.16	0.08	0.04	0.02	0.01
Grid	Coarse	Coarse	Medium	Medium	Fine	Fine
Δt (s)	0.012	0.006	0.003	0.0015	0.00075	0.000375

2.3.4.1 Results of sensitivity study

In this subsection, we present the results of the grid/time step sensitivity study obtained by running six simulations using the pairs of grid/time step summarized in table 2.3. All simulations compute the same flow past a DW at an angle of attack $\alpha = 20°$ and Reynolds number $Re_\infty = 3.4 \times 10^5$.

Figure 2.10 presents the contours of the x-component of vorticity on a plane perpendicular to the DW located as 70% of the wing chord length. Each panel shows the contours of the primary and secondary leading edge vortices obtained by using different grids. As the mesh becomes finer, moving from panel 2.10(a) to panel 2.10(c), more details about the vortical structures are discernible. Figure 2.10(a) shows the results obtained by using the coarse grid, the vortex core cannot be well identified and the secondary vortex is not resolved. In figure 2.10(b), the vortex core can be identified along with the core of the secondary vortex. However, only by using the fine grid, see figure 2.10(c), the vortex cores for both the primary and secondary vortices are well defined.

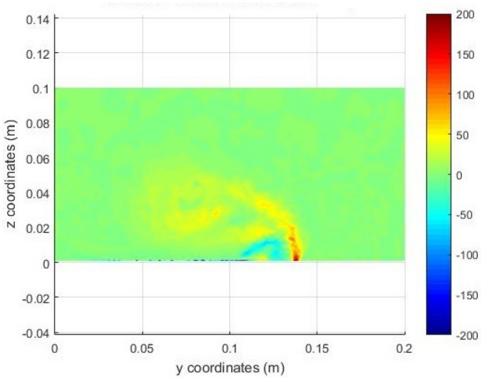

(a) Coarse grid using $\Delta t = 0.012$

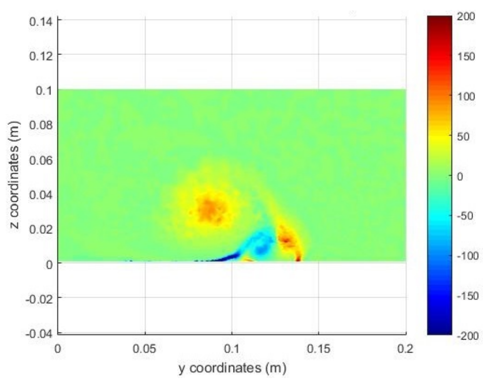

(b) Medium grid using $\Delta t = 0.0015$

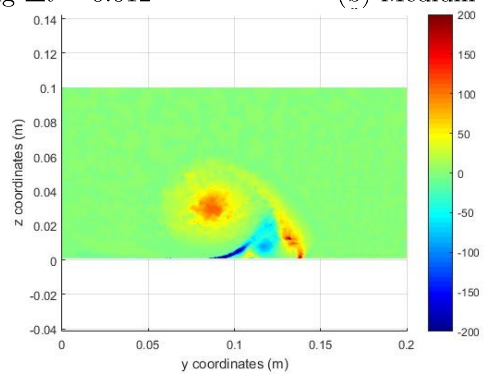

(c) Fine grid using $\Delta t = 0.00075$

Figure 2.10: Contours maps of the x-component of the vorticity field plotted on a yz-plane, perpendicular to the DW, located at 70% if the wing chord length. Panels (a)-(c) show the effect of grid refinement on the resolution of the primary and secondary vortices

Figure 2.11 shows the time histories and power spectral densities (PSD) of the lift coefficient C_L obtained performing two unsteady simulations using the coarse grid and time steps $\Delta t = 0.012$ and 0.006 seconds, respectively. The plots of the power spectral densities show that the locations of the primary frequency peak are almost unaffected by the change in the time step, which indicates the limitations of the coarse grid in detecting the correct dynamics of the vortical structures over a DW (as seen in figure 2.10)). Even though the peak of the primary frequency did not change when reducing the time step, we cannot stop the sensitivity study at this stage because the selection of the grid and time step cannot be decided by testing one grid only, and therefore, finer grids should be tested.

Figure 2.12 shows the time histories and PSDs for the lift coefficient C_L obtained by performing simulations using the medium grid and a time step $\Delta t = 0.0015$ seconds and the fine grid and a time step $\Delta t = 0.00075$ seconds. We see from the figure that as the grid becomes finer and a smaller time step is used, the resolution of the spectra is enhanced and more dynamics are captured. Note that for the medium grid the locations of the primary and secondary peaks change when using a smaller time step, which indicates that using a finer grid will allow to detect even more unsteady dynamics. Using the fine grid, the results showed smaller variations in the location of the primary peak than with the medium grid. However, when the time step used with the fine grid is reduced, the peak location remains almost unchanged for the primary frequency, and only slightly changed for the secondary frequency.

The location of the peak of the primary frequency corresponds to a wave number value close to 4, i.e. a Strouhal number value of 0.25, which, according to [18], is associated to the vortex shedding at a DW trailing edge. Note that this peak corresponds to the phenomenon that has a dominant effect on the coefficient C_L. Figure 2.12 also shows that there are multiple small peaks at lower wave number values, i.e. higher St, which represent the faster dynamics of unsteady phenomena such as helical mode and Kelvin-Helmholtz instabilities shown in figures 1.9 and 1.10.

Figure 2.13 summarizes the results of our grid and time step sensitivity study. Note that the primary and secondary frequencies peaks locations change as the time step reduces and the grid becomes finer, until an almost steady value is obtained. In particular, changing the time step from 0.00075 s to 0.000375 s when using the fine grid produces only slight changes in the locations of the primary and secondary frequencies peaks. Therefore, time steps smaller than 0.00075 seconds are unnecessary. In conclusion we will use the fine grid with time step 0.00075 s for the simulations and subsequent analysis of the flow over a DW and a RDW.

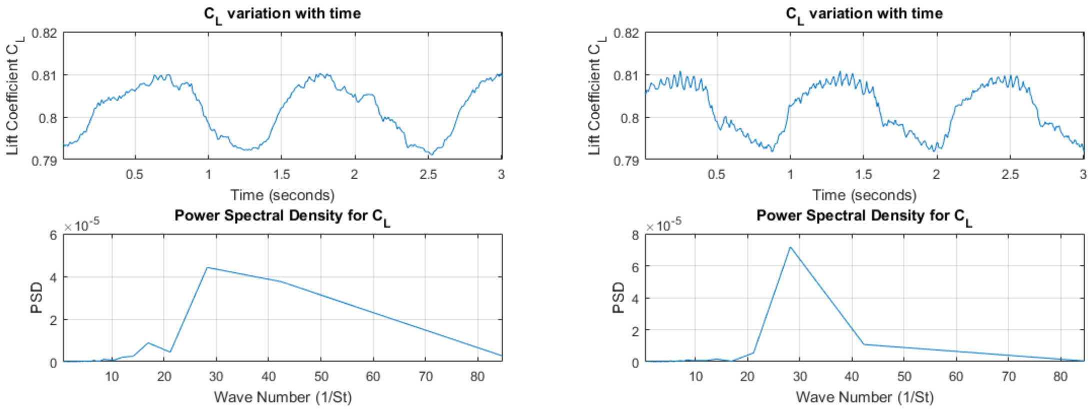

(a) Δt=0.012 s (b) Δt=0.006 s

Figure 2.11: Time history and power spectral density for the lift coefficient C_L of the delta wing at $\alpha = 20°$ from simulation using the coarse grid

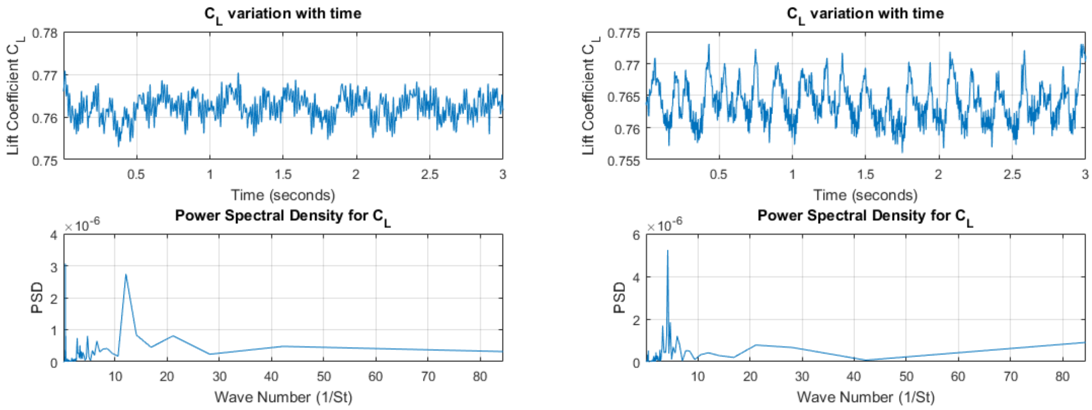

(a) Medium mesh Δt=0.0015 s (b) Fine mesh Δt=0.00075 s

Figure 2.12: Time history and power spectral density for the lift coefficient C_L of the delta wing at $\alpha = 20°$ from simulations using the medium and fine grids

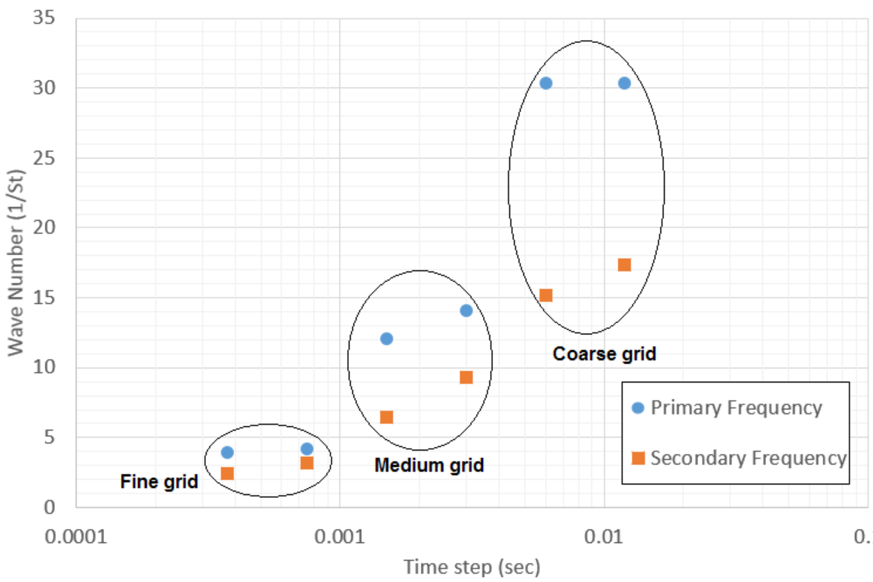

Figure 2.13: Primary and secondary wave numbers variation with time step and grid size, time steps used with the coarse grid are $\Delta t = 0.012$ s and $\Delta t = 0.006$ s, time steps used with the medium grid are $\Delta t = 0.003$ s and $\Delta t = 0.0015$ s, time steps used with the fine grid are $\Delta t = 0.00075$ s and $\Delta t = 0.000375$ s.

Chapter 3

Results of the Numerical Simulations

In this chapter, we present and analyze the results of the CFD simulations of the flow past a DW and a RDW having the same planform. The results include force coefficients, flow visualizations in the form a iso-surfaces and contours maps, and vortex characteristics. First we discuss the results of the DW and second the results of the less studied RDW. In particular, for the RDW, we focus on the unsteady flow. We analyze the time history of the force coefficients to understand the physics of the unsteady phenomena characteristic of the flow past a RDW. Finally, we compare the performance of the two wings.

For convenience, we recall that the setup of the numerical simulations for both DW and RDW is the same. The reason for selecting the same conditions for both wings is to compare their performance. We use a fine mesh, with about 8 million cells, and a time step $\Delta t = 0.00075$ seconds. The machine used for performing the numerical simulations has a processor Intel(R) Xeon Phi(TM) 1.30GHz, with 64 physical cores and four threads for each core, the total RAM is 112 Gigabytes. We performed the numerical simulations using 50 logical cores.

3.1 Results for a delta wing

In this section, we present the results obtained simulating the flow past a DW at angles of attack ranging from $\alpha = 5°$ to $20°$. We do not consider angles of attack larger than $\alpha = 20°$ because, in these cases, the leading edge vortex breaks down in the middle of the wing creating a stall condition, which is beyond the purpose of this study.

3.1.1 Flow visualizations

Figure 3.1 shows the iso-surface of the vorticity magnitude equal to 200, colored in proportion to the value of the pressure coefficient C_p, on the leedward side of a DW at angles of attack $\alpha = 5°, 10°, 15°$ and $20°$. Recall that the numerical simulations are performed only on one half of the DW because we impose symmetry with respect to the plane $y = 0$. The leading edge vortex, or primary vortex, and the shear layer separating from the leading edges dominate the flow. Note that as the angle of attack increases from panel (a) to (d), the size of the primary vortex increases producing a stronger suction shown by the color of the primary vortex, yellow/green at low angles of attack, $\alpha = 5°$ and $10°$, and green/cyan at higher angles of attack, $\alpha = 15°$ and $20°$. The vorticity produced by the separating shear layer over the leeward side of the DW leaves the trailing edge and creates a wake as shown in figures 1.4 and 1.5. However, the details of the vortical structures in the wake of the DW are not captured beyond half a chord past the trailing edge, because the grid is not sufficiently refined and the vorticity magnitude value in the far wake is weak. At angles of attack $5°$ to $15°$, panels (a) to (c), the vortex core is coherent up and past the trailing edge of the DW, while at angle of attack $20°$, the vortex core undergoes to a spiral vortex breakdown near the trailing edge of the DW, similar to the one illustrated in figure 1.3. Figure 3.2 presents the instantaneous snapshot of the iso-surface (in blue) of the vorticity magnitude equal to 1000 that visualizes the cores of the primary vortices showin in figure 3.1(d). Figure 3.2 shows that the cores of the primary vortices undergo to a spiral vortex breakdown (in green) near the trailing edge of the DW at angle of attack $\alpha = 20°$. Panel (a) shows a three-dimensional view, while a magnified view of the spiral breakdown is shown in panel (b). Right before the helical motion of the core of the leading edge vortex, there is an increase in the pressure within vortex core accompanied by a slight increase in its size.

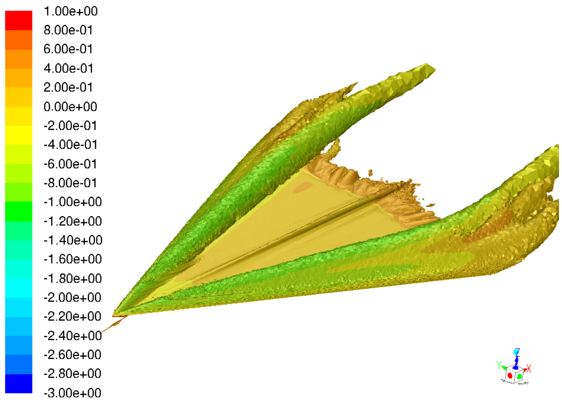

(a) $\alpha = 5°$

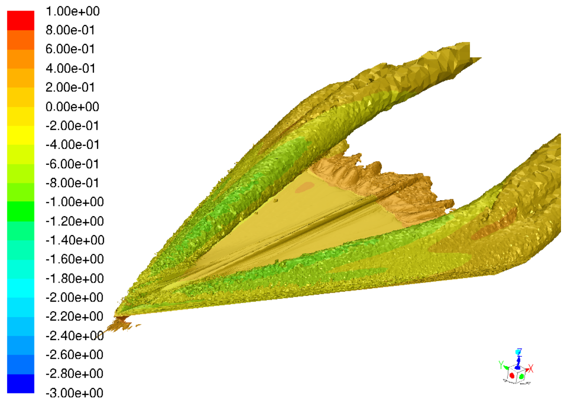

(b) $\alpha = 10°$

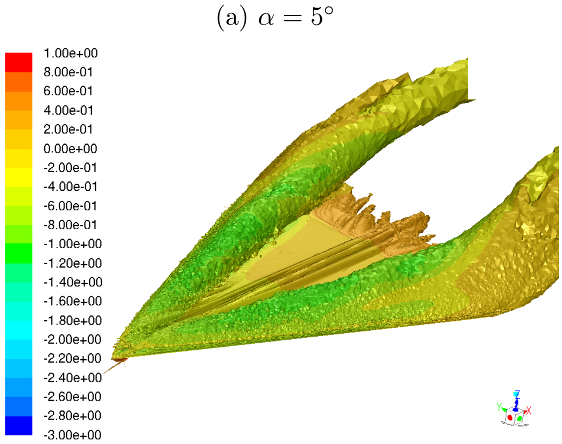

(c) $\alpha = 15°$

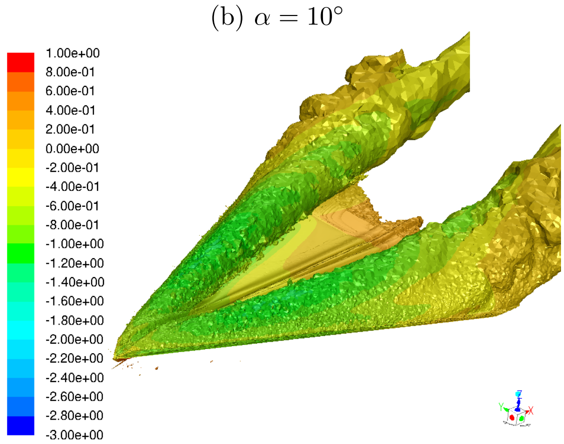

(d) $\alpha = 20°$

Figure 3.1: Iso-surface of vorticity magnitude equal to 200 colored in proportion to the pressure coefficient C_p on the leeward side of a DW at angles of attack $\alpha = 5°, 10°, 15°$ and $20°$.

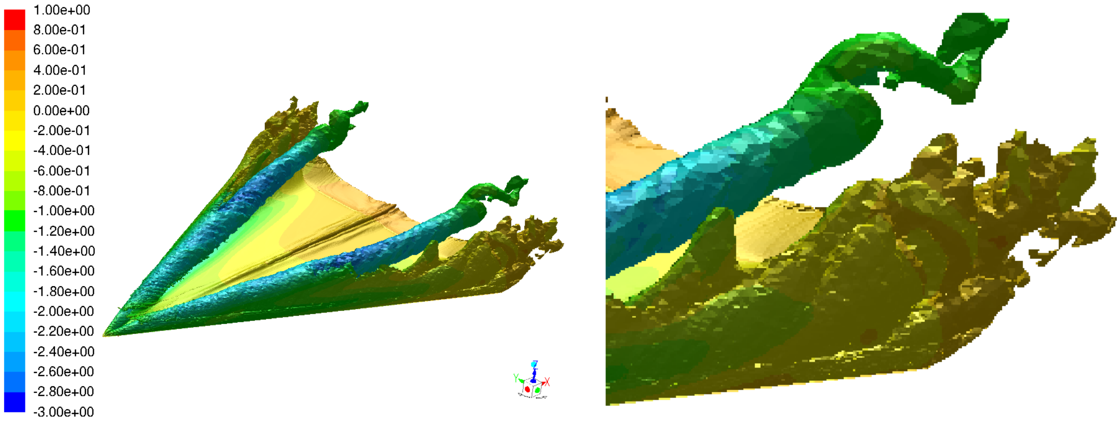

(a) Three-dimensional view

(b) Magnified view

Figure 3.2: Iso-surface of vorticity magnitude equal to 1000 colored in proportion to the pressure coefficient C_p showing spiral breakdown of the primary vortex core of a DW at angle of attack $\alpha = 20°$.

Figure 3.3 shows the contour maps of the pressure coefficient C_p over the leeward surface of the DW at angles of attack $\alpha = 5°, 10°, 15°$ and $20°$. In all cases, underneath the primary vortex there is a low-pressure region that extends downstream, where the free stream pressure is recovered. The peak suction is located close to the apex of the DW. As the angle of attack increases, higher suction is produced by the primary vortex over the leeward side of the wing and the width of the suction region increases as the size and strength of the primary vortex increases, as shown in figure 3.1, leading to an increase in lift. In all cases, the pressure distribution over the leeward side of the DW creates adverse pressure gradients in multiple directions as shown in figure 3.4. Note that the extension and intensity of the adverse pressure gradient region in the axial direction increase as the angle of attack increases, and contribute to the breakdown of the DW primary vortex [48]. The adverse pressure gradient in the outboard direction leads to flow separation and formation of the secondary vortex [49]. The very thin region of suction, adjacent to the main suction region of the primary vortex, is due to the secondary vortex. In the central part of the wing, around the plane of symmetry, the pressure is almost uniform with a small variation in the chordwise direction.

Figure 3.5 shows the contour lines of the skin friction coefficient C_f, drawn on the leeward side of the DW at angles of attack $\alpha = 5°, 10°, 15°$ and $20°$. At angles of attack $5°$ to $15°$, panels (a) to (c), moving from the wing central part towards to leading edge, we observe two lines of zero skin friction corresponding to two stagnation lines. These lines extend from the wing leading edge to the trailing edge. These lines are due to the primary and secondary vortices and correspond to lines of separation and reattachment of the flow. The stagnation lines separate regions of flow with different behavior, in the central part of the DW, the flow is streamwise, while between the stagnation lines there is a cross flow (inboard or outboard) induced by the primary and secondary vortices (see figure 1.2). As the angle of attack increases, from panel (a) to panel (d), the distance separating the two lines increases due to the size of the primary vortex. Note that, at $\alpha = 20°$ (panel (d)) the stagnation lines are lost near the trailing edge because of the breakdown of the primary vortex [50].

To visualize the flowfield, we inject at each time step about 2500 massless particles into the flow to act as tracers. The particles are injected from a line parallel to the leading edge of the DW, 1 mm away from it and long as the leading edge. Figure 3.6 shows an instantaneous snapshots of the massless particles convected by the flow past a DW at angle of attack $\alpha = 14°$. The particles are colored in proportion to the particle residence time, i.e. the time elapsed since a particle was injected into the flow. The (blue) particles that visualize the shear layer separating from the leading edge are entrapped (light blue) within the primary vortex core, making it visible. Figure 3.1 and 3.6 present two different visualizations of the core of the primary vortex. The particles injected close to the trailing edge, apparently, are entrapped only by the secondary vortex. Both the cores of the primary and secondary vortices can be seen extending downstream beyond the DW trailing edge, similarly to figures 1.4 and 1.5.

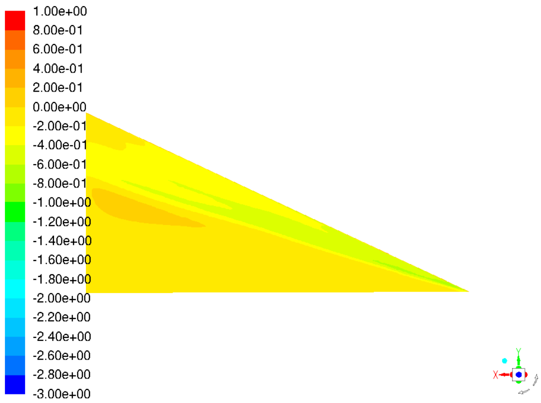

(a) $\alpha = 5°$

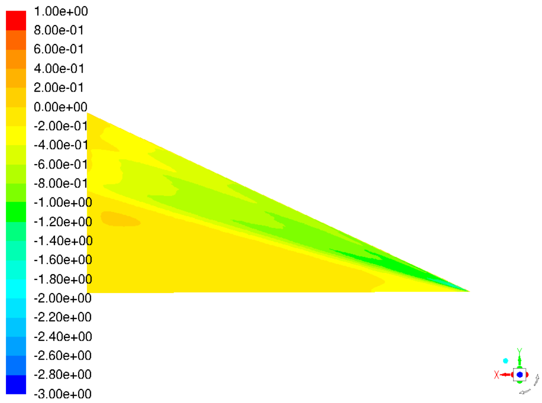

(b) $\alpha = 10°$

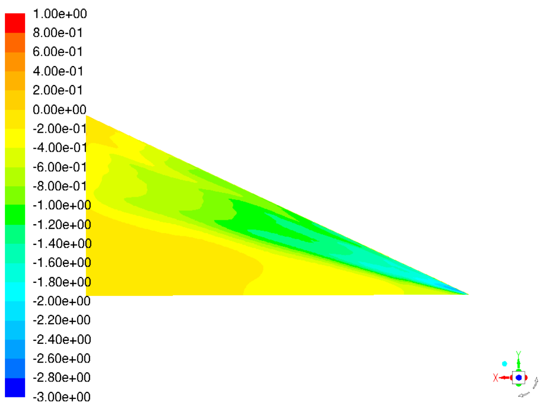

(c) $\alpha = 15°$

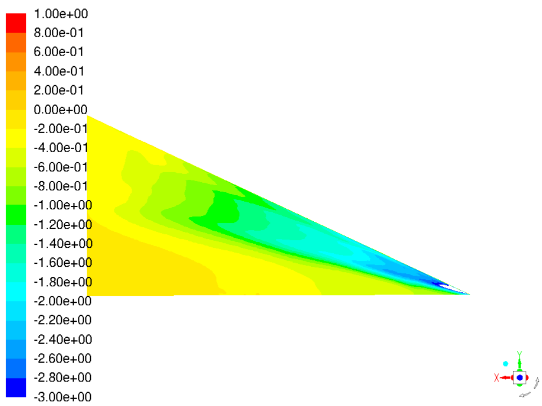

(d) $\alpha = 20°$

Figure 3.3: Instantaneous distribution of pressure coefficient C_p over the leeward side of the DW at angles of attack $\alpha = 5°, 10°, 15°$ and $20°$.

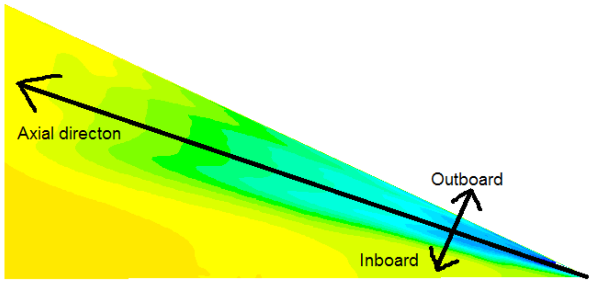

Figure 3.4: Directions of adverse pressure gradient on the leeward surface of a DW, shown contours of pressure coefficient C_p over the leeward surface of a DW at angle of attack $\alpha = 20°$.

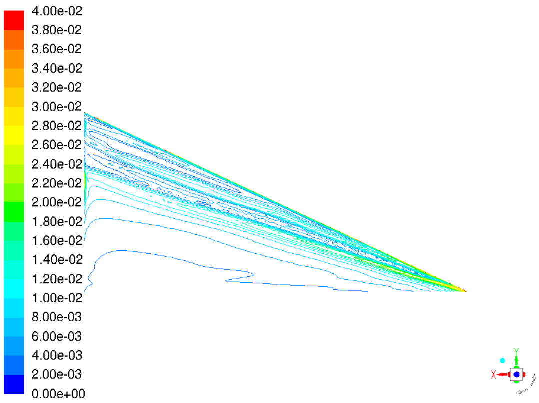

(a) $\alpha = 5°$

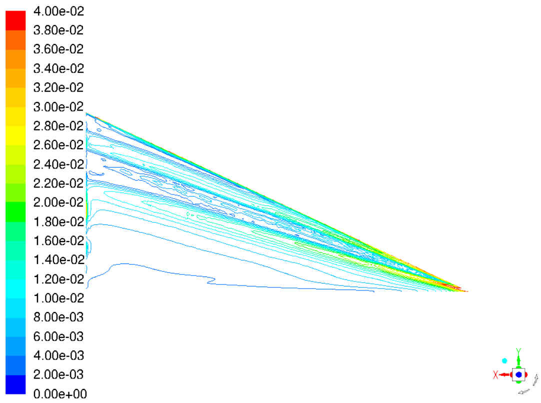

(b) $\alpha = 10°$

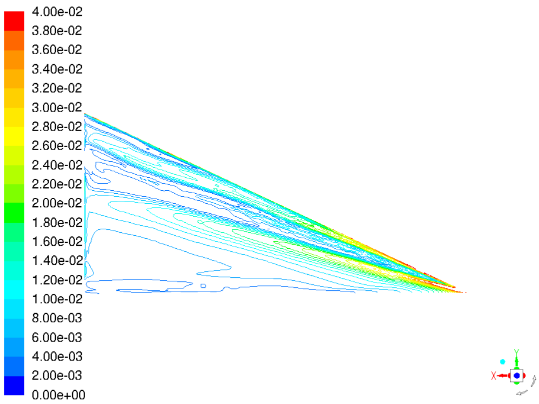

(c) $\alpha = 15°$

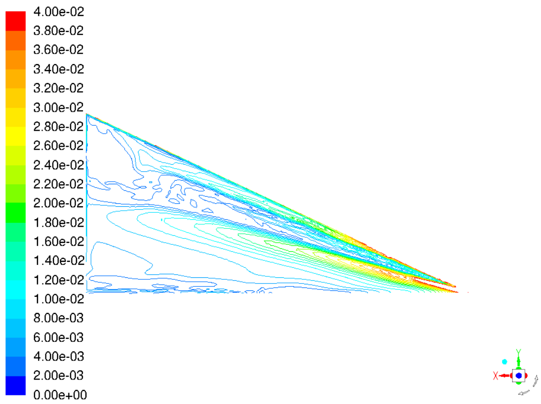

(d) $\alpha = 20°$

Figure 3.5: Contour lines of the skin friction coefficient C_f over the leeward side of the DW at angles of attack $\alpha = 5°, 10°, 15°$ and $20°$.

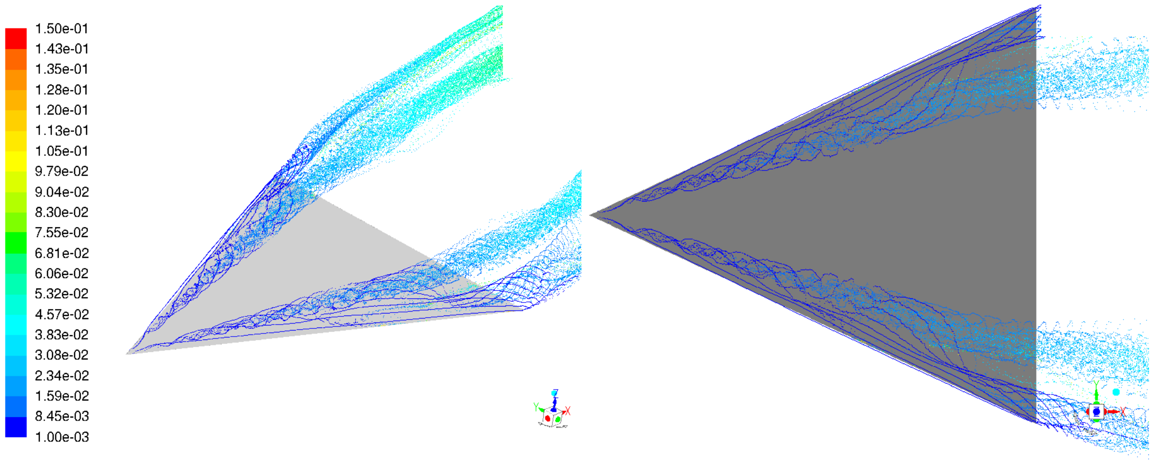

(a) Three-dimensional view

(b) Top view

Figure 3.6: Instantaneous snapshot of the particles injected in the flow past a DW at an angle of attack $\alpha = 14°$ from a line 1 mm away and parallel to the DW leading edge. The particles are colored in proportion to the particle residence time.

3.1.2 Characteristics of the leading edge vortex

The vorticity of the leading edge vortex is mainly composed by the x-component of the vorticity, which is defined as:

$$\zeta = \frac{\partial w}{\partial y} - \frac{\partial v}{\partial z}. \tag{3.1}$$

The associated normalized vorticity is $\zeta c/U_\infty$. The circulation Γ of the leading edge vortex at a given x/c location is obtained by integrating the x-component of the vorticity over the area, S, occupied by the vortex:

$$\Gamma = \oint_S \zeta \, \mathrm{d}S. \tag{3.2}$$

The associated normalized circulation is $\Gamma/U_\infty c$. If we discretize the area of the cross section of the leading edge vortex on a yz-plane in elements of area ΔS_i, the circulation of the vortex can be approximated as:

$$\Gamma = \sum_i^N \zeta_i \Delta S_i, \tag{3.3}$$

where N is the number of elements ΔS_i and ζ_i is the mean value of the vorticity component ζ within ΔS_i.

To use equation (3.3), it is necessary to identify the area occupied by the cross section of the vortex. To this end, we first detected the location of the center of the core by detecting the location where the maximum of the x-component of the vorticity matches the minimum of the fluid velocity on the yz-plane. We estimate the size of the primary vortex by computing the tangential velocity induced by the vortex along a line passing through the center of the vortex, and assuming the distance between the two points of maximum tangential velocity to be the diameter of the primary vortex. Figure 3.7 shows the normalized tangential velocity distributions along a horizontal line passing through the center of the primary vortex at various chordwise stations for a DW at angle of attack $\alpha = 20°$. Note that the maximum tangential velocity decreases and the size of the primary vortex increases as the chordwise station moves downstream.

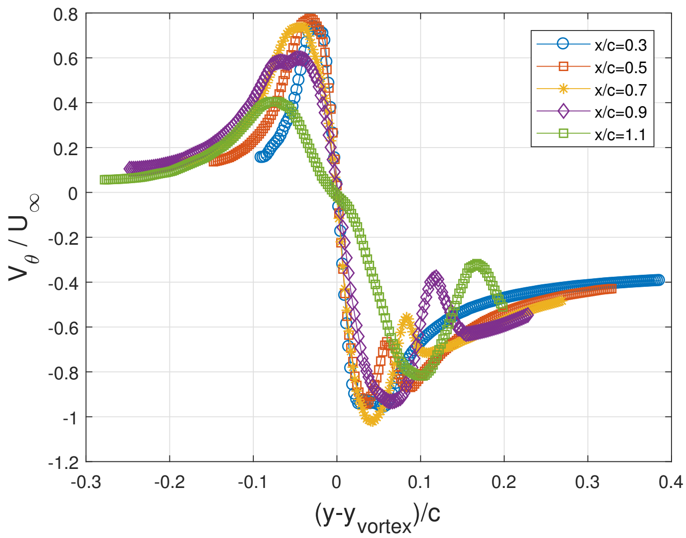

Figure 3.7: Distribution of normalized tangential velocity across a horizontal line passing through the center of the primary vortex core for a DW at angle of attack $\alpha = 20°$.

The experimental work by Ko [1] shows that the location of the vortex breakdown for a DW at angle of attack 20° is beyond the chordwise station $x/c = 0.9$. Figure 3.8 shows the contour levels of the normalized x-component of the vorticity at stations from $x/c = 0.3$ to $x/c = 1.1$. As the vortex cross section moves downstream from $x/c = 0.3$ in the chordwise direction, the size of the leading edge vortex increases and the maximum vorticity value decreases. Panels (d) to (h) show lthe cross sections of the vortical structures before, across and beyond the location of the helical breakdown of the leading edge vortex, see figure 3.2. These results contradict part of the work of Robertson *et al.* [17]. The authors stated that when a DES model is used to simulate the flow past a DW, FLUENT is unable to reproduce the vortex breakdown while OpenFOAM does. Clearly, figures 3.2 and 3.8 (panels (d) to (h)) prove that FLUENT is able to predict the vortex breakdown and its location, reproducing the diffused vortex core and spiral vortex motion [20, 26].

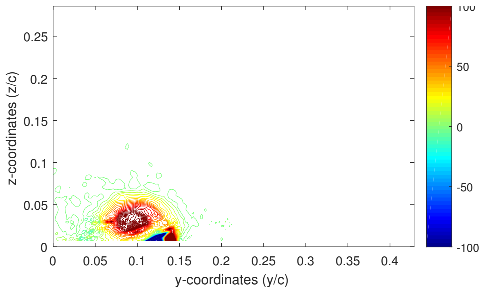

(a) $x/c = 0.3$

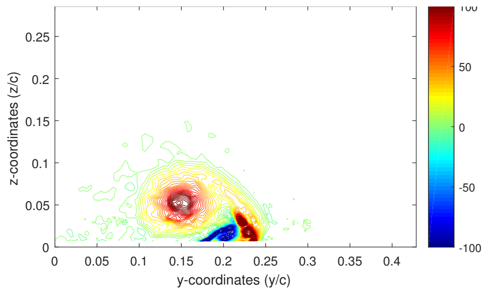

(b) $x/c = 0.5$

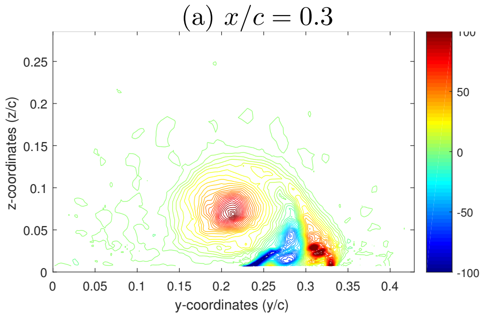

(c) $x/c = 0.7$

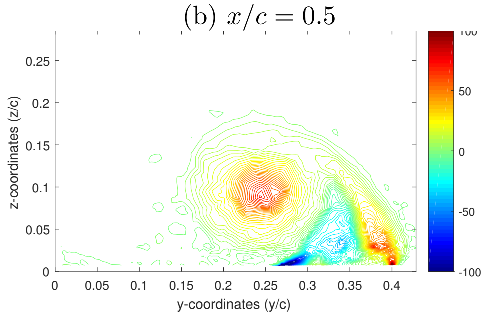

(d) $x/c = 0.85$

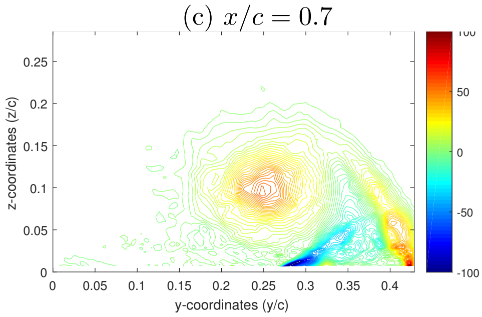

(e) $x/c = 0.9$

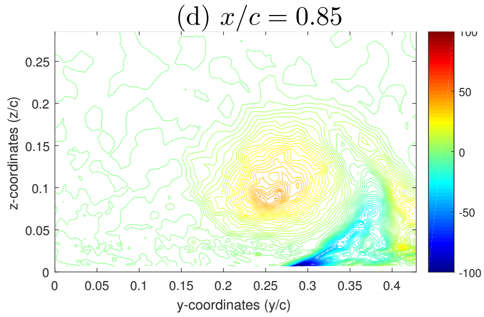

(f) $x/c = 0.95$

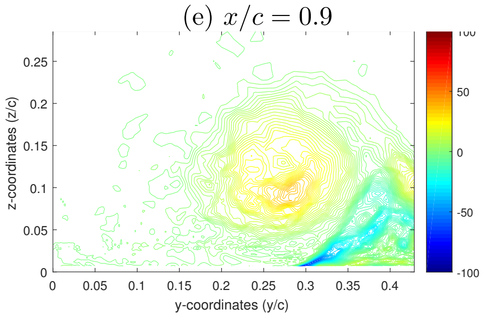

(g) $x/c = 1.0$

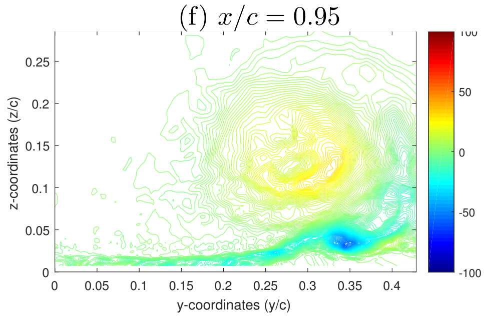

(h) $x/c = 1.1$

Figure 3.8: Contour levels of the normalized x-component of the vorticity of the primary vortex of a DW at angle of attack $\alpha = 20°$. Panels (d) through (h) show the contour levels at increasing normalized chordwise locations just upstream the location of the helical breakdown of the primary vortex, see figure 3.2

.

Figure 3.9 shows the trajectory of the leading edge vortex of a DW at angles of attack $\alpha = 10°, 15°$ and $20°$. Panel (a) shows the projection of the trajectory on the xy-plane, panel (b) on the xz-plane, while the three-dimensional trajectories are shown in panel (c). The vortex trajectory is computed by taking the apex of the wing as the reference point and using the point of maximum vorticity to indicate the vortex location at each station. The vortex trajectory for all angles of attack is similar. Panels (a) and (b) show that as the angle of attack increases, the trajectory of the primary vortex is deflected outboard and upwards, respectively.

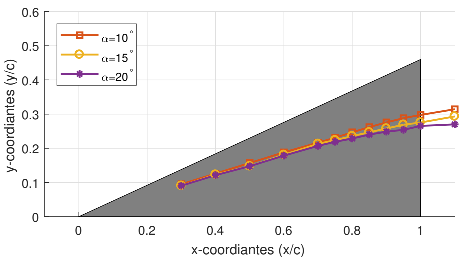

(a) Trajectory in the xy-plane

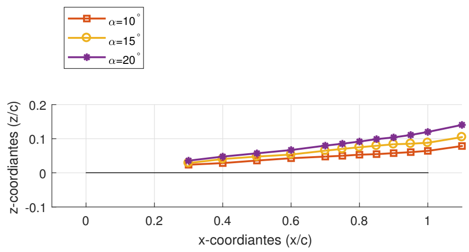

(b) Trajectory in the xz-plane

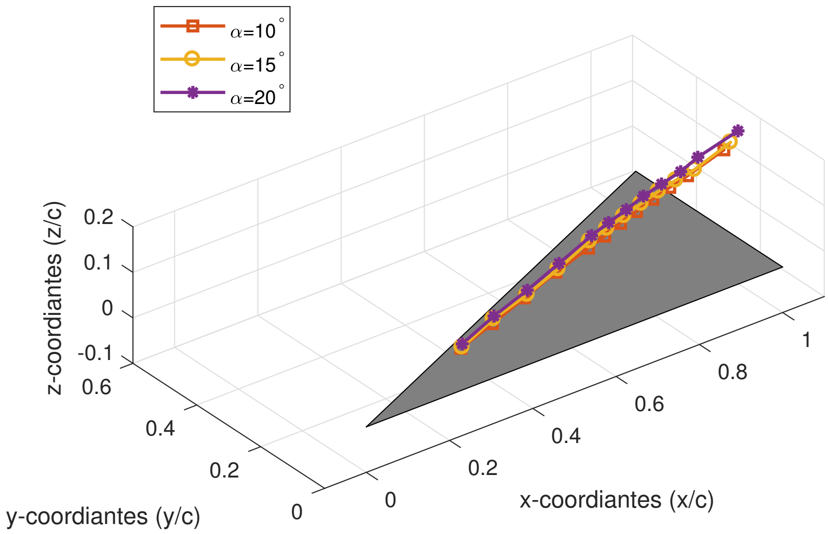

(c) Three-dimensional view of the trajectory

Figure 3.9: Trajectory of the leading edge vortex of a DW at angles of attack $\alpha = 10°$, $15°$ and $20°$.

Figure 3.10 shows the characteristics (normalized maximum tangential velocity in panel (a), maximum normalized vorticity in panel (b) and the normalized circulation in panel (c)) of the primary vortex along the chord of a DW at angles of attack $\alpha = 10°, 15°$ and $20°$. The dashed vertical line in all figures indicates the location of the trailing edge of the DW. For all angles of attack, the maximum normalized tangential velocity, panel (a), starts from a maximum value at $x/c = 0.3 - 0.5$ and then decreases slowly further downstream. At low x/c the maximum tangential velocity is higher at higher angles of attack, but they group together downstream the trailing edge of the DW. Panel (b) shows that the trend of the maximum vorticity is similar for the angles of attack. It starts from a maximum value and decreases moving downstream, as seen previously in figure 3.8. At the angle of attack $\alpha = 20°$, the maximum vorticity drops sharply to values below those for $\alpha = 10°$ and $15°$ beyond $x/c = 0.8$ probably because the leading edge vortex undergoes to breakdown near the trailing edge, which leads to a vortex with a diffused uncoherent vortex core of weaker strength, as shown previously in figure 3.8. At all angles of attack, the normalized circulation, panel (c), increases from the leading to the trailing edges because of the continuous feeding of vorticity from the shear layer and then decreases. The parameters that show the bigger change with angle of attack are the maximum tangential velocity and the circulation, which means that as the angle of attack increases, both the vortex strength and its size increase.

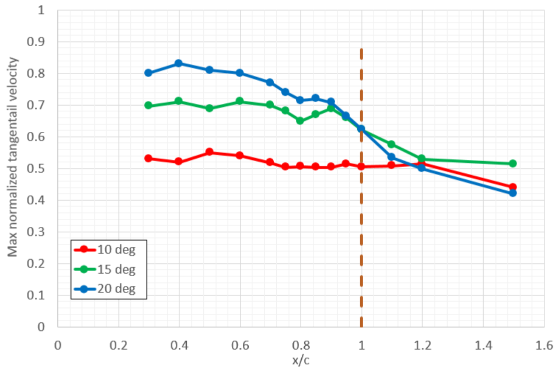

(a) Normalized maximum tangential velocity

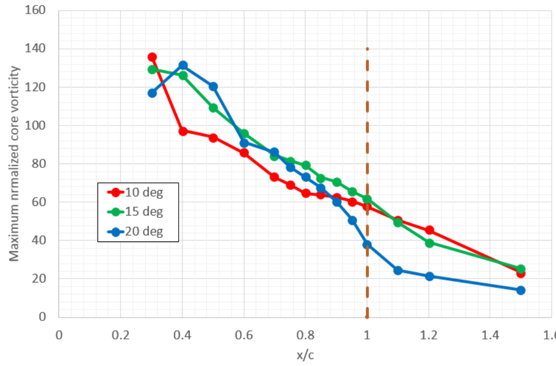

(b) Normalized maximum vorticity

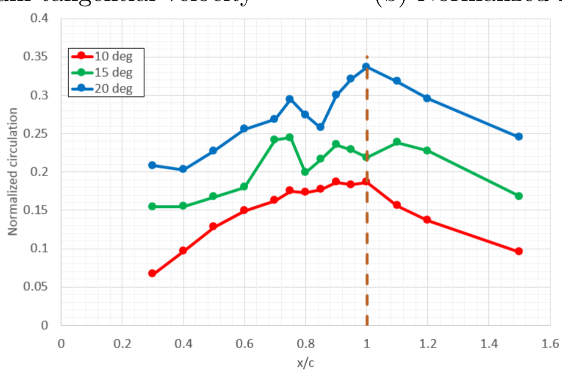

(c) Normalized vortex circulation

Figure 3.10: Variations along the chord of a DW at angles of attack $\alpha = 10°, 15°$ and $20°$ of the characteristics of the leading edge vortex.

3.1.3 Comparison between numerical and experimental results

In this section, we compare the results of our numerical simulations of a flow past a DW with the experimental results presented by Ko in [1] and Lee and Su in [2].

3.1.3.1 Characteristics of the leading edge vortex

Figure 3.11 presents the comparison with the experimental results [2] of the characteristics (panels (a) and (b) projections of the trajectory of the leading edge vortex, the normalized maximum tangential velocity in panel (c), the maximum normalized vorticity in panel (d) and the normalized circulation in panel (e)) of the primary vortex of a DW at an angle of attack $\alpha = 12°$ and $Re_\infty = 2.45 \times 10^5$. The dashed vertical line indicates the location of the DW trailing edge. Panel (a) shows the projection of the trajectory on the plane $z = 0$, the numerical results are in excellent agreement with experimental data in predicting the lateral displacement of the trajectory. The comparison of the vertical displacement (panel (b)), i.e. the projection of the trajectory on the $y = 0$ plane, with the experimental data shows lesser agreement than the previous case, but the upward movement of the vortex is captured. The numerical values of the maximum tangential velocity (panel(c)) under-predict the experimental data. However, the trend of the numerical predictions of the normalized maximum tangential velocity is similar to the one of the experimental data, it is almost constant for $0.5 \leq x/c \leq 1.0$ and then it decreases. Panel (d) shows the comparison of the maximum vorticity value, again the trend of the numerical predictions is similar to the experimental results, but the numerical results substantially under-predict the maximum vorticity at stations beyond $x/c = 0.6$ and the rate of decrease is faster than in the experimental data. Finally, panel (e) shows that the numerical values of the normalized circulation overpredicts the experimental data, which indicates that CFD predicts vortices that are larger in size of the ones measured in experiments. In all cases, panel (a) to (e), the error of the numerical predictions increases beyond the DW trailing edge, i.e. $x/c = 1.0$, because the grid becomes coarser further away from the trailing edge of the DW.

This discrepancy between numerical and experimental results has been explained by Reclari *et al.* (2015) [51], as they studied the effect of local mesh refinements on the vortex characteristics. They argue that to evaluate correctly the size of a vortex and the maximum induced tangential velocity, a local refinement is needed in order to have at least 30 points in the vortex core region. They also argue that, in global terms, the CFD predictions are in good agreement with the experimental results. Figure 3.12(a) supports this interpretation.

3.1.3.2 Aerodynamic forces coefficients

Figure 3.12 compares between the lift and drag coefficients obtained by our simulations and the experimental results of Ko [1] for a DW at $Re_\infty = 3.4 \times 10^5$. The lift coeffcient C_L shows excellent agreement at angles of attack $\alpha = 5°$ and $\alpha = 10°$, while a small error affects the results at $\alpha = 15°$ (6.4% error) and 20° (7.1% error). The numerical predictions of the drag coefficient C_D substantially underestimate the experimental results. Since the underprediction is almost constant at all angles of attack it is resonable to assume that the causes for the underprediction are the same for all angles of attack. Probable causes are: 1) The DW surface in the experiment has finite roughness, while in the numerical simulations is perfectly flat. 2) The DW model assumes a sharp leading edge, which is exactly sharp in the simulations, but not in the experiment, since sharp edges cannot be manufactured. 3) The DW mounting in the wind tunnel could also affect the readings of the force balance. 4) Another source of error could be the use of the RANS turbulence model in the boundary layer region. Large error values in drag coefficient were also obtained by Jamaluddin *et al.* [35].

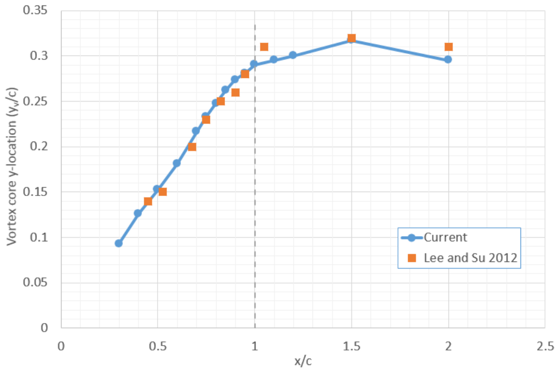

(a) Primary vortex core y-location

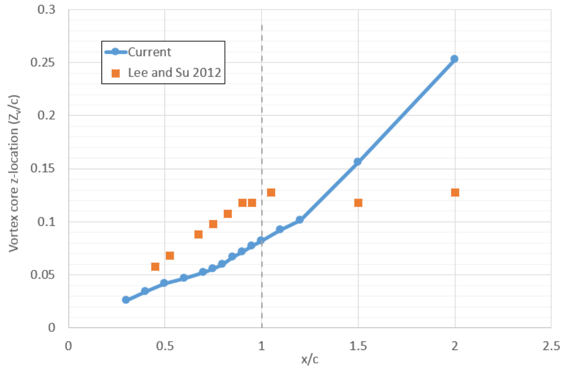

(b) Primary vortex core z-location

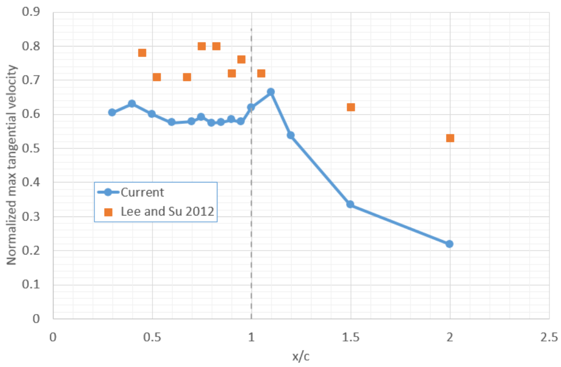

(c) Normalized maximum tangential velocity

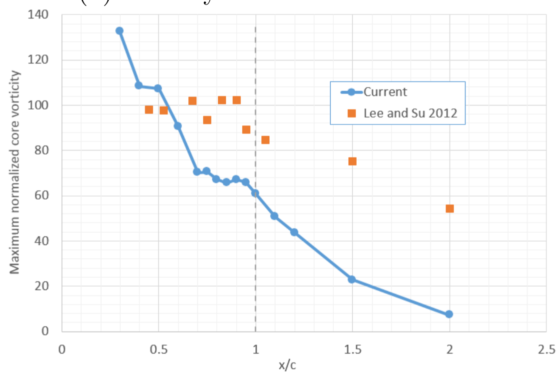

(d) Normalized maximum vorticity

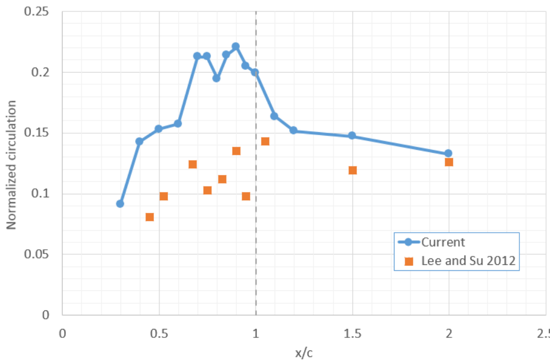

(e) Normalized vortex circulation

Figure 3.11: Comparison with experimental data [2] of the characteristics of the leading edge vortex of a DW at angle of attack $\alpha = 12°$ and $Re_\infty = 2.45 \times 10^5$.

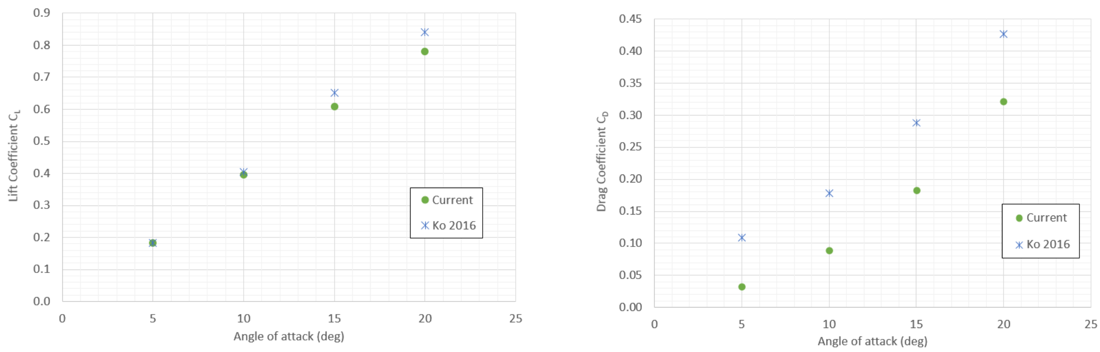

(a) Lift coefficient C_L (b) Drag coefficient C_D

Figure 3.12: Comparison of force coefficients variation with angle of attack α against experimental data from [1].

3.2 Results for a reverse delta wing

In this section we present the results of the numerical simulations of the flow past a RDW. Recall that the geometry of the DW and RDW is identical, therefore, the simulations setup for the RDW is also identical to the one used for the DW.

3.2.1 Numerical results

In this subsection we present the results of the unsteady numerical simulations performed using ANSYS Fluent. Note that we ran the unsteady simulations until the solution reached a flow time beyond 4 seconds, to bypass entirely the initial transient.

Figures 3.13 and 3.14 show the maps of the instantaneous pressure coefficient C_p over the upper and lower (leeward and windward) sides of the RDW at angles of attack $\alpha = 5°, 10°, 15°$ and $20°$ and $Re_\infty = 3.4 \times 10^5$. The instantaneous C_p distribution over the leeward surface (figure 3.13) shows, in all cases, the presence of a region of low-pressure (suction) that starts at the leading edge of the RDW and covers a large portion of the wing upper surface area. At an angle of attack 5° (panel (a)), the minimum $C_p \approx -0.75$ is located at the RDW tips and the suction region extends downstream from the wing leading edge to about half of the chord, and covers most of the wing span, except for a small portion close to the sides of the RDW. With increasing angle of attack from 10° (panel (b)) to 20° (panel (d)) the area of the suction region increases and extends further downstream. The increase in the size of the suction region is accompanied by higher and more uniformly distributed suction and thus by an increase in lift force. Note that in all cases, but especially at $\alpha = 15°$ (panel (c)) and $\alpha = 20°$ (panel (d)), the pressure distribution over the rear of the wing is very patchy. This patchiness is due to the breakdown of the spanwise vortices that are generated near the leading edge and are convected downstream, as we will show below.

Contrary to the unsteady pressure distribution on the leeward side of the RDW, figure 3.14 shows that the pressure distribution on the windward side is steady. Figure 3.14 shows that in all cases the pressure distribution is subdivided in three regions: the beveled leading edge where the pressure is maximal $0.75 \lesssim C_p \lesssim 1$, the beveled side edge where the pressure is minimal $-1.38 \lesssim C_p \lesssim -0.5$, and the flat windward side where the pressure is mostly uniform. Moving along the chord of the RDW from the sharp leading edge to the back apex, the pressure decreases slowly and monotonically from the maximum at the leading edge to ambient pressure at the apex. Only at $\alpha = 5°$ (panel (a)) and $\alpha = 10°$ (panel (b)) a thin stripe of suction is created at the end of the beveled leading edge region parallel to the leading edge. Due to the presence of the low-pressure close to the sides of the lower surface of the wing, there is a favorable pressure gradient from the central part of the wing towards the side edges of the RDW, which becomes even more favorable with increasing angle of attack. This favorable pressure gradient leads to an outboard flow on the windward side of the RDW. In all cases, at the tip of the RDW, the high pressure on the leading edge beveled region meets the beveled side suction region only separated by the beveled edge at the tip. We believe that these two regions of high-low pressure provide the physical mechanism for the initial formation of the tip vortices. This hypothesis is supported by the flow visualization obtained by injecting massless particles on the windward side of the RDW (see figure 3.30), which shows that the tip vortices are formed at the wing tips of the windward side.

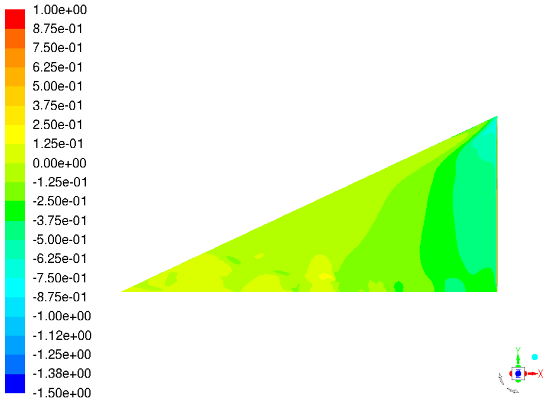

(a) $\alpha = 5°$

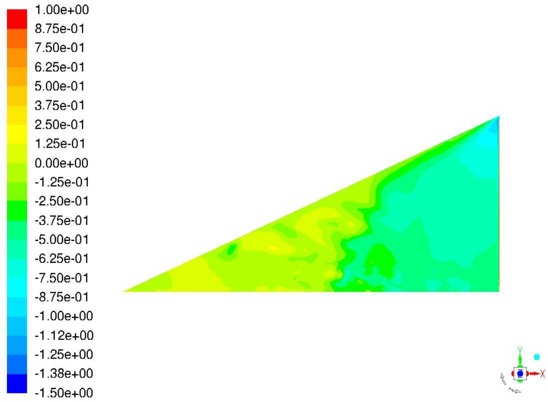

(b) $\alpha = 10°$

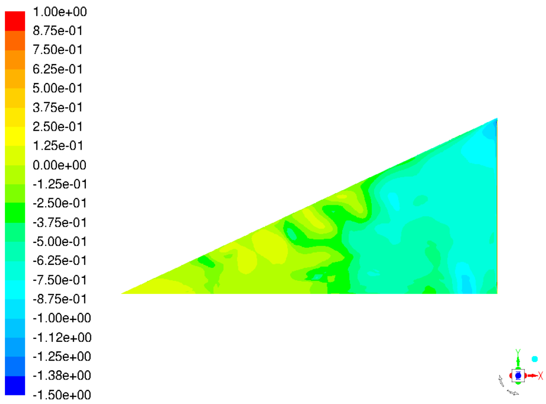

(c) $\alpha = 15°$

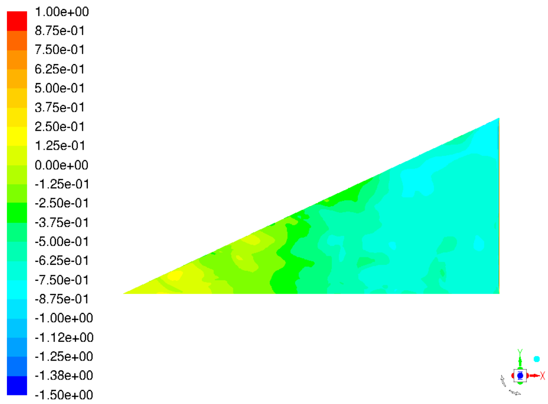

(d) $\alpha = 20°$

Figure 3.13: Instantaneous distribution of pressure coefficient C_p over the leeward side of the RDW at angles of attack $\alpha = 5°, 10°, 15°$ and $20°$.

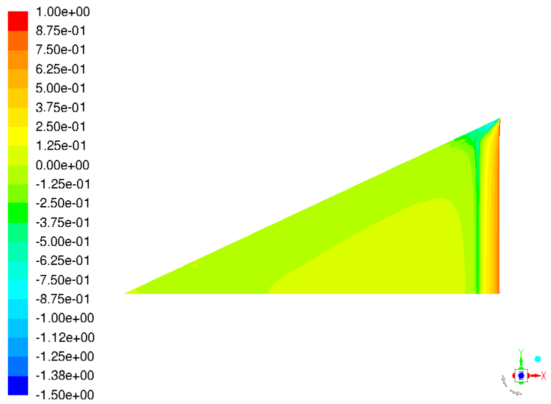

(a) $\alpha = 5°$

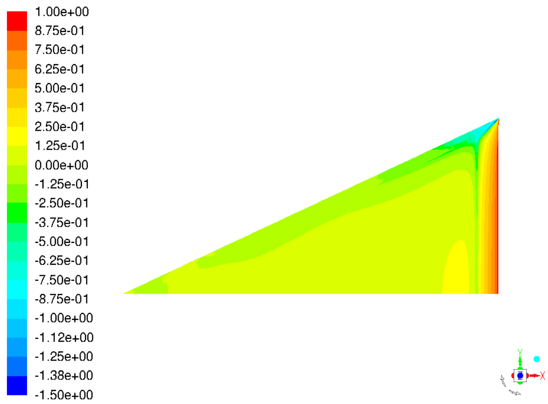

(b) $\alpha = 10°$

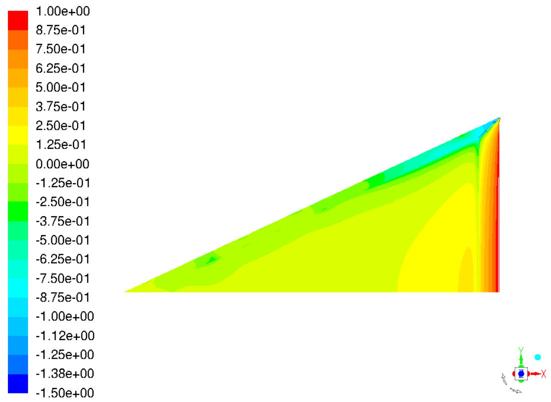

(c) $\alpha = 15°$

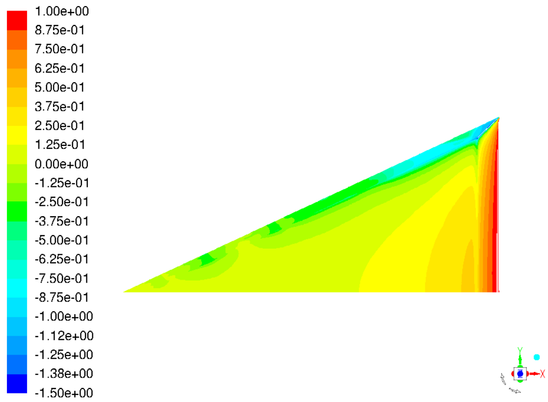

(d) $\alpha = 20°$

Figure 3.14: Instantaneous distribution of pressure coefficient C_p over the windward side of the RDW at angles of attack $\alpha = 5°, 10°, 15°$ and $20°$.

In order to understand better the nature of the unsteadiness affecting the flow on the leeward side of the RDW, we analyze the time evolution of the vorticity field. Figure 3.15 shows the instantaneous distribution of the y-component (spanwise) of the vorticity on the symmetry plane $y = 0$. In all cases, a shear layer separates from the leading edge of the RDW. The shear layer rolls up in separated vortices of negative vorticity, as shown in green/blue, that are convected downstream over the leeward side of the RDW. The shear layer is produced by the separation of the boundary layer on the windward side of the RDW. As the shear layer rolls up, vortices sometimes interact with the leeward side of the RDW generating patches of positive vorticity, shown in red. As the angle of attack increases, from panel (a) to (d), the leading edge shear layer roll up happens at more upstream locations, and stronger vortices of larger sizes are generated. In all cases the separated flow spans the entire chord of the RDW and produces a turbulent wake leaving the back apex of the RDW. In the case $\alpha = 5°$ (panel (a)), the separate region is thin but it thickness grows substantially with increasing angle of attack (panels (b)-(d)).

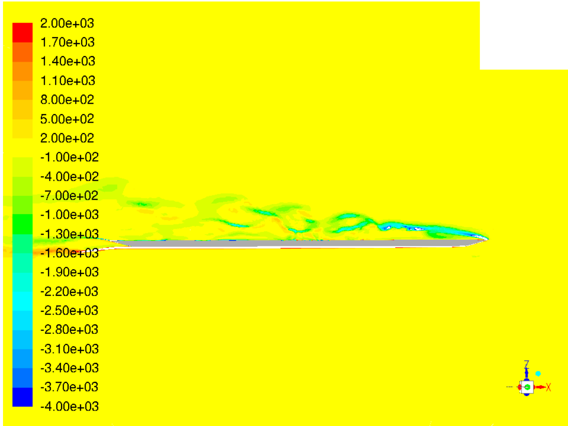

(a) $\alpha = 5°$

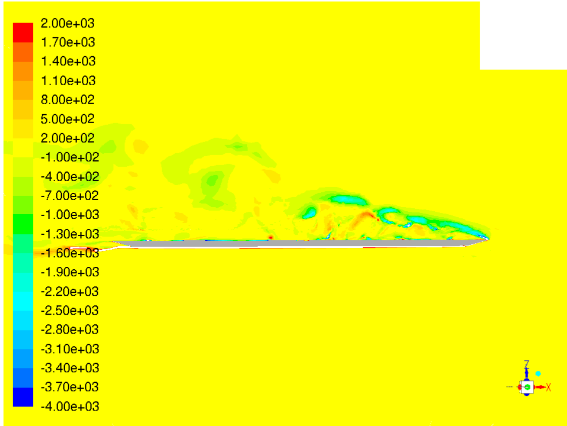

(b) $\alpha = 10°$

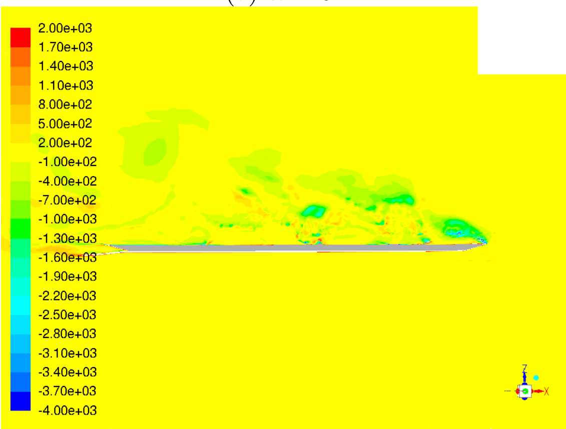

(c) $\alpha = 15°$

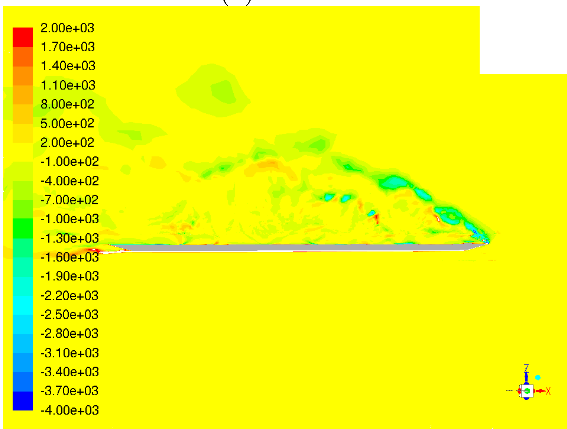

(d) $\alpha = 20°$

Figure 3.15: Instantaneous distribution of the y-component (spanwise) of the vorticity on the symmetry plane $y = 0$ of the RDW at angles of attack $\alpha = 5°, 10°, 15°$ and $20°$.

Figures 3.16(a-d) show the instantaneous distribution of the pressure coefficient C_p on the symmetry plane ($y = 0$) of the RDW at angles of attack $\alpha = 5°, 10°, 15°$ and $20°$, respectively. In all the cases, there is a suction bubble above the front part of the RDW that increases in size with increasing angle of attack. The suction bubble is mirrored by high pressure bubble on the front of the windward side of the RDW. Aside from the main bubbles, there are small, separate circular patches of high suction over the leeward side of the RDW that move downstream. Comparing figures 3.15 and 3.16, the circular patches of high suction correspond to the vortices produced by the roll up of the shear layer. As the vortices are convected downstream, the corresponding patches of low pressure move downstream. Therefore the pressure distribution over the leeward side of the RDW is unsteady. And the patchiness of the pressure distributions shown in figure 3.13 represent the footprints of the vortices that are convected downstream.

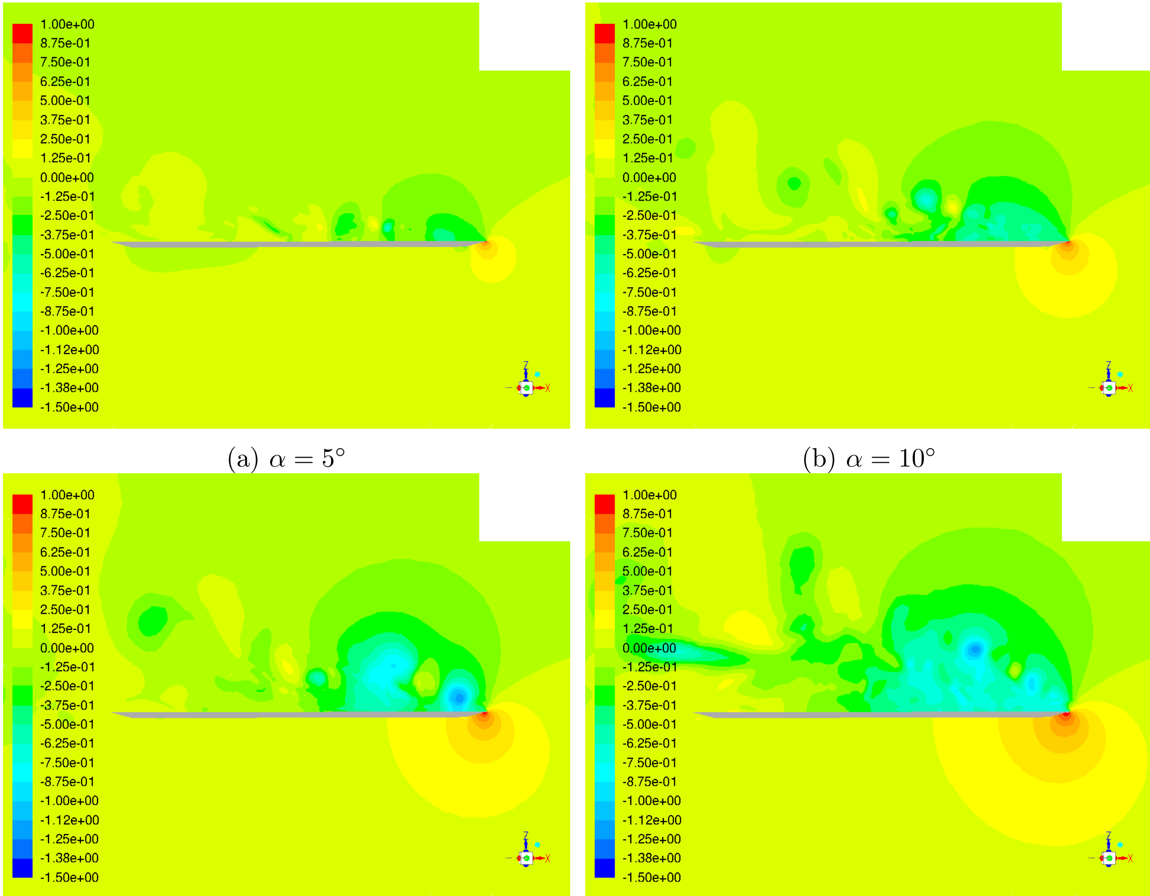

(a) $\alpha = 5°$

(b) $\alpha = 10°$

(c) $\alpha = 15°$

(d) $\alpha = 20°$

Figure 3.16: Instantaneous distribution of the pressure coefficient C_p on the symmetry plane $y = 0$ of the RDW at angles of attack $\alpha = 5°, 10°, 15°$ and $20°$.

Figure 3.17 shows the instantaneous chordwise distribution, at the symmetry plane $y = 0$, of the pressure coefficient C_p over the upper and lower surfaces of the RDW at angles of attack $\alpha = 5°, 10°, 15°$ and $20°$. The plots show that there are separate peaks of suction that decrease in magnitude in the downstream direction. In addition, as the angle of attack increases, the magnitudes of the various peaks increase, indicating higher suction. Although, the maximum peak of negative pressure corresponds to $\alpha = 15°$, the overall suction is highest at $\alpha = 20°$. Note that the spike in pressure on the lower surface corresponds to the high pressure on the beveled surface at the leading edge. Note also that the adverse pressure gradient in the recovery region of the wing upper surface is mild compared to the one in conventional wings, which explains the potential of a RDW to fly at high angles of attack. At $\alpha = 20°$, a small region of negative lift, close to the RDW trailing edge, leads to some loss of lift.

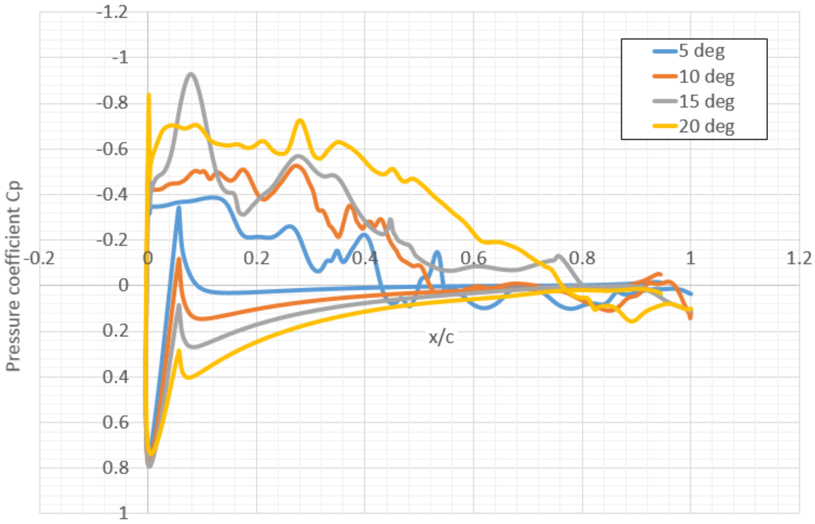

Figure 3.17: Chordwise instantaneous distribution of the pressure coefficient C_p on the upper and lower sides of a RDW at angles of attack $\alpha = 5°, 10°, 15°$ and $20°$.

Figure 3.18 shows the instantaneous iso-surfaces of vorticity magnitude (300 panel (a), 500 panel (b), 700 panel (c)) over the leeward side of a RDW at angles of attack $\alpha = 10°, 15°$ and $20°$ colored in proportion to the values of the pressure coefficient C_p. Clearly, the different values of vorticity used to produce the iso-surfaces indicate that the magnitude of the vorticity field over the RDW increases substantially with increasing angle of attack. In all cases, two tip vortices confine the spanwise vortical structures to the leeward side of the RDW. In all cases, the iso-surfaces leave smoothly the leading edge of the RDW, this smooth part of the iso-surface visualizes the shear layer separating from the leading edge. In all cases, the shear layer rolls up and forms complex spanwise vortical structures that pair with each other as they are convected downstream, forming a narrow wake confined by the tip vortices. The intensity of these vortical structures is visualized by their colors, orange/yellow at $\alpha = 10°$, yellow/greeen at $\alpha = 15°$ and green/blue at $\alpha = 20°$. These vortical structures are responsible for a large portion of the lift generated by a RDW. The large vortical spanwise structures we see in the figure correspond to the spanwise vortex filaments mentioned in the work of Ko [1] which can be seen in figure 1.14.

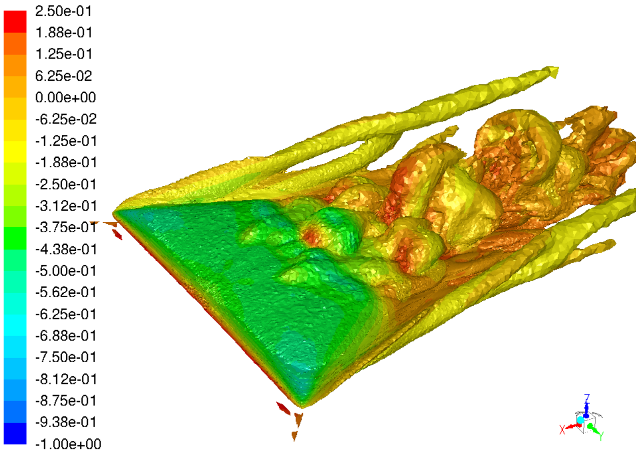

(a) $\alpha = 10°$

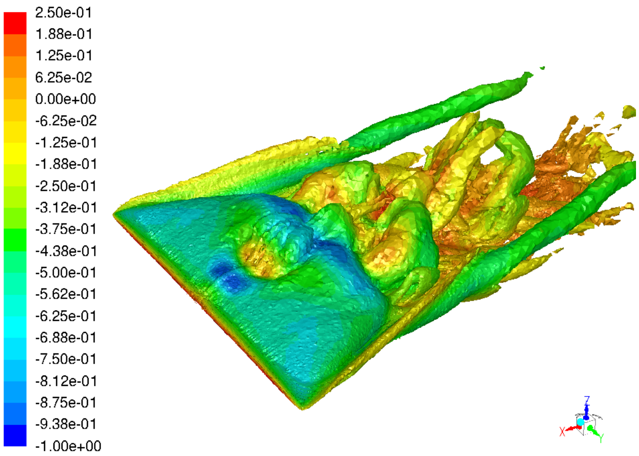

(b) $\alpha = 15°$

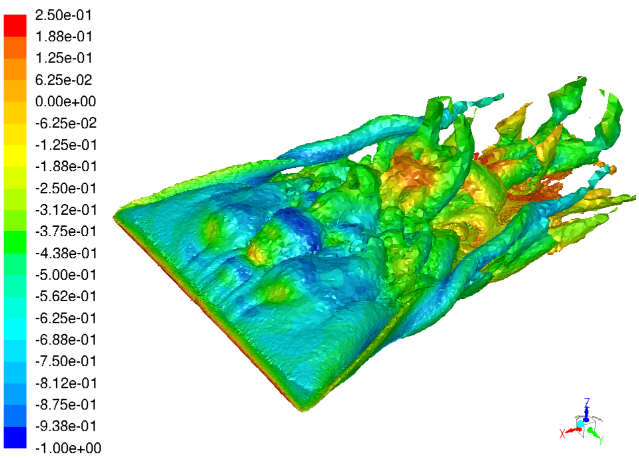

(c) $\alpha = 20°$

Figure 3.18: Instantaneous iso-surfaces of vorticity magnitude (300 panel (a), 500 panel (b), 700 panel (c)) over the leeward side of the RDW at angles of attack $\alpha = 10°, 15°$ and $20°$ colored in proportion to the pressure coefficient C_p.

3.2.2 Characteristics of the tip vortex of a RDW

In this subsection we present and analyze the characteristics of the tip vortices of a RDW. The analysis and presentation is similar to the one given in section 3.1.2 for the characteristics of the leading edge vortices of a DW. Note, however, that the leading edge vortices of a DW and the tip vortices of a RDW have nothing in common. The leading edge vortices lay over the DW while the tip vortices lay outside the planform of the RDW. The leading edge vortices contribute directly to the lift of a DW, while the tip vortices of a RDW do not contribute, at least directly, to the lift of a RDW.

Figure 3.19 shows the trajectory of the tip vortex of a RDW at angles of attack $\alpha = 10°, 15°$ and $20°$ and $Re_\infty = 3.4 \times 10^5$. Panel (a) shows the projection of the trajectory on the xy-plane, panel (b) shows the projection on the xz-plane and panel (c) shows a three-dimensional view of the trajectory. The trajectory is computed using the middle point of the leading edge of the RDW as the reference point and using the point of maximum vorticity to indicate the vortex location at each station. As the angle of attack increases, panels (a) and (b) show that the trajectory of the tip vortex is deflected inboard and upwards.

Figure 3.20 shows the characteristics of a tip vortex of the RDW at angles of attack $\alpha = 10°, 15°$ and $20°$ and $Re_\infty = 3.4 \times 10^5$. The normalized maximum tangential velocity is shown in panel (a), the maximum normalized vorticity in panel (b) and the normalized vortex circulation in panel (c). The vertical dashed line indicates the location of the trailing edge of the RDW. For all angles of attack considered, the trends of the characteristics of the tip vortex are similar. In all cases, the maximum tangential velocity and the maximum vorticity value decrease along the chord and moving further downstream. The vortex circulation, instead, increases with downstream distance, and this is due to the continuous feeding of the tip vortex by the shear layer coming from the windward side of the RDW. The results presented in figures 3.19 and 3.20 agree with the trend of the results obtained by Lee and Ko in [30].

Figure 3.21 shows the variation of normalized tangential velocity along a horizontal line passing through the center of the tip vortex of a RDW at $\alpha = 20°$. The location of the center of the tip vortex is found by detecting the location where the maximum of the x-component of the vorticity matches the minimum of the fluid velocity on the yz-plane. Similar to the case of the DW, as we move downstream, the maximum tangential velocity decreases and vortex size increases. Note that the complex flowfield over the leeward side affects the tangential velocity distribution, and therefore it is not axially symmetric.

Figure 3.22 shows the contours of the time averaged normalized x-component of vorticity at different chordwise stations for the RDW at angle of attack $\alpha = 10°$. In all chordwise stations, the shear layer from the windward surface leaves the wing parallel to the surface and rolls up around the tip vortex. The tip vortex, therefore, has an arm and fist configuration, where the arm represents the feeding shear layer coming out from the wing lower surface, and the fist is the concentrated vorticity region. As shown in figure 3.20, we observe the inwards and upwards movement of the vortex core with downstream distance. Also, in agreement with figure 3.20, the size of the tip vortex increases with downstream distance.

By only looking at the vorticity contours shown in figure 3.22, one cannot understand how the tip vortex is formed nor at which chordwise station does it roll up. To this end, in figure 3.23 we superimpose the vectors of the time averaged velocity field to the normalized vorticity contours. Figure 3.23 shows a cross flow coming inwards, from the tip vortex to the leeward side of the RDW. This cross flow is induced by the low-pressure region that is created by the spanwise vortices over the leeward side of the RDW. Therefore, the tip vortices contributes indirectly to the generation of lift. They confine the spanwise vortical structures over the leeward side of the RDW. Moreover, in agreement with the results of Lee and Ko [30] and Altaf *et al.* [29], it took a considerable downstream distance for the vortex to roll up, and this happened at a chord wise station beyond $x/c = 0.7$.

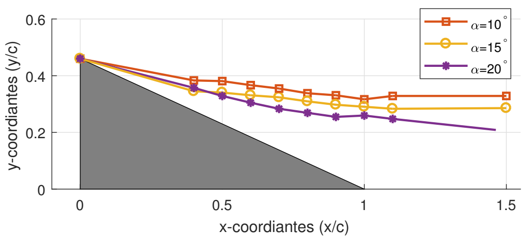

(a) Trajectory in the xy-plane

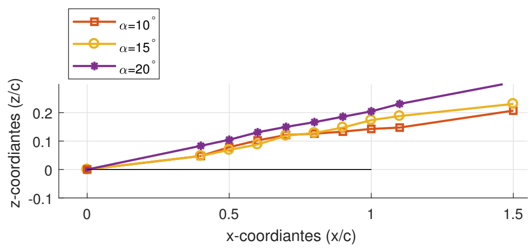

(b) Trajectory in the xz-plane

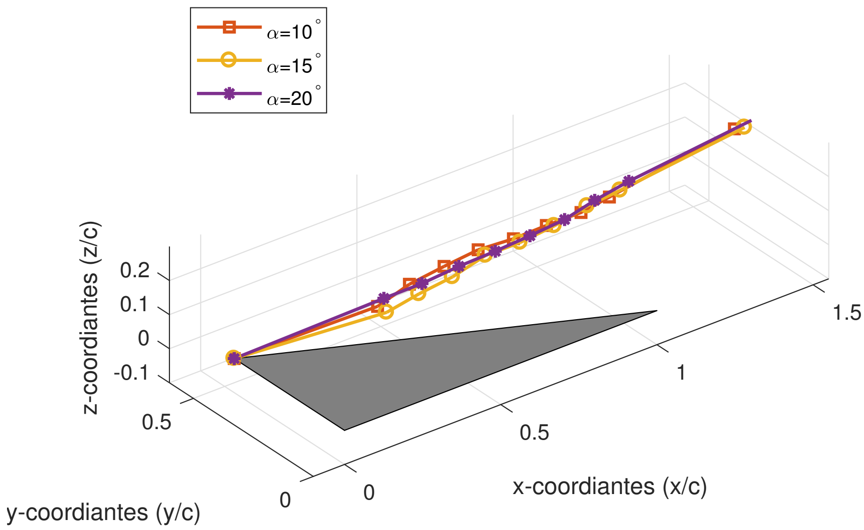

(c) Three-dimensional view of the trajectory

Figure 3.19: Trajectory of the tip vortex of a RDW at angles of attack $\alpha = 10°$, $15°$ and $20°$.

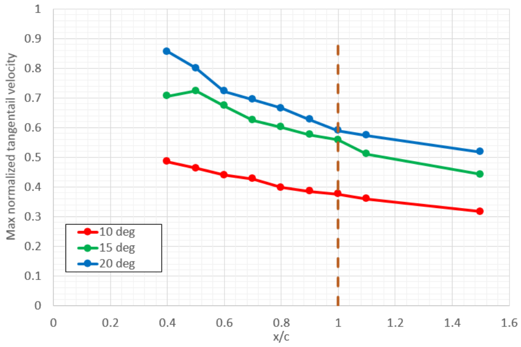

(a) Normalized maximum tangential velocity

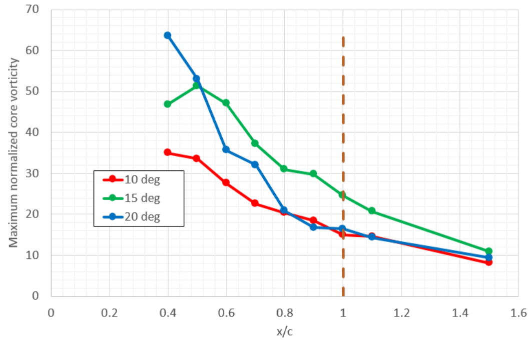

(b) Normalized maximum vorticity

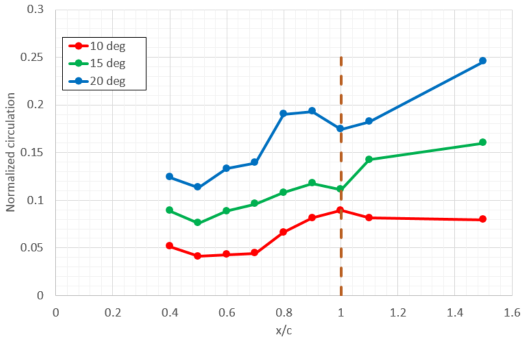

(c) Normalized vortex circulation

Figure 3.20: Characteristics of the tip vortex of a RDW at angles of attack $\alpha = 10°, 15°$ and $20°$.

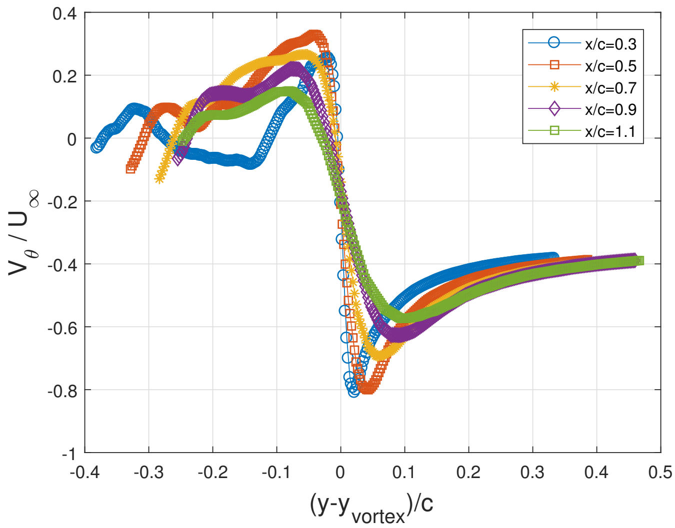

Figure 3.21: Distribution of normalized tangential velocity across a horizontal line passing through RDW tip vortex center at different chordwise stations for angle of attack $\alpha = 20°$.

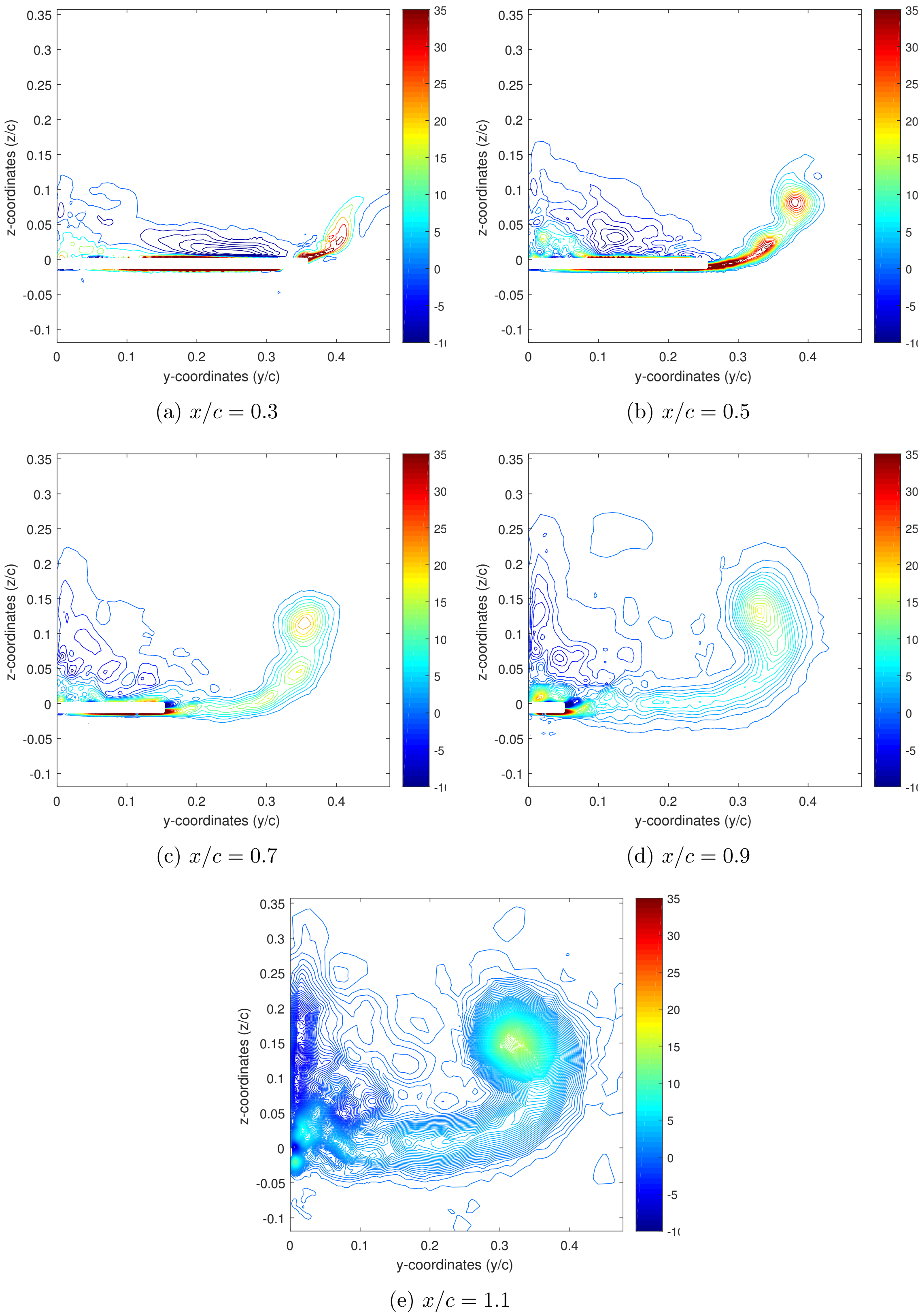

Figure 3.22: Contours of the time averaged normalized x-component of vorticity of the tip vortex of a RDW at angle of attack $\alpha = 10°$ at various chordwise stations.

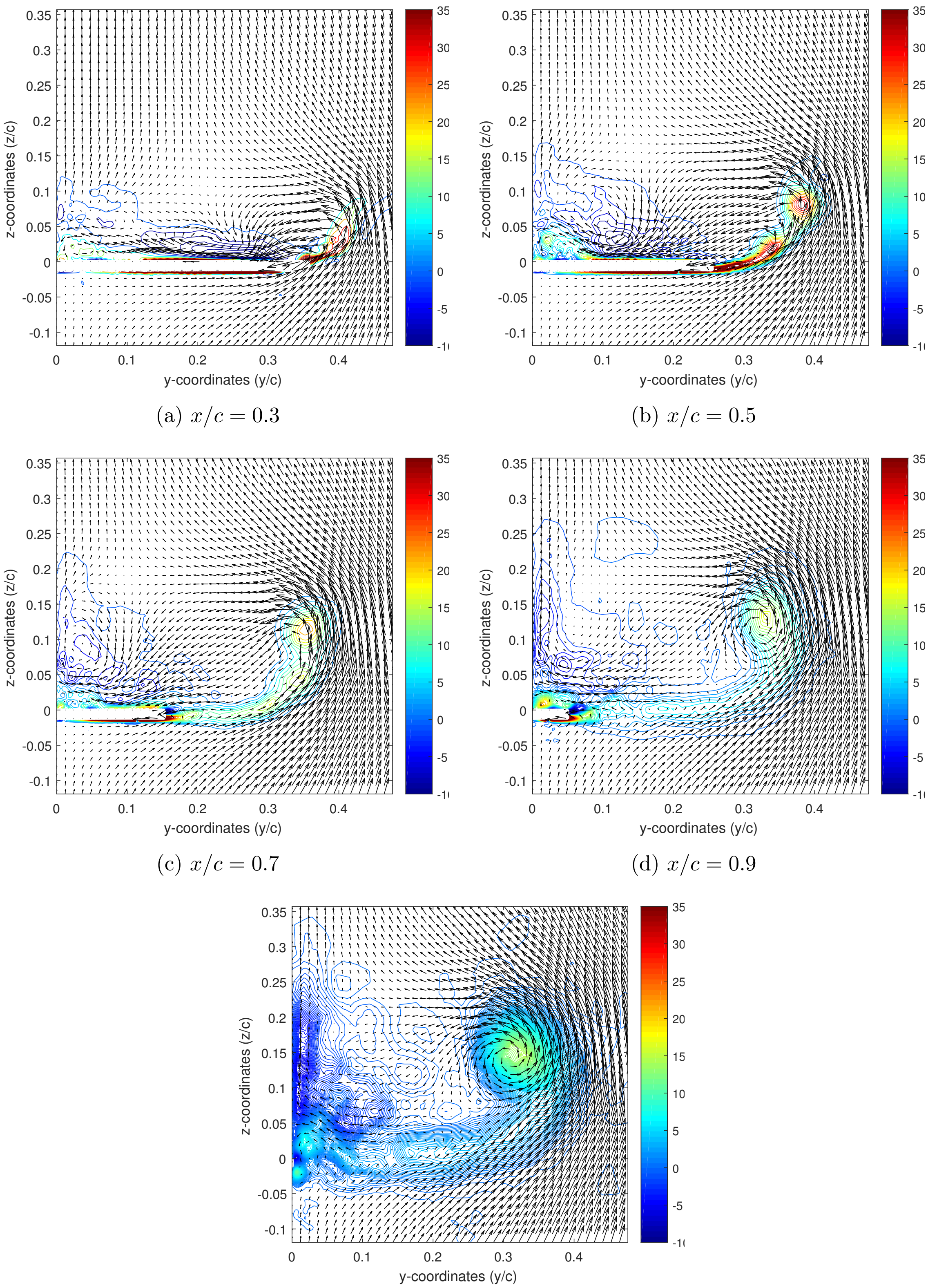

(a) $x/c = 0.3$

(b) $x/c = 0.5$

(c) $x/c = 0.7$

(d) $x/c = 0.9$

(e) $x/c = 1.1$

Figure 3.23: Vectors of averaged cross velocity and contours of normalized x-component of vorticity at various chordwise stations for the RDW at $\alpha = 10°$.

3.2.3 Unsteady flow characteristics

In this subsection, we analyze the characteristics of the unsteady flow past a RDW and develop an understanding of the physical mechanisms responsible for such unsteadiness using the results presented in the subsections 3.2.1 and 3.2.2.

Figure 3.24 shows the time histories of the lift coefficient C_L for the flow past a RDW at angles of attack $5°, 10°15°$ and $20°$ and the associated PSD's. At all angles of attack, the PSD of the lift coefficient shows a dominant peak with a well-defined Stouhal number. The peak location, i.e. the Strouhal number, changes with increasing angle of attack, at $\alpha = 5°$ the peak corresponds to a Strouhal number of 0.33, at $\alpha = 10°$ is $St = 0.19$, at $\alpha = 15°$ is $St = 0.13$ and at $\alpha = 20°$ is at $St = 0.07$. We hypothesize that these dominant peaks identify the frequency of vortex formation and shedding from the leading edge of the RDW. We will verify our hypothesis in the next paragraph. At all angles of attack, the dominat peak is surrounded by lower peaks especially at higher Strouhal numbers. These peaks correspond to high frequency unsteady phenomena that contribute to make complex the flow past the RDW. Figure 3.25 summarizes the frequency variation of the primary peak versus angles of attack. The decrease of the Strouhal numbers associated to vortex shedding is weakly nonlinear but monotonic, the Strouhal number of the dominant peaks deacreses as the angles of attack increases.

In this paragraph we verify the hypothesis made in the previous one. To this end, we present, in figure 3.26, a sequence of instantaneous snapshots of the distribution of the normalized y-component of the vorticity field on the symmetry plane $y = 0$ for the flow past a RDW at angle of attack $\alpha = 15°$ at time instants t = 4.785, 4.807, 4.83, 4.852, 4.875 and 4.898 seconds. The sequence of snap shots, panels (a) to (f), shows that vortices of negative y-component of vorticity are generated by the roll up of the shear layer that separates from the leading edge of the RDW, shed into the flow over the leeward side of the RDW and convected downstream, where their strength and the maximum magnitude of y-vorticity decrease. To understand the relationship between vortex shedding and the frequency of the dominant peaks observed in the PSDs of the lift coefficients shown in figure 3.25, we present, in figure 3.27, the instantaneous contour maps of the y-component of vorticity along with the plots of the chordwise pressure coefficient distribution, both at the same time instant of time. The vortices generated by the roll up of the shear layer and shed into the flow create patches of low-pressure underneath them on the leeward side of the RDW, as shown in figures 3.13. These patches of low pressure are the footprints of the vortices as shown in figure 3.27. As time passes, figures 3.26 and 3.27 show that the vortices are convected downstream and with them move their footprints on the leeward side of the RDW. Since the suction generated by the spanwise vortices shed from the leading edge of the RDW contributes substantially to the lift produced by a RDW, then the frequency of vortex shedding affect the time evolution of the lift coefficient and, ultimately, is detected by the PSD analysis of the time history of the lift coefficient as shown in figure 3.24. Finally, figure 3.28 presents the instantaneous velocity vector field at time t = 4.346 seconds on the symmetry plane $y = 0$, where the velocity vector field is bi-dimensional by construction, of a RDW at angle of attack $\alpha = 10°$. The velocity vector field shows several vortices, with the closest to the leading edge that is rolling up. This velocity vector field is in agreement with the smoke visualizations presented by Ko [1], which are shown in figure 1.14.

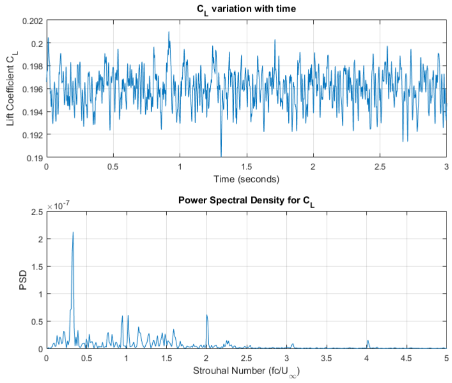

(a) $\alpha = 5°$

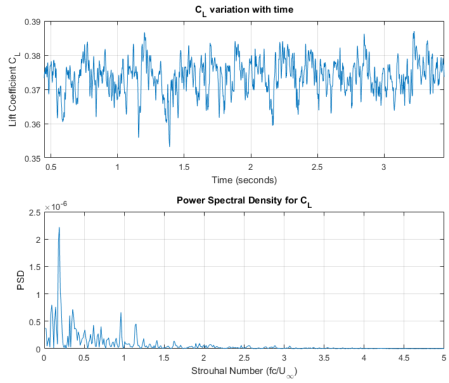

(b) $\alpha = 10°$

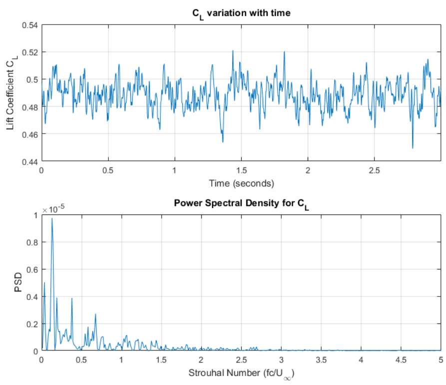

(c) $\alpha = 15°$

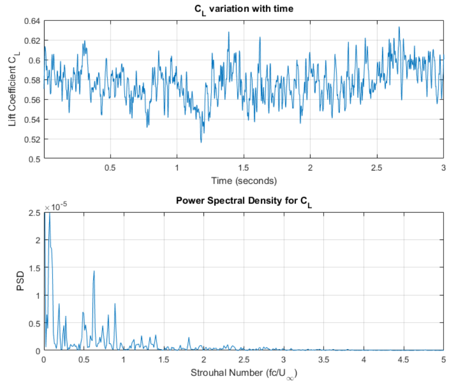

(d) $\alpha = 20°$

Figure 3.24: Time history and PSD for the lift coefficient C_L of the RDW at angles of attack $\alpha = 5°, 10°, 15°$ and $20°$.

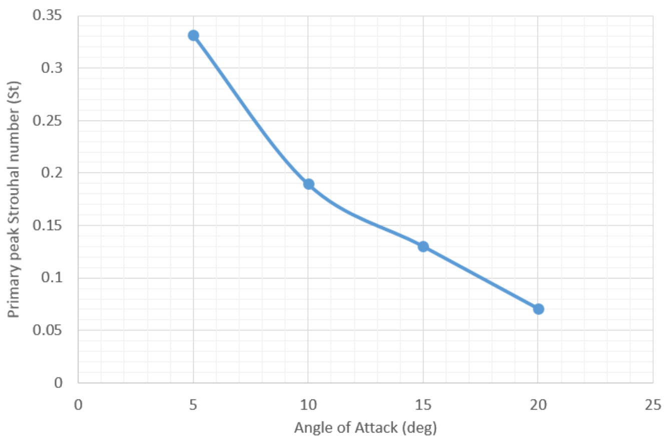

Figure 3.25: Variation of primary peak Strouhal number of the PSD of the lift coefficient C_L time history with angle of attack α.

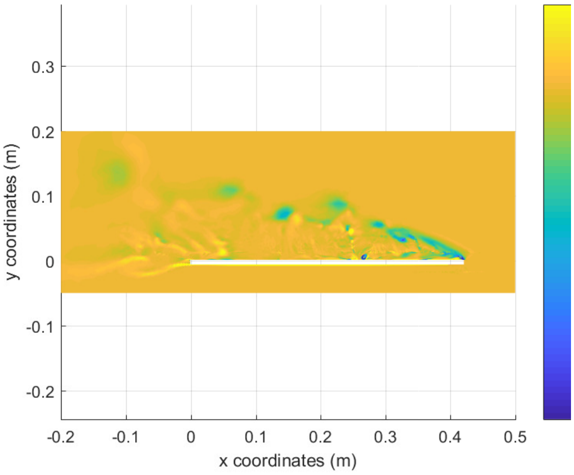

(a) t = 4.785 seconds

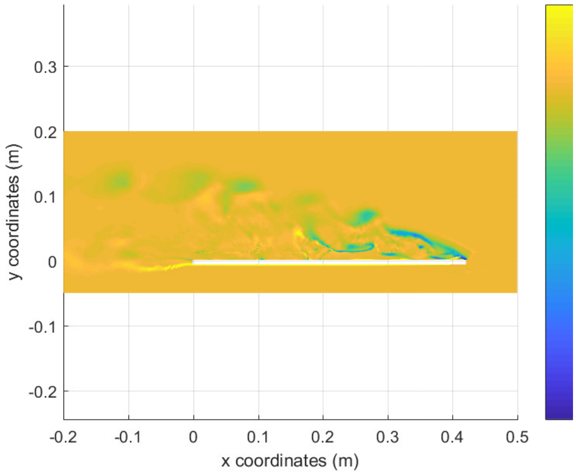

(b) t = 4.807 seconds

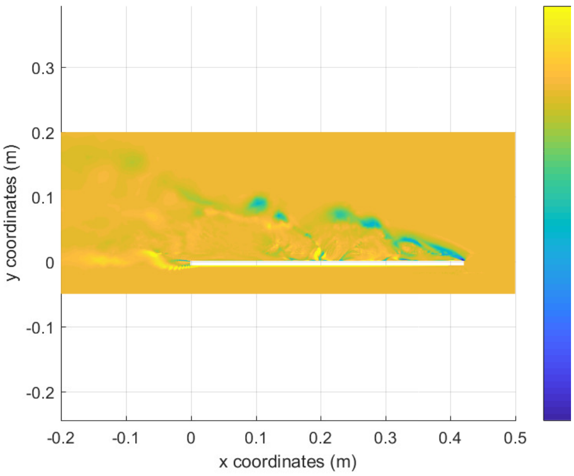

(c) t = 4.83 seconds

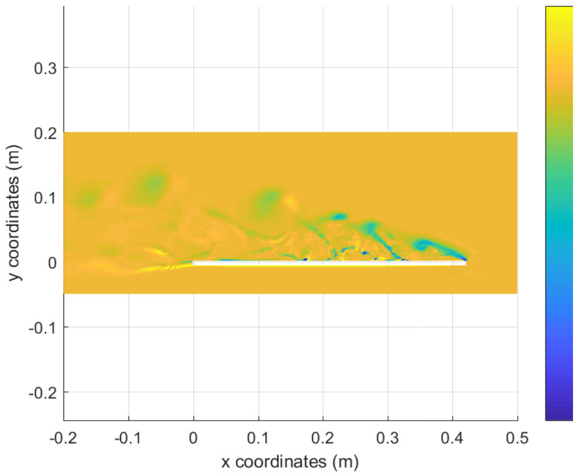

(d) t = 4.852 seconds

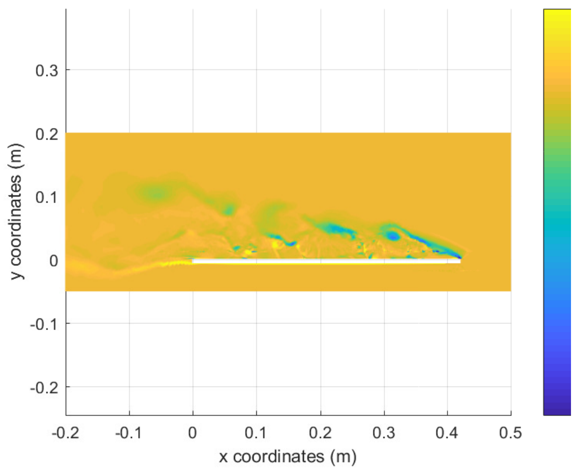

(e) t = 4.875 seconds

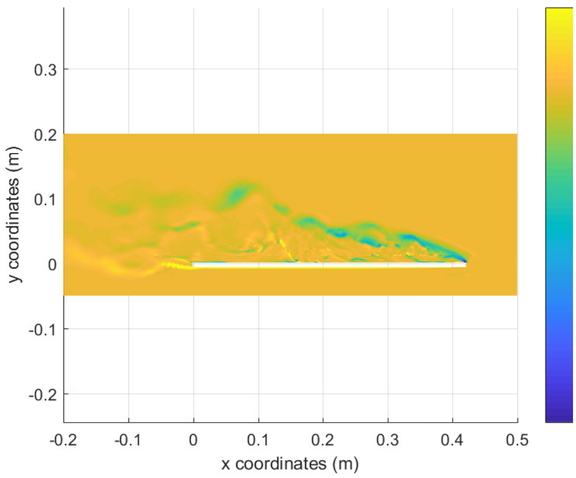

(f) t = 4.898 seconds

Figure 3.26: Sequence of instantaneous snapshots showing the contour maps of the normalized y-component of vorticity at the symmetry plane $y = 0$ of a RDW at $\alpha = 15°$ at time instants t = 4.785 to 4.898 seconds.

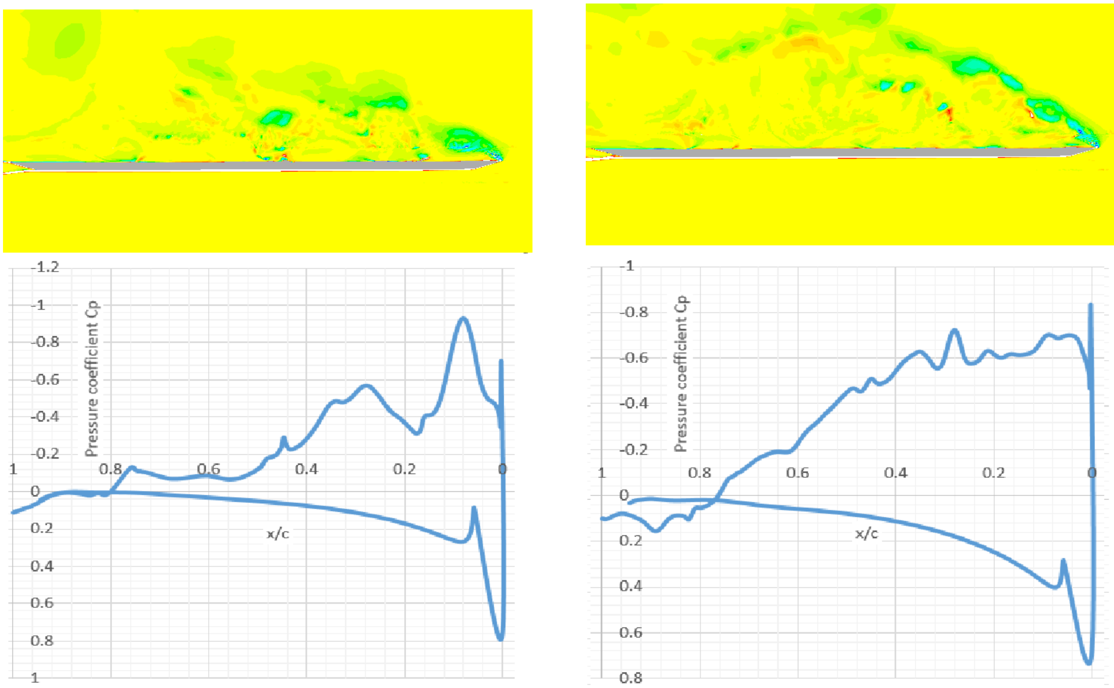

(a) $\alpha = 15°$ (b) $\alpha = 20°$

Figure 3.27: Effect of spanwise vortices on the instantaneous pressure field at angles of attack $\alpha = 15°$ and $20°$.

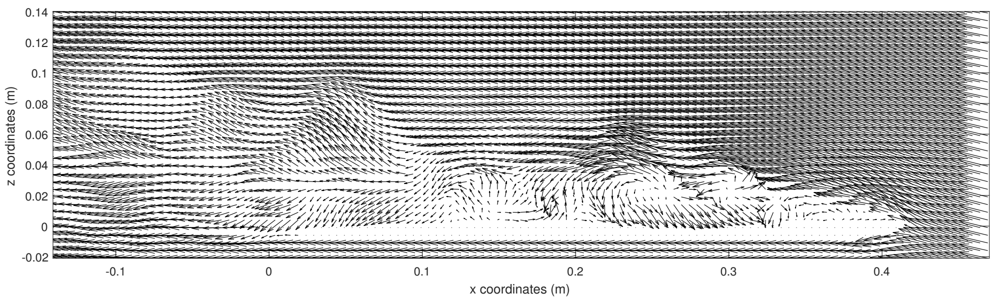

Figure 3.28: Instantaneous velocity vectors at the symmetry plane $y = 0$ for a RDW at angle of attack $\alpha = 10°$ at t=4.346 seconds.

Jamaluddin *et al.* [35] used a steady state solver to obtain the streamlines shown in figure 1.15. To mimic a steady state solution, we time averaged the vorticity field obtained from our simulations. Figure 3.29 shows the time averaged y-component of vorticity at the symmetry plane $y = 0$ when the RDW is at angles of attack $\alpha = 5°$ and $20°$. Figure 3.29 indicates that the time averaging process leads to a total loss of the individual vortices shed from the leading edge of the RDW. The resulting time averaged vorticity field shows only a shear layer separating from the leading edge of the RDW, a shear layer that quickly diffuses. This result provides an explanation for the streamline pattern shown in figure 1.15, which

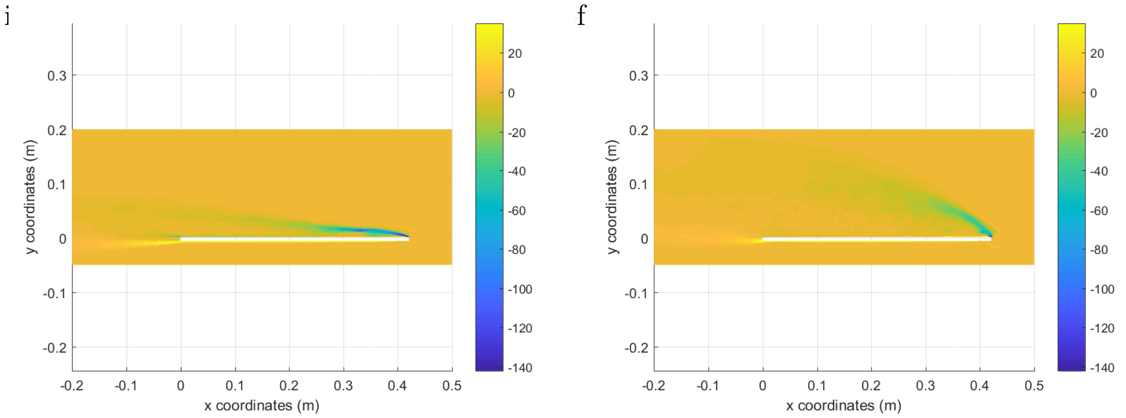

(a) $\alpha = 5°$ (b) $\alpha = 20°$

Figure 3.29: Time averaged y-component of vorticity field at the symmetry plane $y = 0$ when the RDW is at angles of attack $\alpha = 5°$ and $20°$.

3.2.4 Particle tracks visualization

To visualize the flowfield over both the leeward and windward sides of the RDW, we inject massless particles at two different locations, the first along a line aligned with the wing leading edge, 5 cm away from it, the second along a line aligned with the wing leading edge, 7 mm below it. The length of the two injection lines is 25 cm, 6 cm longer than the RDW leading edge. About 2500 massless particles are injected into the flow at each time step. We select the locations from where the particles are injected in accordance with the locations of the smoke lines that were used in the visualizations by Ko [1] shown in figure 1.14.

Figure 3.30 shows the instantaneous snapshot of the massless particles convected by the flowfield past the RDW at angle of attack $\alpha = 14°$. In panels (a) to (d) the particles are colored in proportion to the residence time, i.e. the time elapsed since the particle was injected into the flow, while in panel (e) they are colored in proportion to the z-component of velocity. Panels (a) and (b) show the instantaneous snapshots of the massless particles injected from the upper injection line. Panels (a) and (e) show that the particles are lifted up by the unsteady vortical structures created by the roll up of the shear layer that separates from the leading edge, as shown by figure 3.15 and 3.18. Panel (b) shows that there is nearly no flow from the leeward side to the windward side of the RDW. Panels (c) and (d) show the instantaneous snapshots of the massless particles injected from the lower injection line. Panel (d) shows that the massless particles are entrapped in the tip vortices. Panel (c) shows no spillage of particles from the windward side to the leeward side of the RDW, aside near the back apex of the wing. This visualization supports the hypothesis that the tip vortices are generated exclusively on the windward side of the RDW. Panel (e) shows yellow or green massless particles entrapped into the spanwise vortical structures on the leeward side of the RDW. The colors indicate an alternating sign of the z-component of velocity indicating that the particles are entrapped by the spanwise vortical structures. As the particles are convected downstream past the back apex of the RDW, they visualize a complex wake.

3.2.5 Comparison of RDW results with experimental data

In this section we compare the results of the numerical simulations of the flow past a RDW at angle of attack $\alpha = 12°$ and $Re_\infty = 2.45 \times 10^5$ with the experimental results by Lee and Su (2012) [2], and the results for the flow past a RDW at $Re_\infty = 3.4 \times 10^5$ with the experimental results of Ko (2016) [1].

3.2.5.1 Characteristics of the tip vortex

The characteristics of the tip vortex are obtained by time averaging the unsteady flowfield, consistently with experimental data obtained by time averaging PIV data. Figures 3.31(a) and (b) show that the numerically estimated tip vortex trajectory is in good agreement with experimental data [2]. The maximum tangential velocity (panel (c)) is estimated by averaging the negative and positive peak values shown in figure 3.21. The comparison with experimental results gives a good agreement between $x/c = 0.5$ and $x/c = 0.8$, but it is overestimated before $x/c = 0.5$, and underestimated beyond $x/c = 0.8$. The maximum vorticity within the vortex core (panel (d)) is largely underestimated by the numerical simulations. The estimated circulation of the tip vortex is almost twice as the experimental data, but with a similar trend. Apparently, the CFD simulations tend to predict larger vortices than the ones measured in the experiments. This discrepancy is similar to the one observed for the leading edge vortex of the DW, discussed in section 3.1.3.1.

3.2.5.2 Aerodynamic forces

Since the flow past a RDW is always unsteady, as discussed in the previous sections, the values of the force coefficients vary in time. Therefore, the force coefficients are time averaged before comparing them with the experimental data obtained from a force balance. Figure 3.32 shows the comparison between the lift and drag coefficients estimated numerically with those measured experimentally [1]. The lift coefficient shows an excellent agreement at angles of attack $\alpha = 5°$ and $10°$, and some discrepancies at $\alpha = 15°$ (7.4% error) and $20°$ (4.5% error). The comparison with the experimental data of the drag coefficient shows a larger but almost constant error at all angles of attack, similarly to the error detected in the DW case. The fact that the error is almost constant and of about the same magnitude, as the error detected for the DW, reinforces the hypothesis formulated in the case of the DW, that the causes for the underprediction are the same for all angles of attack and for both DW and RDW. As discussed previously, probable causes are: 1) The DW surface in the experiment has finite roughness, while in the numerical simulations is perfectly flat. 2) The DW model assumes a sharp leading edge, which is exactly sharp in the simulations, but not in the experiment, since sharp edges cannot be manufactured. 3) The DW mounting in the wind tunnel could also affect the readings of the force balance. 4) Another source of error could be the use of the RANS turbulence model in the boundary layer region.

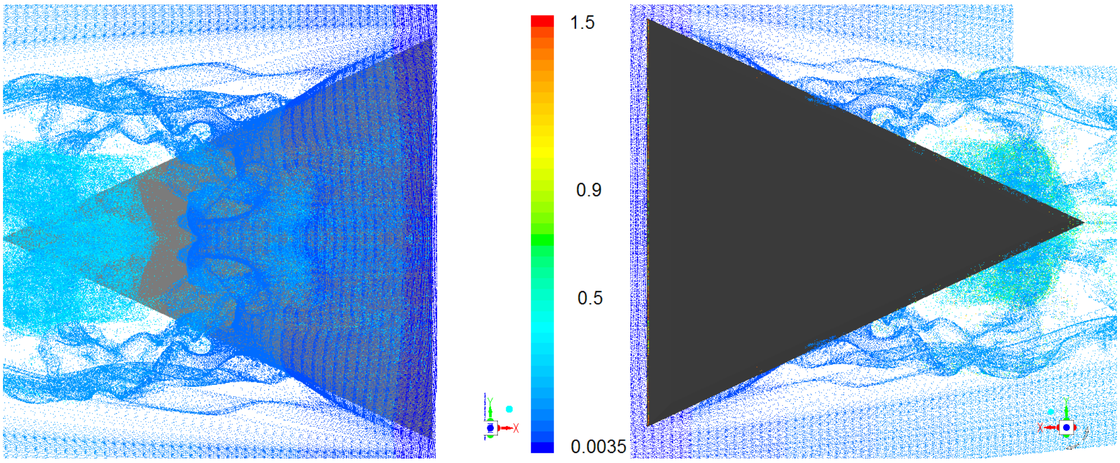

(a) TOp view of the particles injected from the upper injection line

(b) Bottom view of the particles injected from the upper injection line

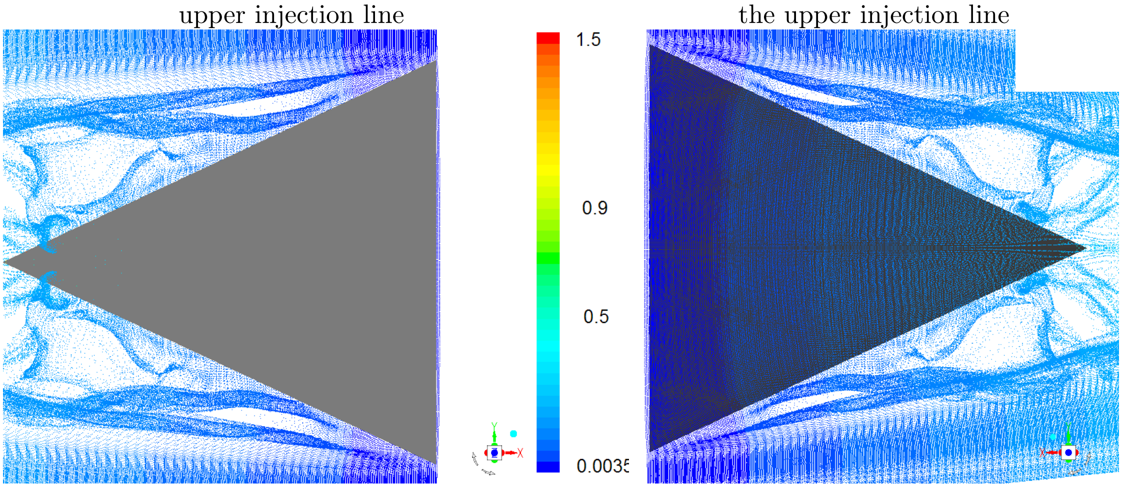

(c) Top view of the particles injected from the lower injection line

(d) Bottom view of the particles injected from the lower injection line

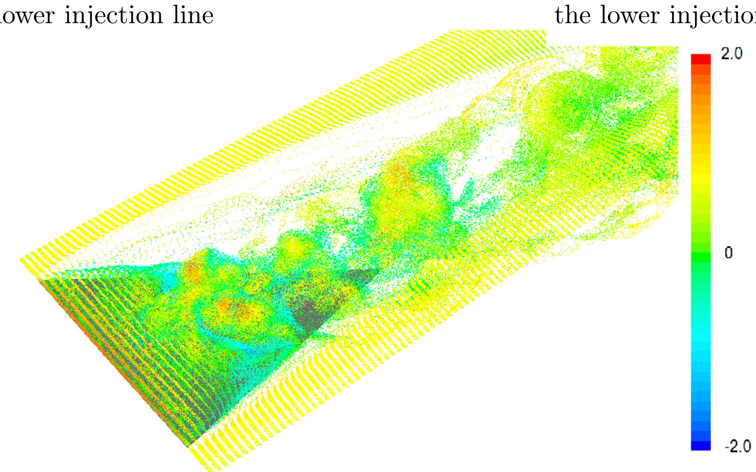

(e) Three-dimensional view of the particles colored in proportion to the z-component of velocity

Figure 3.30: Instantaneous snapshots of the massless particles injected at each time step into the flow past a RDW at angle of attack $\alpha = 14°$.

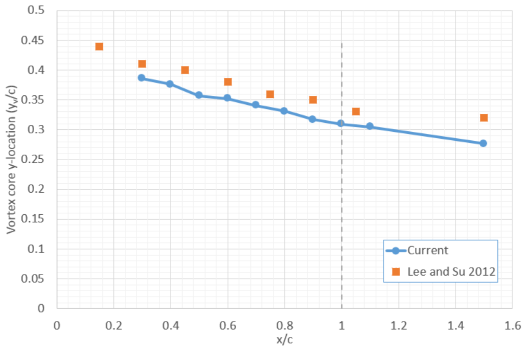

(a) Vortex core y-location

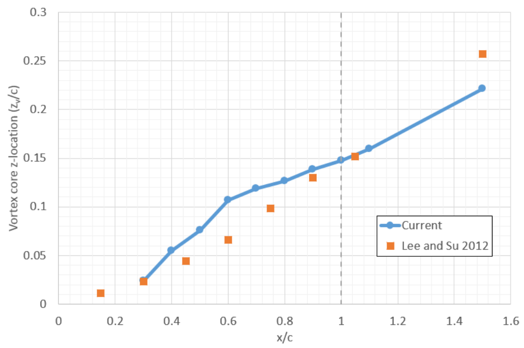

(b) Vortex core z-location

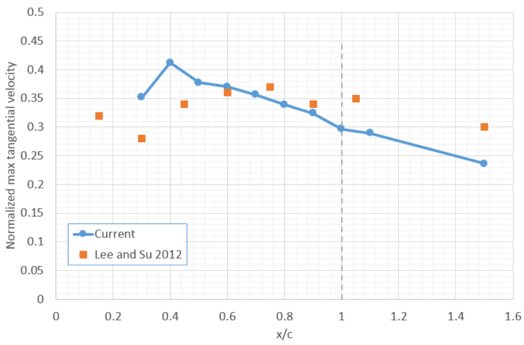

(c) Maximum tangential velocity

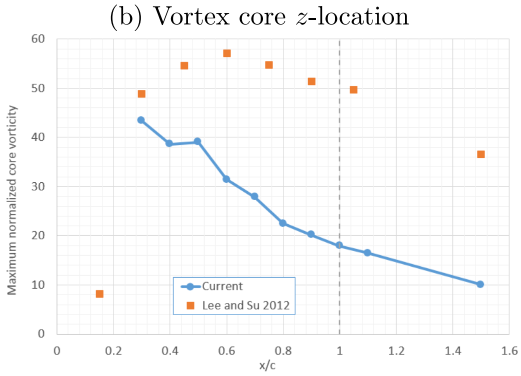

(d) Normalized maximum vorticity

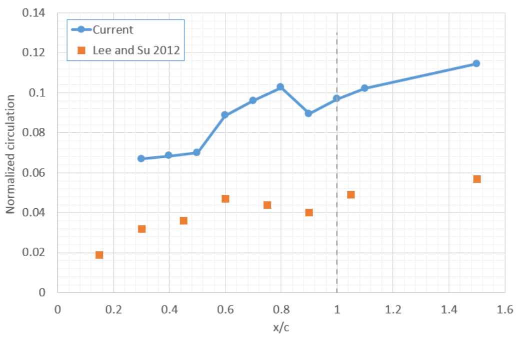

(e) Normalized circulation

Figure 3.31: Comparison with experimental data [2] of the characteristics of the tip vortex of a RDW at angle of attack $\alpha = 12°$ and $Re_\infty = 2.45 \times 10^5$.

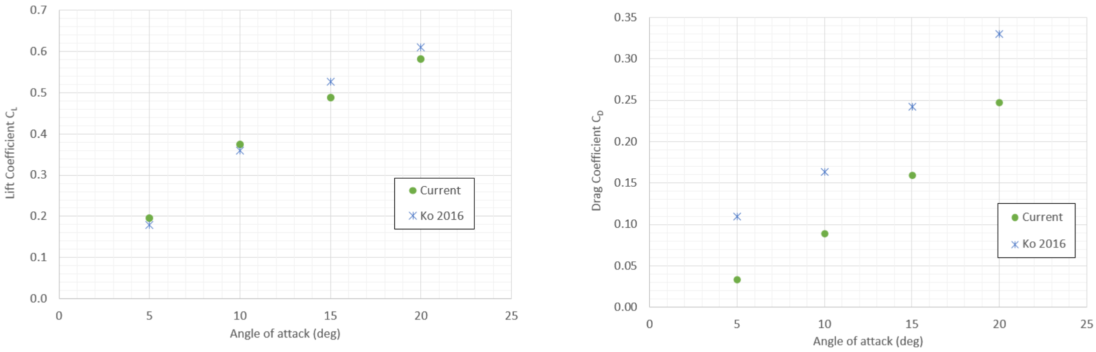

(a) Lift coefficient C_L (b) Drag coefficient C_D

Figure 3.32: Comparison against experimental data from [1] of the force coefficients of a RDW at different angles of attack α.

3.3 Performance of a DW versus a RDW

In this section we compare the numerical results of the simulations of the flows past the DW and the RDW and comment on their performance. We compare the aerodynamic forces and the vortex characteristics of the DW leading vortex and the RDW tip vortex. We also substantiate our comparisons leveraging the findings of some previous experimental studies.

3.3.1 Structure of the flowfield past a DW and a RDW

The structures of the flowfield past a DW and a RDW are substantially different although the two wings have exactly the same planform. In the case of a DW, the structure of the flowfield is characterized by two leading edge vortices. These vortices are formed by the separation of the flow from the windward side to the leeward side of the wing. The shear layer that forms rolls up in two vortices that sit on the leeward side of the wing and that are responsible for a large portion of the lift generated by a DW. These vortices are nearly stable for angles of attack less than 20°, above this angle of attack the leading edge vortices undergo a breakdown, the flowfiled become unsteady and the DW starts to stall.

In the case of a RDW the flowfield is totally different, characterized by spanwise vortices over the leeward side of the RDW and a pair of tip vortices that always lay outside the wing and move inboard as they evolve downstream, see figure 3.19(a). Contrary to the flowfield past a DW, the flowfield past a RDW is always unstable. The spanwise vortices are generated by the flow from the windward side of the wing that separates at its leading edge and are responsible for a large portion of the lift generated by the RDW. The spanwise vortices are continuosly convected downstrean. At the tips of the leading edge, on the windward side, two tip vortices are formed and fed by the shear layer generated by the separation of the spanwise flow on the windward side of the wing. Note that this separated flow does not roll up over the leeward side of the wing, as in the case of a DW, because of the receding angle of the planform. As shown in figure 3.22(a-e) the shear layer lay almost on the same plane as the RDW and rolls around the tip vortex feeding it. Note that the tip vortices do not contribute directily to the lift generated by the RDW. However, it appears that they contribute to lift indirectly. As they move inboard evolving downstream, they contain the spanwise vortices over the leeward side of the RDW and induce a narrow wake as shown in figure 3.18. Note that this analysis and interpretation of the flowfield past a RDW is complemented and supported by the experimental results of Ko [1], Lee and Su [2] and Lee and Ko [30].

3.3.2 Characteristics of the leading edge and tip vortices

As explained in the previous section the leading edge vortices of a DW and the tip vortices of a RDW have different mechanisms of formation, they play a diffrent role in the structure of the associated flowfields and their contribution to lift is also substantially different. For these reasons a comparison of the characteristics of these two vortices is not particularly meaningful but it is more of a curiosity. It also allow us to make further comparison with experimental results.

Figure 3.33 presents a comparison of the vortex characteristics for a DW and a RDW at angle of attack $\alpha = 10$ and Reynolds number $Re_\infty = 3.4 \times 10^5$. The vertical dashed line indicates the location of the trailing edge of either the DW or the RDW ends. Panels (a) and (b) present the projections of the trajectories of the vortices on the planes $z = 0$ and $y = 0$, respectively. The leading edge vortex of a DW is located above the wing and moves outwards as one moves downstream. On the other hand, the tip vortex of a RDW forms near the wing tip, and develops outside the wing, and moves inwards further downstream. The trajectories are, obviously, very different because the trajectory of the leading edge vortex starts at the apex of the DW while the trajectory of the tip vortex starts at the tip of the leading edge of the RDW. Interestingly, although the trajectories are very different over the wings, as they evolve downstream they connect at about half a chord downstream from the trailing edge of the wings.

Panels (d) and (e) show the maximum value of the normalized vorticity magnitude within the vortex core and the normalized circulation, respectively. The maximum values of the normalized vorticity of the leading edge vortex is about three times higher than the corresponding values for the tip vortex. Consistently, the normalized circulation of the leading edge vortex is more than twice larger than the circulation of the tip vortex. These differences between the leading edge vortices and the tip vortices seem to reflect their different role in the production of lift, the leading vortex is responsible for a large portion of the lift generated by a DW while the tip vortex does not contribute to the lift generated by a RDW.

Curiously, panel (c) show that the maximum values of the normalized tangential velocity is similar in both cases.

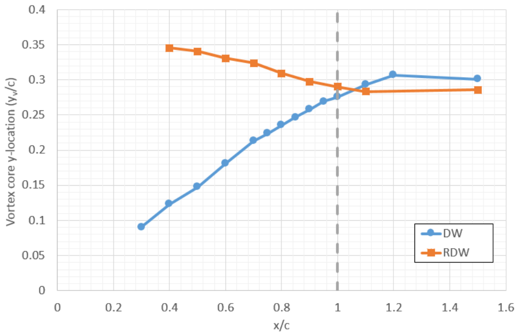

(a) Vortex core y-location

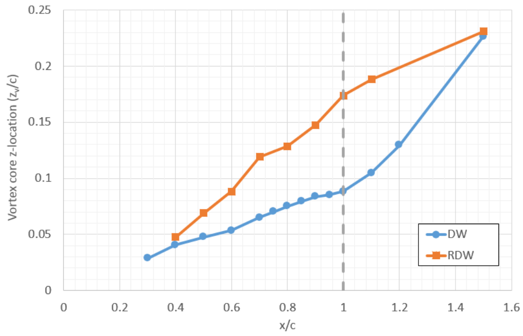

(b) Vortex core z-location

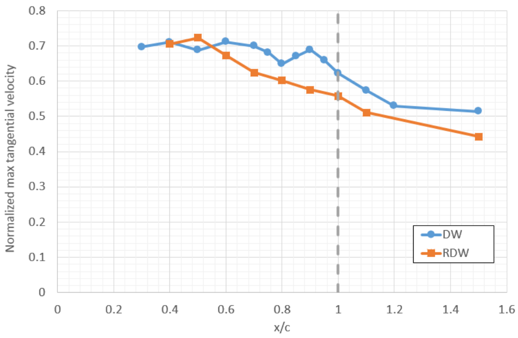

(c) Normalized maximum tangential velocity

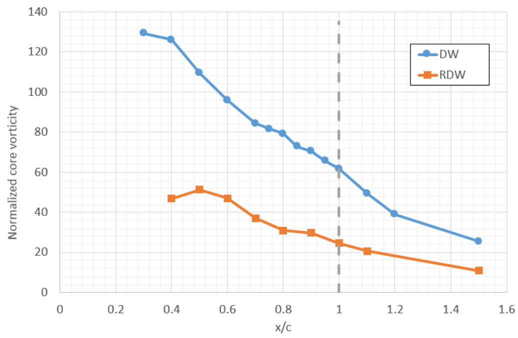

(d) Normalized maximum vorticity

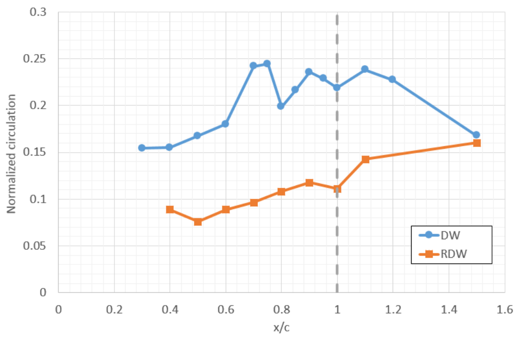

(e) Normalized circulation

Figure 3.33: Comparison of vortex characteristics of the DW leading edge vortex and the RDW tip vortex.

3.3.3 Aerodynamic forces

Figure 3.34 shows the comparison between the aerodynamic forces (panel (a) and (b)) and moment (panel (c)) coefficients of the DW and the RDW. At low angles of attack ($\alpha = 5°$ and $10°$), both wings generate nearly the same lift (panel (a)) and drag (panel (b)). At higher angles of attack ($\alpha = 15°$ and $20°$), the DW generates higher lift but also higher drag than the RDW. Interestingly, the lift-to-drag ratio of both wings is almost the same: at angle of attack $\alpha = 15°$, for the DW we have $C_L/C_D = 3.30$ while for the RDW is 3.06; at angle of attack $\alpha = 20°$, for the DW we have $C_L/C_D = 2.41$ while for the RDW is

2.37. Figure 3.34(c) compares the pitching moment coefficient $C_{m,c/4}$, which was evaluated at 25% of the wing middle chord, of a DW with a RDW. The RDW produces an almost constant ($0.05 \leq C_{m,c/4} \leq 0.08$) stabilizing moment coefficient, while the DW generates a destabilizing moment that decreases almost linearly with angle of attack from $C_{m,c/4} = -0.05$ at $\alpha = 5°$ to $C_{m,c/4} = -0.22$ at $\alpha = 20°$.

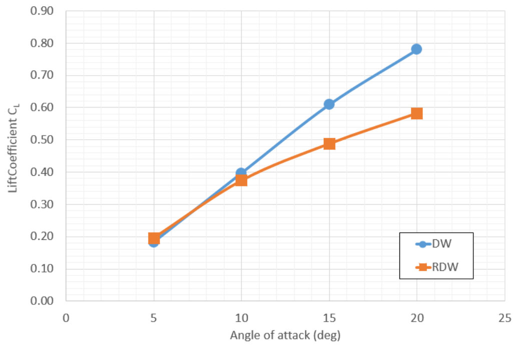

(a) Lift coefficient C_L against angle of attack α

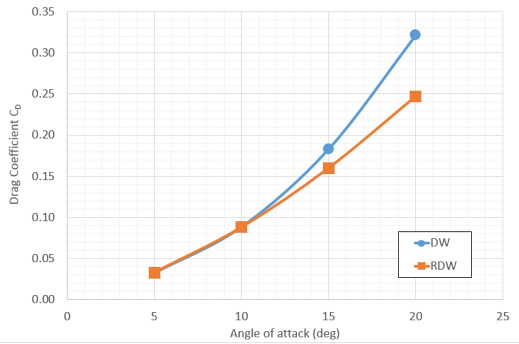

(b) Drag coefficient C_D against angle of attack α

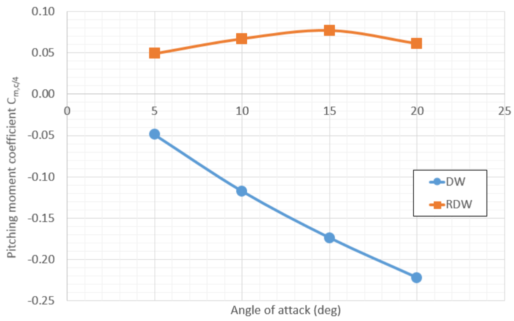

(c) Pitching moment coefficient C_m against angle of attack α

Figure 3.34: Comparison between the aerodynamic forces and moment coefficients for the DW and the RDW.

Chapter 4

Conclusions and Future Work

In this chapter we draw conclusions of the work presented in this thesis. We also make recommendations for potential future work that will extend the results presented in this thesis.

4.1 Conclusion

This thesis presented accurate numerical simulations of the flow past a DW and a RDW. Our work allows us to draw some important conclusions.

To design properly our numerical simulations performed using ANSYS Fluent, we followed the framework presented by Cummings *et al.* [28]. We performed a combined grid/time step sensitivity study to select the combination of grid and time step that produced the most accurate results in simulating the flow past a DW at angle of attack $\alpha = 20°$, when the leading edge vortices undergo to a breakdown. We tested the selected combination of grid and time step to simulate, among other angles of attack, the flow past a DW at angle of attack $\alpha = 20°$ when the leading edge vortices undergo a helical breakdown near the trailing edge of the DW. Our simulation predicted correctly the helical vortex breakdown contradicting the work of Robertson *et al.* [17] that stated that ANSYS Fluent was not able to predict the helical vortex breakdown of the leading edge vortices of a DW.

Our study showed that the flow past a RDW is always unsteady, contrary to the flow over a DW and, therefore, the flow past a RDW must be computed by performing an unsteady simulation. Our study also supported and complemented the experimental findings of Ko [1] and Lee and Su [2]. We showed that the flow past a RDW has nothing in common with the flow past a DW. While, in the case of a DW at angle of attack below 20°, the leading edge vortices produce quasi stationary lift and drag coefficents. In the case of a RDW, the tip vortices do not contribute to the lift and the spanwise vortices produced by the roll up of the shear layer separating from the leading edge produce unsteady lift and drag coefficients.

We were able to to find the relationship between the unsteadiness of the lift and drag coefficients of a RDW with the frequency of shedding of the vortices generated by the roll up of the shear layer separating from the leading edge of the RDW. The liason is the pressure field. The spanwise vortices shed from the leading edge of the RDW generate an unsteady low pressure (suction) pattern on the leeward side of the RDW. As the vortices move downstream so does the pressure pattern. Therefore, through a PSD analysis, we were able to show that the frequency of the oscillations of the pressure field reflect on the frequency of oscillation of the lift and drag coefficients.

Finally, we compared the performance of a DW with that of a RDW. We showed that low angles of attack, $\alpha \leq 10°$, the aerodynamic performance of the two wings is nearly identical. At angles of attack $\alpha > 10°$ the DW present a better lift performance at the cost of a worse drag performance. Interestingly, the lift-to-drag performance is the two wings at angles of attack $\alpha > 10°$ is almost identical. Furthermore we were able to show that the pitching moment coefficient $C_{m,c/4}$ of a RDW is much better behaved than that of a DW. The RDW produces an almost constant stabilizing moment coefficient, while the DW generates a destabilizing moment that decreases almost linearly with angle of attack. These findings support, complement and extend those of Ko [1] and Altaf *et al.* [29].

4.2 Future work

The results presented in this thesis open the door to some potentially interesting future work. First, we propose to extend our work to simulate accurately the flow past a DW and RDW at angles of attack up to 40°. In this case the flow past both planforms is unsteady. The DW is known to be stalled at angle of attack near 40°. On the other hand, the performance of the RDW is unknown at such high angles of attack, but it is expected to perform better than the DW.

Another interesting extension of the present work is to perform simulations without imposing symmetry with respect to the $y = 0$ plane. In this case, it is possible to simulate the flow past a RDW that is banking and study the interaction of the tip vortex with the spanwise vortices that populate the leeward side of the RDW. The goal of this study is to predict the potential maneuverability of a RDW.

Finally, following the lead of Lee [31], it would be useful to explore how to design the shape of the leading edge of a RDW in order to enhance its performance. In other words, we propose to formulate an optimization problem to optimize the shape of the leading edge of a RDW in order to reduce the unsteadiness of its lift and drag coefficients, improve its lift-to-drag performance and enhance its maneuverability.

References

[1] Lok Sun Ko. *An experimental investigation of the aerodynamics and vortex flowfield of a reverse delta wing.* Phd thesis, McGill University, 2016.

[2] T. Lee and Y. Y. Su. Aerodynamic performance of a wing with a deflected tip-mounted reverse half-delta wing. *Experiments in Fluids*, 53(5):1221–1232, 2012.

[3] Alexander M Lippisch. Ground effects utilizing and transition aircraft, jan 1965.

[4] Alexander M. Lippisch. Wing arrangement, dec 1969.

[5] S R Urquhart, S A Prince, and V Khodagolian. Aerodynamic study of reversed-delta wing surface craft in ground effect. *Collection of Technical Papers - 44th AIAA Aerospace Sciences Meeting*, 5(January):3067–3081, 2006.

[6] Heinz A. Gerhardt. Supersonic Natural Laminar Flow Wing, 1996.

[7] Ahmad Z. Al-Garni, Farooq Saeed and Abdullah M. Al-Garni. Experimental and Numerical Investigation of 65 Degree Delta and 65/40 Degree Double-Delta Wings. *Journal of Aircraft*, 45(1), 2008.

[8] Mario Lee and Chih-Ming Ho. Lift Force of Delta Wings. *Applied Mechanics Reviews*, 43(9):209–221, 1990.

[9] E. L. Houghton and P. W. Carpenter. *Aerodynamics for engineering students.* Butterworth-Heinemann, 2003.

[10] T. Lee and J. Pereira. Modification of static-wing tip vortex via a slender half-delta wing. *Journal of Fluids and Structures*, 43:1–14, 2013.

[11] N C Lambourne and D W Bryer. The Bursting of Leading'Edge Vortices - Some Observations and Discussion of the Phenomenon (Report No. 3282). Technical report, Ministry of Aviation - Aeronautical Research Council, London, 1961.

[12] H Werle. Sur l'eclatement des tourbillons. Technical report, ONERA, Chatillon, 1971.

[13] G. D. Miller and C. H K Williamson. Free Flight of a Delta Wing. *Physics of Fluids*, 1995.

[14] L A Schiavetta, K J Badcock, and R M Cummings. Comparison of DES and URANS for Unsteady Vortical Flows over Delta Wings. *45th AIAA Aerospace Sciences Meeting and Exhibit*, (January), 2007.

[15] Lucy M Schiavetta. *Evaluation of URANS and DES Predictions of Vortical Flows over Slender Delta Wings*. Phd thesis, University of Glasgow, 2007.

[16] Heinrich Ludeke and Stefan Leicher. Unsteady CFD analysis of a delta wing fighter configuration by Delayed Detached Eddy Simulation. *Notes on Numerical Fluid Mechanics and Multidisciplinary Design*, 97:202–211, 2008.

[17] Eric D Robertson and D Keith Walters. On the Vortex Breakdown Phenomenon in High Angle of Attack. In *ASME 2014 International Mechanical Engineering Congress and Exposition IMECE2014*, pages 1–9, 2014.

[18] M. Menke, H. Yang, and I. Gursul. Experiments on the unsteady nature of vortex breakdown over delta wings. *Experiments in Fluids*, 1999.

[19] D Rockwell. Three-Dimensional Flow Structure on Delta Wings at High Angle-of-Attack : Experimental Concepts and Issues. In *31 st Aerospace Sciences Meeting 81 Exhibitition*, 1993.

[20] S. Leibovich. The structure of vortex breakdown. *Annual Review of Fluid Mechanics*, 10(20):221–246, 1978.

[21] Jean M Delery. Aspects of vortex breakdown. *Progress in Aerospace Sciences*, 30(1):1–59, 1994.

[22] Michael Jones, Atsushi Hashimoto, and Yoshiaki Nakamura. Criteria for Vortex Breakdown Above High-Sweep Delta Wings. *AIAA Journal*, 47(10):2306–2320, 2009.

[23] B. A. Robinson, R. M. Barnett, and S. Agrawal. Simple numerical criterion for vortex breakdown. *AIAA Journal*, 32(1):116–122, jan 1994.

[24] T. B. Benjamin. Significance of the Vortex Breakdown Phenomenon. *Journal of Basic Engineering*, 87(2):518, 1965.

[25] N. Srigrarom, S.; Lewpiriyawong. Controlled Vortex Breakdown on Modified Delta Wings. *Journal of VIsualization*, 10(3):299–307, 2007.

[26] M R Visbal and I Reno. Computational and Physical Aspects- of Vortex Breakdown on Delta Wings. In *33rd Aerospace Sciences Meeting & Exhibition*, Reno, New Virginia, 1995.

[27] Ismet Gursul. Review of unsteady vortex flows over slender delta wings. *Journal of Aircraft*, 42(2):299–319, 2003.

[28] Russell M. Cummings, Scott A. Morton, and David R. McDaniel. Experiences in accurately predicting time-dependent flows. *Progress in Aerospace Sciences*, 44(4):241–257, 2008.

[29] Afaq Altaf, Ashraf a. Omar, Waqar Asrar, and Hani Bin Ludin Jamaluddin. Study of the Reverse Delta Wing. *Journal of Aircraft*, 48(1):277–286, 2011.

[30] T. Lee and L. Ko. Experimental study of the vortex flow and aerodynamic characteristics of a reverse delta wing. *Proceedings of the Institution of Mechanical Engineers, Part G: Journal of Aerospace Engineering*, 230(6):1126–1138, 2016.

[31] T. Lee. Impact of Gurney flaplike strips on the aerodynamic and vortex flow characteristic of a eeverse delta wing. *Journal of Fluids Engineering, Transactions of the ASME*, 138(6):061104–1–061104–9, 2016.

[32] A Altaf, T B Thong, A A Omar, and W Asrar. Influence of a reverse delta-type add-on device on wake vortex alleviation. *AIAA Journal*, 54(2):625–636, 2016.

[33] Afaq Altaf and Ashraf Ali Omar. Impact of a Reverse Delta Type Add-on Device on the Flap-tip Vortex of a Wing. *International Journal of Aviation, Aeronautics, and Aerospace*, 3(3), 2016.

[34] T Lee, LS Ko, and V Tremblay-Dionne. Effect of anhedral on a reverse delta wing. *Proceedings of the Institution of Mechanical Engineers, Part G: Journal of Aerospace Engineering*, 0(0):1–9, 2017.

[35] Hani Bin Ludin Jamaluddin, Ashraf A. Omar, and Waqar Asrar. Numerical Investigation of the Flow Over Delta Wing and Reverse Delta Wing. *Engineering Applications of Computational Fluid Dynamics, Advanced Structure Materials*, 44:85–101, 2015.

[36] Stephen B. Pope. *Turbulent Flows.* Cambridge University Press, Cambridge, 2000.

[37] Florian R Menter. Two-Equation eddy-visocity turbulence models for engineering applications. *AIAA Journal*, 32(8):1598–1605, 1994.

[38] F R Menter, M Kuntz, and R Langtry. Ten Years of Industrial Experience with the SST Turbulence Model. *Turbulence Heat and Mass Transfer 4*, 4:625–632, 2003.

[39] Antti Hellsten. Some improvements in Menter's k-omega SST turbulence model. In *29th AIAA, Fluid Dynamics Conference*, Reston, Virigina, jun 1998. American Institute of Aeronautics and Astronautics.

[40] Pavel E. Smirnov and Florian R. Menter. Sensitization of the SST Turbulence Model to Rotation and Curvature by Applying the SpalartâĂŞShur Correction Term. *Journal of Turbomachinery*, 131(4):041010, 2009.

[41] P. R. Spalart, W. H. Jou, Mikhail Kh Strelets, and S. R. Allmaras. Comments on the feasibility of LES for wings and on a hybrid RANS/LES approach. In *Advances in DNS/LES*, volume 1, 1997.

[42] Philippe R. Spalart. Detached-Eddy Simulation. *Annual Review of Fluid Mechanics*, 41(1):181–202, 2009.

[43] P. R. Spalart, S. Deck, M. L. Shur, K. D. Squires, M. Kh Strelets, and A. Travin. A new version of detached-eddy simulation, resistant to ambiguous grid densities. *Theoretical and Computational Fluid Dynamics*, 20(3):181–195, 2006.

[44] W Kyle Anderson and Daryl L Bonhaus. An Implicit Upwind Algorithm for Computing Turbulent Flows on Unstructured Grids. *Computers and Fluids*, 23(1):1–21, 1994.

[45] W Malalasekera and H K Versteeg. *An introduction to computational fluid dynamics : the finite volume method.* Pearson Education Ltd, 2007.

[46] Timothy Barth and Dennis Jespersen. The design and application of upwind schemes on unstructured meshes. In *27th Aerospace Sciences Meeting*, Reston, Virigina, jan 1989. American Institute of Aeronautics and Astronautics.

[47] ANSYS® Fluent 12.0 Theory Guide, 2009.

[48] Turgut Sarpkaya. Effect of the Adverse Pressure Gradient on Vortex Breakdown. *AIAA Journal*, 12(5):602–607, may 1974.

[49] Hammad Rahmanl and Kamran Ahmadl. Experimental and Computational Investigation of Delta Wing Aerodynamics. In *10th International Bhurban Conference on Applied Sciences & Technology (IBCAST)*, pages 203–208, 2013.

[50] Stefan Görtz. *Realistic simulations of delta wing aerodynamics using novel CFD methods.* Phd thesis, KTH Royal Institute of Technology, 2005.

[51] Martino Reclari, Shinji Fukao, Masamichi Lino, Takeshi Sano, and Yuuki Nakamura. CFD of Vortical Flows: Requirements and Mesh Adaption Techniques. In *Proceedings of the ASME-JSME-KSME 2015 Joint Fluids Engineering Conference*, pages 1–6. ASME, jul 2015.